



**Politecnico  
di Torino**

**Master of Science in Energy and Nuclear Engineering**

**Academic year 2021/2022**

**Modeling, experimental calibration and  
validation of a lithium-sulfur battery**

**Advisors**

Amici Julia Ginette Nicole

Versaci Daniele

Santarelli Massimo

Ferrero Domenico

**Candidate**

Marco Desiderio Loffredo Senesi

# **Acknowledgments**

*I would like to thank my family and friends for supporting me throughout the hard times with their care and enthusiastically celebrating my achievements, love you all.*

*I am grateful to all my advisors for the dedication they offered me throughout the development of my thesis work, encouraging me to understand and appreciate the topic and allowing me to “level up” on my academic training.*

# Table of contents

Table of contents .....	i
List of Figures .....	iv
List of Tables.....	vi
1. Introduction and batteries fundamentals .....	1
1.1 Introduction.....	1
1.2 Fundamental topics on batteries.....	3
1.2.1 Classification of electrochemical batteries .....	3
1.2.1.1 Open batteries.....	3
1.2.1.2 Closed Batteries.....	4
1.2.1.3 Semi-open batteries .....	5
1.2.2 Physicochemical phenomena occurring in batteries .....	6
1.2.2.1 The generation of the electrode potential.....	6
1.2.2.2 The electric double layer .....	9
1.2.2.3 The thermodynamics of an electrochemical cell.....	11
1.2.2.4 Polarization effects .....	14
1.2.2.5 The cell voltage .....	21
1.2.2.6 Key Performance Indicators.....	21
1.2.2.7 Cell energy balance .....	25
1.3 Lithium Sulfur Batteries structure and operation.....	26
1.3.1 Lithium-Ion Batteries.....	26
1.3.1.1 Lithium.....	26
1.3.1.2 LIBs structure and operation .....	27
1.3.2 Lithium Sulfur Batteries .....	30
1.3.2.1 Sulfur.....	30

1.3.2.2	LSB main reactions .....	31
1.3.2.3	A focus on the role of polysulphides.....	34
1.3.2.4	The LSB Cathode .....	38
1.3.2.5	The LSB Electrolyte.....	39
1.3.2.6	The LSB Anode.....	43
2.	Modelling .....	44
2.1	Modelling tool and interface .....	45
2.2	The Porous Electrode Theory (PET) applied to LSBs.....	46
2.2.1	Model Equations .....	47
2.2.1.1	Mass transfer equations .....	47
2.2.1.2	Thermodynamics equation .....	49
2.2.1.3	Electrochemical kinetics equations .....	49
2.2.1.4	Electroneutrality and charge conservation .....	50
2.2.1.5	Morphological and non-faradaic reactions kinetics relationships.....	51
2.2.2	Boundary Conditions .....	53
2.2.2.1	Anode/Separator interface.....	53
2.2.2.2	Separator/Cathode interface .....	54
2.2.2.3	Cathode/Current collector interface .....	55
2.3	Analysis of the models available in the literature .....	55
2.3.1	Comparison between K. and Z. adopted parameters .....	56
2.3.2	A focus on the Zhang model.....	60
2.3.2.1	Analysis on the dissolved species concentrations over the discharge.....	60
2.3.2.2	Sensitivity of the model to external conditions .....	63
3.	Experimental validation of the model .....	69
3.1	Battery assembly and testing .....	69
3.1.1	Coin cells assembling .....	69
3.1.1.1	Preparation of the cathodes .....	69

3.1.1.2	Preparation of the electrolyte .....	73
3.1.1.3	Final cell assembly .....	74
3.1.2	Battery Testing .....	75
3.1.2.1	Galvanostatic Cycling .....	75
3.1.2.2	Electrochemical Impedance Spectroscopy .....	78
3.1.2.3	Voltammetry .....	82
3.1.2.4	Galvanostatic Intermittent Titration Technique .....	86
3.2	Precalibration and validation of the model .....	90
3.2.1	Precalibration of the model and sensitivity analysis .....	90
3.2.1.1	Comparison between experimental and simulated discharge curves .....	91
3.2.1.2	Sensitivity analysis on diffusion coefficients .....	92
3.2.1.3	Sensitivity analysis on reference exchange current densities .....	93
3.2.2	Model calibration by experimental and literature data .....	95
3.2.2.1	Diffusion coefficients .....	95
3.2.2.2	Solubility product of octasulfur .....	96
3.2.3	Proposal of model calibration by structural modifications .....	97
3.2.3.1	Approaching calibration by introducing $Li_2S_2$ species .....	98
3.2.3.2	Focus on $Li_2S$ precipitation and porosity .....	102
3.2.4	Model Validation .....	110
4.	Conclusions .....	114
	Bibliography .....	115

# List of Figures

Figure 1. 1 – IEA net zero pathway targets for 2030 [2] .....	2
Figure 1. 2 – Electrode surface and electrolyte prior to interaction, during an oxidation process (a) ion motion due to the electrode potential generation (b) [3] .....	8
Figure 1. 3 – The electric double layer in different theories [4] .....	11
Figure 1. 4 – List of standard reduction potentials [5] .....	13
Figure 1. 5 – Effect of voltage hysteresis on a generic battery and lost work [7].....	25
Figure 1. 6 – Loss of electrical contact in the case of solid-state $S_8$ reduction [21] .....	32
Figure 1. 7 – PS driven sulfur redistribution over the conductive host [19] .....	36
Figure 1. 8 – Main characteristics of different electrolytes typologies [28] .....	43
Figure 2. 1 – From the physical problem to the computational solution [29].....	51
Figure 2. 2 – Graphical representation of tortuosity [31].....	47
Figure 2. 3 – Visual comparison between Kumaresan and Zhang model.....	55
Figure 2. 4 – Evolution of the dissolved species average concentrations over the discharge..	61
Figure 2. 5 – Evolution of the cathode porosity over the discharge.....	62
Figure 2. 6 – Extending Zhang model self-testing to lower c-rates .....	63
Figure 2. 7 – Species distribution at DOD = 100%, high C-rates [32] .....	64
Figure 2. 8 – Species distribution at DOD = 100%, low C-rates .....	65
Figure 2. 9 – Testing the model temperature sensitivity .....	66
Figure 3. 1 – KJB and octasulfur in powder containers (a), mortar, pestle and spatula to handle powders (b).....	70
Figure 3. 2 – Micropipette (a), PVdF in NMP solution (b), slurry in the test tube (c) .....	70
Figure 3. 3 – Ball milling machine.....	71
Figure 3. 4 – Tape casting (a) and slurry after drying in the oven (b) .....	71
Figure 3. 5 – Cutting tool (a) and weight-based sorting (b).....	72
Figure 3. 6 – Vacuum chamber (a), control system (b), vacuum pump (c) .....	72
Figure 3. 7 – Glovebox at DISAT Electrochemistry Lab [35].....	73
Figure 3. 8 – Coin cell components.....	74
Figure 3. 9 – Pre-closed cells .....	75
Figure 3. 10 – Arbin battery cycler .....	76
Figure 3. 11 – Discharge behaviour of a coin cell over C/10 formation cycles and subsequent C/5 cycling .....	76

Figure 3. 12 – Cycling behaviour in terms of capacity fade and coulombic efficiency fluctuations .....	77
Figure 3. 13 – C/10 and C/5 discharge curves employed for model validation.....	78
Figure 3. 14 – Nyquist plot from EIS performed on a generic battery [37].....	80
Figure 3. 15 – Nyquist plot of 3 lithium-sulfur coin cells.....	81
Figure 3. 16 – Cyclic Voltammetry for a reversible process [39].....	83
Figure 3. 17 – CV at different scan rates.....	84
Figure 3. 18 – GITT performed on a lithium sulfur coin cell, charge and discharge set at C/20 .....	87
Figure 3. 20 – Evaluation of $\Delta EPULSE$ vs $\sqrt{t}$ linearity in region B.....	88
Figure 3. 19 –Evaluation of $\Delta EPULSE$ vs $\sqrt{t}$ linearity in region A .....	88
Figure 3. 21 – Evaluation of $\Delta EPULSE$ vs $\sqrt{t}$ linearity in region C.....	89
Figure 3.22 – Comparison between experimental and simulated discharge curves.....	91
Figure 3. 23 – Parametric sweep on MD.....	92
Figure 3. 24 – Parametric sweep on MI1 and MI2.....	94
Figure 3. 25 – Comparison between calibrated, precalibrated curves and experimental data .	97
Figure 3. 26 – Effect of $Li_2S_2$ precipitation kinetics on Q2 [2] .....	98
Figure 3. 27 – Evaluation of Kum. proposed parameters for $Li_2S_2$ precipitation kinetics .....	99
Figure 3. 28 – Sweep on kinetic multipliers MK1 and MK2.....	100
Figure 3. 30 – Evaluation of the impact of cathode porosity on simulated discharge curves	103
Figure 3. 31 – Evaluation of the impact of MK1, $\sigma$ and $\epsilon_{Li_2S, pos, 0}$ on discharge curves .....	105
Figure 3. 32 – Specific capacity vs electronically conductive medium employed [44].....	106
Figure 3. 33 – Effect of porosity on exp. discharge curves in case of low (a) and high mass loading (b) [45].....	107
Figure 3. 34 – Evaluation of the impact of the multiplier MAV0 on discharge curves .....	109
Figure 3. 35 – Validation of the model .....	111
Figure 3. 36 – Validation of the model (modified $K_{sp, S_8}$ ) .....	112

# List of Tables

Table 2. 1 – Kumaresan and Zhang list of parameters .....	56
Table 2. 2 – Focus on OCV discrepancy .....	59
Table 3. 1 – PEIS paramaters and results .....	82
Table 3. 2 – Determination of $D_{Li^+}^{eff}$ from CV data fitting .....	85
Table 3. 3 – Diffusion coefficients from GITT .....	89
Table 3. 4 – Modification to model parameters in the precalibration stage .....	90
Table 3. 5 – Calibration on bulk diffusion coefficients .....	96
Table 3. 6 – Calibration on octasulfur dissolution properties .....	96
Table 3. 7 – Validation parameters .....	112

# 1. Introduction and batteries fundamentals

## 1.1 Introduction

The production of electrical and thermal energy is crucial for the support and development of anthropogenic activities as the manufacturing and transportation of goods and providing services both to industries and final consumers.

The availability of a plethora of dedicated established and emerging technologies raises the issue of determining their most appropriate mix.

This problem is not trivial at all, its solution is strongly conditioned by the goal to be pursued, ranging from the maximum productive capacity to an extreme environmental impact minimization.

As the first one would lead to a rapid condition of resource scarcity and a steep deterioration of the habitat for all living beings and the second one to a radical degrowth, reversing the improvements on human well-being to the pre-industrial era, the optimal solution stands in between.

The idea of sustainable development emerges, defined as:

*“(...) development that meets the needs of the present generation without compromising the ability of future generations to meet their own needs” [1].*

The availability of different technologies exploiting renewable resources allows a targeted fade out of fossil fuels-based systems depending on the peculiar properties of each country and regions.

The adoption of renewable energy systems is also related to energy security, as the opportunity to be independent from fossil fuels producing nations plays an important role in altering international political equilibria and bargaining power.

The International Energy Agency, an intergovernmental organisation providing policy recommendations, emphasizes the need to increase renewable installed capacity, promote the deployment of electric vehicles and plan actions to reduce the energy intensity of a country, thus increasing the energy efficiency to produce GDP (Figure 1.1) [2].

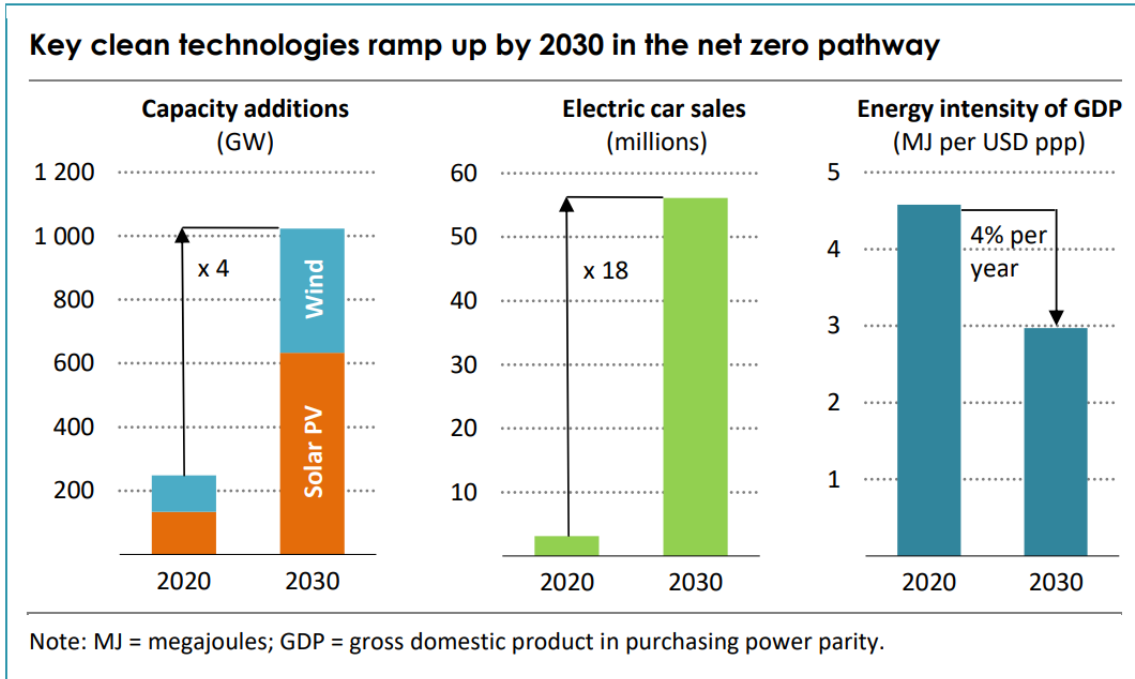


Figure 1. 1 – IEA net zero pathway targets for 2030 [2]

Solar and wind-based energy systems, being progressively involved in the energy mix of developed and economically emerging nations, present the intrinsic problem of daily, seasonal and yearly variability of their primary resource.

Merging this issue with the efforts to proceed toward the paths of electrification of transportation and heating, also considering the rise in the share of prosumers, Electrochemical Energy Storage (EES) systems plays an increasingly important role in the aim for sustainable development.

These devices allow to manage the mismatch in time and space between energy production and consumption by a bidirectional conversion of electrical energy into chemical energy.

Nowadays lithium-ion batteries (LIBs) represent the widest spread and most efficient technology among them, but scientific research always moves forward, proposing cheaper and better performing alternatives.

Lithium-sulfur batteries (LSBs) raise interest due to their lower costs and higher energy density/specific energy, while issues in understanding their underlying working mechanisms are still present.

The goal of this thesis is to study extensively LSBs with the purpose of investigating on the limitations and opportunities the state of art has to offer and compare computational modeling results to experimental data.

## **1.2 Fundamental topics on batteries**

### **1.2.1 Classification of electrochemical batteries**

A battery is an electrochemical device whose purpose is to store electrical energy into chemical energy by exploiting redox reactions, converting reactants into products to feed an electrical or electronic load by an external circuit.

Batteries are constituted by two electrodes, named positive electrode and negative electrode, where semi-reactions of oxidation (at anode) and reduction (at cathode) are properly separated by an interlayer, comprising an electrolyte and eventually a separator, to avoid direct contact between the reactants.

Closed batteries exchange only work and heat with the environment, while open batteries also exchange mass, intaking reactants and expelling the products of reactions.

Semi-open batteries mix the behaviour of the previously cited categories in peculiar ways depending on the specific device considered.

For the sake of simplicity, referring to closed batteries, during the discharge the term anode will be adopted to define the electrode where oxidation occurs and cathode for the electrode where reduction occurs.

#### **1.2.1.1 Open batteries**

These devices are open systems: chemical species involved in the reactions flow throughout the anode (fuel flow) and cathode (oxidizing agent flow).

Both electrodes are constituted by porous materials and don't react to form products (aside from parasitic processes) but allow the separation of reactants, the ionic transport between electrodes,

and perform a catalytic activity, fostering the conversion from chemical energy embedded in a fuel (as hydrogen or carbonaceous species) to electrical energy. The flow-rate of the reactants is adjusted depending on the power required by the user.

Fuel cells could operate at high temperatures (650-800 °C), as Solid Oxide Fuel Cells (SOFC), featuring high conversion efficiency, fuel flexibility and the opportunity to employ waste heat for cogeneration, suitable for stationary applications and reversible, or operate at low temperature (60-80°C), as Proton Exchange Membrane Fuel Cells (PEMFC), featuring better dynamic response and lower costs, suitable for automotive sector applications.

Intermediate operating temperature devices as Molten Carbonate Fuel Cells (MCFC) are interesting due to their potential adoption in decarbonization strategies.

The fuel could be extracted, produced by thermochemical processes (as biogas/syngas), by electrochemical process (as  $H_2/CO$ ) or by their appropriate combinations (as DME/syn- $CH_4$ ).

The reversibility of reactions is suitable at high temperature only, as for SOFC in reverse mode, acting as Solid Oxide Electrolyzer Cell (SOEC), while at low temperature an additional unit is required in the charging phase.

The employment of  $H_2$  as fuel for FC based energy storage is an open debate due to the lower round-trip efficiency compared to closed batteries.

#### 1.2.1.2 Closed Batteries

Being closed systems, only electrical work and heat is exchanged with the environment, while no mass transfer occurs across their boundaries.

During the discharge the materials participating in the reactions are stored as a part of the cell structure, power is provided to an external circuit due to a change in the internal morphology of the device, with the depletion of reactants and accumulation of products.

During the charging process, the reaction is reversed but only partially due to unavoidable irreversibilities leading to a progressive fade out in performances, thus a limited cyclability.

#### 1.2.1.2.1 *Primary Batteries*

These devices are single-use units as the recharge is not possible due to the irreversible change in morphology occurring during the discharge process and complex parasitic reactions. As an example, non-rechargeable alkaline batteries are constituted by a zinc powder anode, a manganese dioxide cathode and a potassium hydroxide paste electrolyte and account for the largest market share in this category.

#### 1.2.1.2.2 *Secondary batteries*

Systems capable of multiple discharge and recharge cycles due to the partial reversibility of their characterizing reactions, also called rechargeable batteries or accumulators.

The most adopted secondary batteries are cheap lead acid batteries while the commercial scale best performing ones are lithium-ion batteries.

#### 1.2.1.3 Semi-open batteries

##### 1.2.1.3.1 *Redox flow batteries*

These systems are constituted by a core fuel cell adopted as an energy converter and vessels to store reactants and products, allowing a decoupling between power and energy as the first is tuned by varying the converter size and the second by adjusting the tanks size. For example, vanadium redox flow batteries exploit four oxidation states of vanadium to operate.

##### 1.2.1.3.2 *Lithium-air batteries*

These devices are characterized by a closed anode in metallic lithium and an open porous cathode where air flows across the boundaries allowing the oxygen to oxidize lithium, thus producing electrical energy.

## 1.2.2 Physicochemical phenomena occurring in batteries

During the discharge the motion of electrons in the external circuit connected to the battery occurs from the lowest potential (anode) to the highest potential (cathode).

If a fixed amount of charge is generated, the potential at the electrodes would equalize due to the electrons migration, thus a continuous charge generation in time is required to maintain a suitable voltage between the electrode over the discharge phase.

### 1.2.2.1 The generation of the electrode potential

The Gibbs free energy (G) of a system is defined as the maximum amount of work extractable from it at constant temperature and pressure:

$$G = H - TS \quad (1.1)$$

Where H is the enthalpy, T the absolute temperature and S the entropy.

Considering a chemical reaction:

$$\Delta G_R = \Delta H_R - T\Delta S_R \quad (1.2)$$

The reacting system would be at equilibrium as its Gibbs free energy is minimized.

An important parameter to be accounted for is the chemical potential, being the change in Gibbs free energy per unit mole of the i-th substance added to the system, given the conditions expressed below:

$$\mu_i = \left( \frac{\partial G}{\partial n_i} \right)_{p,T,n_j \neq i} \quad (1.3)$$

Considering a generic reaction, the molar Gibbs free energy in standard conditions is:

$$\Delta G_R^0 = \sum_{i=1}^n \nu_i \mu_i(T_0, p_0) \quad (1.4)$$

Where stoichiometric coefficients are positive for products and negative for reactants.

The electrochemical potential adds to the chemical potential an electrostatics contribution, accounting for the effect of an electric field on a particle's energy. Adopting a continuum model, its distribution in a region of space could be described by:

$$\bar{\mu}_e(\mathbf{r}) = E_f(\mathbf{r}) - e_0\phi(\mathbf{r}) \quad (1.5)$$

$$\bar{\mu}_i(\mathbf{r}) = \bar{\mu}_i^\theta + k_B T \ln\left(\frac{c_i(\mathbf{r})}{c^\theta}\right) + \bar{\mu}_i^{ex}(\mathbf{r}) + z_i e_0 \phi(\mathbf{r}) \quad (1.6)$$

Being the first expression related to electrons and the second to the i-th charged species particles (e.g. ions), where  $E_f$  is the thermodynamic Fermi level of the electrode,  $\bar{\mu}_i^{ex}$  represents the excess chemical potential due to Excluded Volume Interactions (EVI),  $e_0$  the elementary charge,  $k_B$  the Boltzmann constant,  $\bar{\mu}_i^\theta$  the reference standard state electrochemical potential at a concentration  $c^\theta = 1M$ ,  $z_i$  the charge number while  $\phi$  is the electrostatic potential [3].

When a solid material is formed, the orbital energy levels of atoms or molecules merges and broaden, resulting in energy bands. The Fermi level is a hypothetical energy level within the band structure which has 50% probability of occupancy by a valence electron at any given time, it lies between the valence band (characterizing bonding electrons) and the conduction band (characterizing free moving electrons). Fermi levels of dissimilar materials will differ.

The work function is the amount of energy required to excite an electron from the Fermi level to the vacuum, where the electric field is zero, at the vacuum potential.

For a semiconductor or insulator, to allow an electron to move from its belonging atom to the surrounding ones, the energy to be provided must cover at least the band gap, being the energy difference between the valence band and the conduction band.

For a molecular material, the band gap is the difference in energy between the highest occupied molecular orbital (HOMO) and the one in the lowest unoccupied molecular orbital (LUMO).

For a conductor, the valence and the conduction band partially overlap.

The Fermi level depends on the specific structure of the material considered. Putting in contact two conductors, their Fermi level difference is the driver for electron flows between the materials. The charge separation leads to the development of an electric potential difference across the boundary, the Galvani potential  $\Delta\phi^G$  opposing to further electron flowing [3].

At equilibrium:

$$\bar{\mu}_{e^{-2}} = \bar{\mu}_{e^{-1}} \rightarrow E_f^2 + e_0 \Delta\phi^G = E_f^1 \quad (1.7)$$

The electrostatic potential energy difference equals the Fermi level offset between the two conductors. An analogous phenomenon occurs as a solid metallic body, named electrode, is exposed to an electrolyte.

Reduction and oxidation processes occur, involving the present ionic species and converting them to the neutral species or viceversa.

Reduction results in the removal of electrons from the electrode, leaving it positively charged, while the oxidation process provides electrons to the electrode, leaving it negatively charged (Figure 1.2).

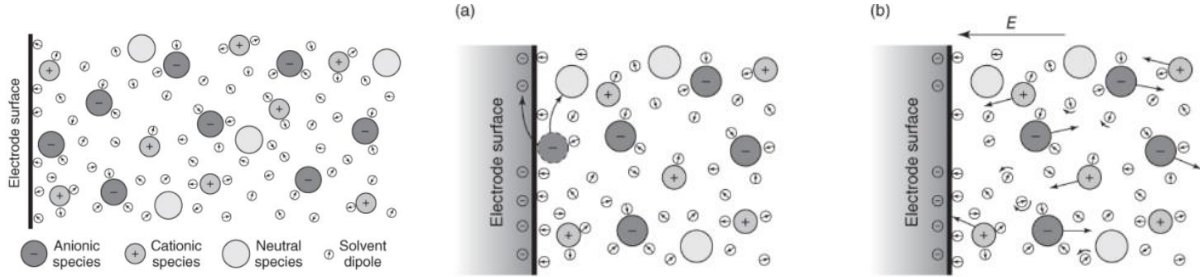


Figure 1.2 – Electrode surface and electrolyte prior to interaction, during an oxidation process (a) ion motion due to the electrode potential generation (b) [3]

The driving force in the reaction is the Gibbs free energy minimization, where:

$$\Delta G_R = \bar{\mu}_{Re} - \bar{\mu}_{ox} - \bar{\mu}_{e^{-}} \quad (1.7)$$

The charge separation generates an electric potential difference at the interface, as  $\Delta G_R > 0$  the reaction is biased toward spontaneous oxidation, as  $\Delta G_R < 0$  it is reduction biased.

Considering an oxidation process only, where anions are oxidized to neutral species, their depletion, as they adsorb on electrode surface, leads to a diffusion current, driving more anions towards the reaction site. The growing negative charge deposited generates an electric field repelling the anions, the effect of migration, which acts to reduce  $\Delta G_R$ .

Ionic interactions different from the electrochemical reaction are accounted in the term  $\bar{\mu}_i^{ex}$ , neglecting this term, the electrode/half-cell potential is thus the difference in potential between the electrode and the bulk solution as equilibrium is reached.

### 1.2.2.2 The electric double layer

The surface of the electrode has acquired charge due to the interaction with the electrolyte, the same phenomenon could also occur even if an electric potential is imposed from an external source.

Exposing a charged electrode towards an electrolyte solution, the electric double layer develops, which is a structure characterized by a charge layer in the solid material and a charge layer forming in the solution.

#### 1.2.2.2.1 *The Helmholtz Theory*

According to Helmholtz, ions characterized by the opposite charge (counterions) are adsorbed on the charged surface while co-ions are repelled.

The surface charge is thus neutralized by ions immobilization and the potential linearly decays to zero at a molecular distance.

#### 1.2.2.2.2 *The Gouy-Chapmann Theory*

GC theory is more complex as it includes the effects of thermal fluctuations, considering a diffused ion layer.

Combining the Poisson Equation for the electric potential, relating the charge density to the concentration of ions and employing the Boltzmann distribution, the Poisson-Boltzmann distribution is expressed as:

$$\nabla^2\psi = -\frac{F}{\epsilon_r\epsilon_0} \sum_i z_i c_i^0 \exp\left(-\frac{z_i F\psi}{RT}\right) \quad (1.8)$$

Being  $\psi$  the electric potential and  $c_i^0$  the concentration of the i-th chemical species.

In this mathematical model, a monodimensional problem is considered, with the electrode/electrolyte interface located at  $x = 0$ .

To compute the analytical solution, the exponential terms are expressed in their Taylor expansions and truncated to linearize the problem, assuming  $z\psi \ll RT/F$ .

The ionic strength  $I$  is defined as the concentration of charge in the solution and the Debye length  $\lambda_D$  as the distance between two plates of an equivalent capacitor providing the same capacitance as the EDL:

$$I = \frac{1}{2} \sum_i c_i z_i^2 \rightarrow \lambda_D = \sqrt{\frac{\epsilon_r \epsilon_0 RT}{F^2 I}} \quad (1.9)$$

The final expression for the approximated 1-D ODE is therefore extremely simplified.

Applying the Neumann boundary condition for the potential at infinite distance from the plate and explicating the surface potential  $\phi_s$  as the second boundary condition, the solution leads to an exponential decay with the distance from the plate.

At Debye length most of the surface charge on the electrode is screened by counter-ions.

#### 1.2.2.2.3 *The Stern Theory*

It combines the first two theories, considering a Stern layer with adsorbed counterion with a thickness  $a$ , partially screening the electric potential, leading to a first steep linear drop, then a diffused Gouy-Chapman layer toward the bulk electrolyte [4].

$$\begin{cases} \psi(x) = \psi_s \left(1 - \frac{x}{a}\right) + \psi_a \left(\frac{x}{a}\right) & 0 < x \leq a \\ \psi(x) = \psi_a \exp\left(\frac{a-x}{\lambda_D}\right) & x > a \end{cases} \quad (1.10)$$

The exposed theories lead to three different EDL structures resulting from the interaction between charged surface and electrolyte, qualitatively depicted in Figure 1.3.

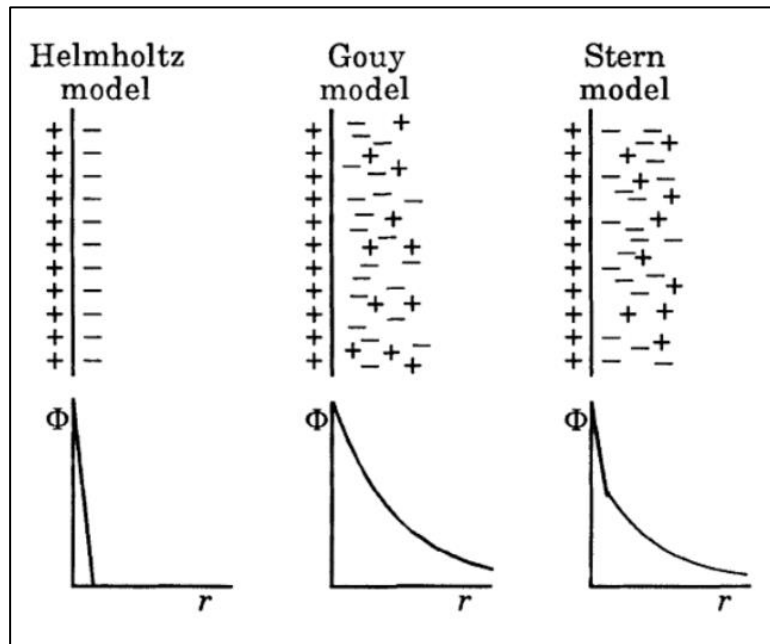


Figure 1. 3 – The electric double layer in different theories [4]

The currents produced by electrochemical reactions are called faradaic currents, while non-faradaic currents develop due to capacitive effect as a capacitor discharge or variation in electrode potential leading to ionic migration due to electric double layer capacitance, they are not related to chemical change in components but to electrostatic forces.

### 1.2.2.3 The thermodynamics of an electrochemical cell

#### 1.2.2.3.1 *Connecting two half-cells*

The structure of an electrochemical cell comprises two electrochemically active electrodes interfacing with a separator, permeated by an electrolyte.

The merge of the two structures, referred to as half-cells, forms a full cell.

The presence of a second electrode will alter the ionic arrangement in between, allowing a contact among the half-cells by closing an external circuit, generate an unbalance in the Gibbs free energy of the system thus, to minimize it, an external coherent flow of electrons will be transferred.

The electrode providing electrons is the anode, which is oxidation biased in the discharge reaction, while the electrode accepting electrons is the cathode, which is reduction biased.

The Faraday's law expresses a relationship between the amount of charge  $Q$  transferred from chemical species in an electrochemical reaction and the amount of moles  $n$  of the substance reacting. Differentiating the expression with respect to time, the relationship could be expressed between the current  $I$  and the mole flow rate  $\dot{n}$  :

$$Q = z_i F n \rightarrow I = z_i F \dot{n} \quad (1.11)$$

Where  $z_i$  is the amount of charge exchanged as a chemical species is reduced/oxidized.

The first and second principle of thermodynamics are expressed in the suitable form for stationary closed system at steady state in molar specific form, considering a generic reaction occurring in standard conditions:

$$\bar{q} - \bar{l} = \Delta H_R^0 \quad (1.12)$$

$$\bar{q} = T \Delta S_R^0 \quad (1.13)$$

Where  $\bar{q}$  and  $\bar{l}$  are the heat and work exchanged between the system and the environment per unit mole of the species with a unitary stoichiometric coefficient in the considered reaction.

Combining the previous expression with the definition of electrical work, the equilibrium cell potential (defined as  $E$  from now on) in standard conditions could be obtained:

$$-\bar{l} = \Delta G_R^0 = -E \cdot Q = -E \cdot F n \rightarrow E^0 = -\frac{\Delta G_R^0}{F n} \quad (1.14)$$

The equilibrium cell potential is related to the potentials of the electrodes by their difference:

$$E^0 = E_{cat}^0 - E_{an}^0 \quad (1.15)$$

While the equilibrium cell potential could be defined as the sum of the two double layer potential differences, the cathodic and the anodic one, each contribution is not easily measurable, thus an external reference for potential is required. Usually, the standard hydrogen electrode (SHE) is used as reference, consisting in hydrogen bubbling in an acidic solution, where the following reaction occurs on a platinum plate:



The standard redox potential ( $E_{red}^0$ ) expresses the tendency of a species to be reduced: it could be related to the half-cell potential in standard conditions for simple cells, where a single electrochemical reaction occur at each electrode.

$E_{red}$  is measured with reference to the SHE, a list of the most adopted redox pairs is shown below, in Figure 1.4.

Reaction	$E^0$ , V (SHE)	Reaction	$E^0$ , V (SHE)
$\text{Li}^+ + \text{e}^- \rightleftharpoons \text{Li}$	-3.045	$\text{HgO} + \text{H}_2\text{O} + 2\text{e}^- \rightleftharpoons \text{Hg} + 2\text{OH}^-$	0.098
$\text{K}^+ + \text{e}^- \rightleftharpoons \text{K}$	-2.935	$\text{Sn}^{4+} + 2\text{e}^- \rightleftharpoons \text{Sn}^{2+}$	0.154
$\text{Ca}^{2+} + 2\text{e}^- \rightleftharpoons \text{Ca}$	-2.866	$\text{Cu}^{2+} + \text{e}^- \rightleftharpoons \text{Cu}^+$	0.153
$\text{Na}^+ + \text{e}^- \rightleftharpoons \text{Na}$	-2.714	$\text{AgCl} + \text{e}^- \rightleftharpoons \text{Ag} + \text{Cl}^-$	0.2224
$\text{Mg}^{2+} + 2\text{e}^- \rightleftharpoons \text{Mg}$	-2.363	$\text{Hg}_2\text{Cl}_2 + 2\text{e}^- \rightleftharpoons 2\text{Hg} + 2\text{Cl}^-$	0.2676
$\text{Al}^{3+} + 3\text{e}^- \rightleftharpoons \text{Al}$	-1.662	$\text{Cu}^{2+} + 2\text{e}^- \rightleftharpoons \text{Cu}$	0.337
$\text{Ti}^{2+} + \text{e}^- \rightleftharpoons 2\text{e}^- \rightleftharpoons \text{Ti}$	-1.628	$\text{Fe}(\text{CN})_6^{3-} + \text{e}^- \rightleftharpoons \text{e}(\text{CN})_6^{4-}$	0.36
$\text{Zn}(\text{OH})_2 + 2\text{e}^- \rightleftharpoons \text{Zn} + 2\text{OH}^-$	-1.245	$\text{Cu}^+ + \text{e}^- \rightleftharpoons \text{Cu}$	0.521
$\text{Mn}^{2+} + 2\text{e}^- \rightleftharpoons \text{Mn}$	-1.180	$\text{I}_2 + 2\text{e}^- \rightleftharpoons 2\text{I}^-$	0.536
$2\text{H}_2\text{O} + 2\text{e}^- \rightleftharpoons \text{H}_2 + 2\text{OH}^-$	-0.822	$\text{O}_2 + 2\text{H}^+ + 2\text{e}^- \rightleftharpoons \text{H}_2\text{O}_2$	0.682
$\text{Zn}^{2+} + 2\text{e}^- \rightleftharpoons \text{Zn}$	-0.764	$\text{Fe}^{3+} + \text{e}^- \rightleftharpoons \text{Fe}^{2+}$	0.771
$\text{S} + 2\text{e}^- \rightleftharpoons \text{S}^{2-}$	-0.48	$\text{Br}_2 + 2\text{e}^- \rightleftharpoons 2\text{Br}^-$	1.065
$\text{Fe}^{2+} + 2\text{e}^- \rightleftharpoons \text{Fe}$	-0.441	$\text{O}_2 + 4\text{H}^+ + 4\text{e}^- \rightleftharpoons 2\text{H}_2\text{O}$	1.229
$\text{Cd}^{2+} + 2\text{e}^- \rightleftharpoons \text{Cd}$	-0.403	$\text{Cl}_2 + 2\text{e}^- \rightleftharpoons 2\text{Cl}^-$	1.358
$\text{Ni}^{2+} + 2\text{e}^- \rightleftharpoons \text{Ni}$	-0.250	$\text{PbO}_2 + 4\text{H}^+ + \text{e}^- \rightleftharpoons \text{Pb}^{2+} + 2\text{H}_2\text{O}$	1.455
$\text{Sn}^{2+} + 2\text{e}^- \rightleftharpoons \text{Sn}$	-0.136	$\text{Ce}^{4+} + \text{e}^- \rightleftharpoons \text{Ce}^{3+}$	1.61
$2\text{H}^+ + 2\text{e}^- \rightleftharpoons \text{H}_2$	0.0000	$\text{F}_2 + 2\text{e}^- \rightleftharpoons 2\text{F}^-$	1.87

Figure 1. 4 - List of standard reduction potentials [5]

### 1.2.2.3.2 The Nernst Law and the OCV

Exploiting the thermodynamic relationship among the Gibbs free energy and other state functions, the equilibrium cell potential could be calculated in conditions differing from the standard ones by the Nernst law:

$$E = E^0 + \frac{RT}{nF} \ln \left[ \frac{\prod_r a_r^{v_i}}{\prod_p a_p^{v_i}} \right] \quad (1.17)$$

Where the terms  $a$  accounts for the activity of the reactant/product, being a parameter extending the concept of concentration from an ideal solution to a real solution, by the definition:

$$a_i = \exp \left[ \frac{\mu_i - \mu_i^0}{RT} \right] = \gamma_i C_i \quad (1.18)$$

Where  $\gamma_i$  is the activity coefficient.

By performing the approximation of ideal solution (null enthalpy of mixing, Raoult's and Henry's laws valid)  $\gamma_i$  is unitary, the activities could be substituted by the concentrations at electrode/electrolyte interface:

$$E = E^0 + \frac{RT}{nF} \ln \left[ \frac{\prod_r C_r^{v_i}}{\prod_p C_p^{v_i}} \right] \quad (1.19)$$

Nernst law could also be adopted to calculate half-cell potential, this approach is required to perform calculations of theoretical battery performances when multiple semi-reactions occur.

The previously described cell potential is referred to as the open circuit voltage (OCV), corresponding to the voltage measured between the battery terminals as no current passes through the external circuit, thus in equilibrium conditions.

In a closed battery the OCV naturally decays due to the depletion of reactants and the formation of products, as the state of charge (SOC) reduces, due to the progressive minimization of the Gibbs free energy of the system.

The device must be capable to maintain a voltage between the electrodes, otherwise the electron transfer would stop, being self-limiting, which occurs as the whole system reaches the equilibrium state.

#### 1.2.2.4 Polarization effects

Polarization is a term referring to a set of phenomena generating an insulating layer between the bulk electrolyte and the active surface of the electrode, where electrochemical reactions take place. The activation polarization is related to the kinetics of chemical reactions, the concentration polarization to the lack of reactants in the active sites due to a diffusion effect.

By extension, it's also possible to include in polarization phenomena the voltage drop occurring between the electrode surface and the current collector, where the device to be powered or the measuring instrument is connected.

#### 1.2.2.4.1 The Butler-Volmer equation and the activation polarization

The study of the kinetics of reactions is crucial as real processes occur in a finite time, thus the equilibrium state could be not reached at the end of the process.

The concentration of reactants and products at the outlet of an industrial reactor or the time dependent phenomena affecting the performance of a battery, could not be determined by thermodynamics itself.

For a generic reaction with  $n$  reactants and products ( $A_i$ ), being  $\nu_i$  the stoichiometric coefficient with positive sign for products and negative sign for reactants:

$$0 \Leftrightarrow \sum_{i=1}^n \nu_i A_i \quad (1.20)$$

The rate of reaction is the speed of the evolution of the reaction, expressed as the rate of change of products or reactants, weighted by the inverse of their stoichiometric coefficient:

$$r = \frac{1}{\nu_i} \frac{dC_i}{dt} \left[ \frac{\text{mol}}{\text{m}^3 \text{s}} \right] \quad (1.20)$$

The factors affecting  $r$  are the following:

- 1) Temperature determines the kinetic energy of the particles, thus the energy of collisions, it increases both the probability and the energy of impacts.
- 2) Concentration of reactants increases the probability of collision between the molecules
- 3) The presence of a catalyst modifies the energy pathway of a reaction, it reduces the activation energy  $E_a$ , which is the minimum value of collision energy allowing the activation of the reaction.

In the following steps, the charge transfer kinetics expression is developed by considering as the driving force the potential difference between the solid phase and the region outside the EDL, in a semi-empirical relationship.

A well stirred solution, a fast transport of electroactive material and high electrolyte concentration lead to a fast decay of the electric potential, such that it could be approximated to drop to zero outside the Stern layer.

The law of mass action describes the rate of reactions by the following power law:

$$r = kC_1^n C_2^m \quad (1.21)$$

Where  $C_1, C_2$  are the concentration of reactants,  $m + n$  is the reaction order and  $K$  is the rate constant, expressed in Arrhenius form, being  $A$  a data-fitting pre-exponential parameter:

$$k = A \exp \left[ -\frac{E_a}{RT} \right] \quad (1.22)$$

For an electron-transfer process consisting in a single elementary step, where O is the oxidised species and R the reduced one:



The rates of anodic and cathodic reactions are expressed as first order dependent to the reactants concentration:

$$i_a = k_a C_R(0, t) \quad (1.24)$$

$$i_c = k_c C_O(0, t) \quad (1.25)$$

The net current density will be proportional to the difference between the anodic and cathodic rate:

$$i = F[k_a C_R(0, t) - k_c C_O(0, t)] \quad (1.26)$$

Where the rate constants are temperature dependent, by a pre-exponential factor  $Z$ :

$$k_a = Z \exp \left[ -\frac{E_{a,a}}{RT} \right] \quad (1.27)$$

$$k_c = Z \exp \left[ -\frac{E_{a,c}}{RT} \right] \quad (1.28)$$

Considering the conduction of equilibrium, the rates of cathodic and anodic reactions must balance, thus the net current must be zero and the concentration gradient must be null:

$$\ln \left[ \frac{C_O(0, t)}{C_R(0, t)} \right] = \frac{E_{a,c} - E_{a,a}}{RT} \quad (1.29)$$

While by the Nernst equation, considering the equilibrium concentration:

$$\ln \left[ \frac{C_O^*}{C_R^*} \right] = \frac{F(E_{eq} - E^0)}{RT} \quad (1.30)$$

By combining the previous equations, a potential difference compared to standard conditions will affect not only the equilibrium concentration but also the difference in activation energy values:

$$E_{a,c} - E_{a,a} = F(E_{eq} - E^0) \quad (1.31)$$

The Stern layer voltage, multiplied by the transfer coefficient, provides a contribution to the activation energy barriers, which is shared between reactants and products energy levels.

Adopting a phenomenological approach, a linear variation in activation energies is considered, allocating the effect of potential offset through the forward and backward transfer coefficients  $\alpha_a$  and  $\alpha_c$ :

$$E_{a,a} = E_{a,0} - \alpha_a F(E_{eq} - E^0) \quad (1.32)$$

$$E_{a,c} = E_{a,0} + \alpha_c F(E_{eq} - E^0) \quad (1.33)$$

$$\alpha_c + \alpha_a = 1; \quad (1.34)$$

$$k_0 = Z \exp \left[ -\frac{E_{a,0}}{RT} \right] \quad (1.35)$$

$$E_{a,c} - E_{a,a} = F(E_{eq} - E^0) \quad (1.36)$$

$$k_{a,0} = k_0 \exp \left[ \frac{\alpha_a F(E_{eq} - E^0)}{RT} \right] \quad (1.37)$$

$$k_{c,0} = k_0 \exp \left[ -\frac{\alpha_c F(E_{eq} - E^0)}{RT} \right] \quad (1.38)$$

Operating in non-equilibrium conditions (non-null current flowing), the half-cell potential differs from the equilibrium value by the activation overpotential:

$$\eta_{act} = E - E_{eq} = \phi_1 - \phi_2 - E_{eq} \quad (1.39)$$

Where  $\phi_1$  is the solid-phase potential and  $\phi_2$  is the electrolyte-phase potential.

The activation overpotential acts biasing the reaction toward the formation of products, thus:

$$k_0 = Z \exp \left[ -\frac{E_{a,0}}{RT} \right] \quad (1.40)$$

$$k_a = k_{a,0} \exp \left[ \frac{\alpha_a \eta_{act}}{RT} \right] \quad (1.41)$$

$$k_c = k_{fw,0} \exp \left[ -\frac{\alpha_c \eta_{act}}{RT} \right] \quad (1.42)$$

By experimental evidence, for the purpose of battery modelling, the transfer coefficients could be considered equal  $\alpha_{fw} = \alpha_{bw} = \alpha = 0.5$ , the expression of the total current density becomes:

$$i = F \left\{ k_{a,0} C_R(0, t) \exp \left[ \frac{0.5 \eta_{act}}{RT} \right] - k_{c,0} C_O(0, t) \exp \left[ -\frac{0.5 \eta_{act}}{RT} \right] \right\} \quad (1.43)$$

The electric field affects the energy level of reactants and products, as the cell is in open circuit conditions the contribution required is null while higher is the current withdrawn, higher is the overpotential contribution required.

The exchange current density  $i_0$  is defined as the rate of forward reaction and the opposite of the rate of backward reactions at equilibrium:

$$i_0 = F k_0 C_0^* \exp \left[ -\frac{0.5 F (E - E^0)}{RT} \right] = F k_0 C_R^* \exp \left[ \frac{0.5 F (E - E^0)}{RT} \right] \quad (1.44)$$

$$i = i_0 \left\{ \exp \left[ \frac{0.5 \eta_{act}}{RT} \right] - \exp \left[ -\frac{0.5 \eta_{act}}{RT} \right] \right\} \quad (1.45)$$

Considering the anodic process, in the discharge phase, the oxidation kinetics overcome the reduction one, thus a net flow of electrons is provided toward the external circuit, being the evaluated current density negative, meaning that current is withdrawn from the environment.

While for a cathodic process, in the discharge phase, the reduction kinetics overcome the oxidation one, thus a net flow of electrons is withdrawn from the external circuit, being the evaluated current density negative, thus current is provided to the environment [4].

Adopting the symmetric expression for the exchange current density, the activation overpotential can be derived for a generic reaction involving  $n$  electrons transferred as:

$$\eta_{act}(SOC, i) = \frac{RT}{0.5nF} \sinh^{-1} \left( \frac{i}{2i_0} \right) \quad (1.46)$$

The contribution required by the kinetics to produce a specific current will reduce the voltage output of the battery.

The presence of a catalyst, reducing the activation energy of the processes, higher temperature and a finely designed electrodes morphology act by reducing the activation overpotential [6].

#### 1.2.2.4.2 *The ohmic polarization*

Considering the Ohm's law, electronic resistance is a proportionality factor between the electric potential difference across a body and the electronic current flowing throughout it.

Resistivity is evaluated as resistance per unit length, its reciprocal is the conductivity:

$$\sigma_s = \frac{l_s}{R_s A} = \rho_s^{-1} \quad (1.47)$$

Where  $l$  is the length perpendicular to the cross section of the body of surface area  $A$  while  $R$  is its resistance.

The property of charge is also possessed by ions and the Ohm's law can be applied identically to the electrolyte, where ionic current flows throughout its length between electrodes, compensating for the electronic current of the external circuit.

The ionic conductivity for a specific charged species  $i$  could be defined as:

$$\sigma_i = F^2 \mu_i z_i^2 c_i = 2F^2 \mu_i I_i = \rho_i^{-1} \quad (1.48)$$

Where the terms  $\mu_i$  refers to the ionic mobility, being the speed of ions when the material is subjected to an electric field of 1 V/m.

Combining the contribution of electronic and ionic resistance the ohmic overpotential could be described as:

$$\eta_{ohm}(SOC, i) = (\rho_s l_s + \rho_i l_i) i \quad (1.49)$$

Where the electronic and ionic paths differ [6].

#### 1.2.2.4.3 Diffusion and concentration polarization

Diffusion is a mass transfer phenomenon, the driving force of a particle motion in a medium is related to its concentration gradient, its mass flux  $J$  [kg/m<sup>2</sup>s] is a vector quantity and could be expressed by the Fick's first law, where  $D$  [m<sup>2</sup>/s] is the diffusion coefficient, varying with temperature by the Arrhenius law:

$$J_i = -D_i \nabla c_i \quad (1.50)$$

$$D = D_0 \exp \left[ \frac{Q}{RT} \right] \quad (1.51)$$

As a battery is discharging at high current density, the reactants inertia could lead to their depletion at the active sites, generating a concentration polarization acting on the cell voltage:

$$\eta_{conc}(SOC, i) = \left| \frac{RT}{zF} \nu \ln \left( 1 - \frac{i}{i_{lim}} \right) \right| \quad (1.52)$$

Where the  $i_{lim}$  is the limiting current density, which is the value at which complete reactants depletion would occur.

Further details on diffusion and transport phenomena will be provided in a dedicated paragraph [6].

#### 1.2.2.5 The cell voltage

The cell voltage could be finally defined as:

$$V = E - (\eta_{act,anode} + \eta_{act,cathode} + \eta_{ohm} + \eta_{conc,anode} + \eta_{conc,cathode}) \quad (1.53)$$

Where the first term is related exclusively to thermodynamic effects and polarization terms are related to the system irreversibilities.

The specific behaviour of the simplified presented equation is partially the reason of the asymmetries between the charge and discharge curve of a battery, while upon progressive cycling other effects might take place depending on the specific chemistry [6].

#### 1.2.2.6 Key Performance Indicators

A complete characterization of the performance, status, cost and environmental impact of a cell, module or battery pack is required to perform comparison among the possible available options, both for lab scale and for commercial units and to select the most suitable for a specific application.

Key Performance Indicators efficiently describe characteristic behaviours and consider degrading phenomena occurring in the devices providing simple synthetic figures.

A list of the most relevant KPIs is provided below.

##### 1.2.2.6.1 *Capacity*

Capacity is the amount of available charge to be exchanged with the external circuit, being the discharge capacity the amount of charge that could be provided, while the charge capacity the amount of charge which could be stored.

Theoretical capacity  $Q_t$ , commercially expressed in Ah, could be calculated by Faraday's law on the active materials, the limiting value is the minimum capacity between anodic and cathodic one.

The theoretical specific capacity (Ah/g) could be calculated by:

$$q_t = \frac{Q_t}{m_{tot}} \quad (1.54)$$

Where the total mass of the battery  $m_{tot}$  must be considered.

#### 1.2.2.6.2 State of charge/discharge

Considering a discharged battery being charged with a current  $I(\tau)$ , where  $Q_0 = \int_{t_0}^{\infty} I(\tau) d\tau$  is the maximum charge that the device could hold in the process, by the charging time  $t_c$ , the State of Charge could be defined as:

$$SOC(\%) = \frac{\int_{t_0}^{t_c} I(\tau) d\tau}{Q_0} 100 \quad (1.55)$$

Thus, a SOC = 100% the battery will be completely charged, while a SOC = 0% states that the device is completely discharged.

The Depth of Discharge (SOD) is the complementary to 100 of the SOC, thus a fully charged battery has DOD of 0% while for a fully discharged DOD is 100%.

To avoid a fast degradation of the battery performance, it is required to avoid limit conditions of fully charged or fully discharged devices.

#### 1.2.2.6.3 State of Health

Different chemistries adopted would lead to different capacity fading mechanism, leading to a  $Q_{present} < Q_{initial}$ . Employing a common indicator among the different typologies, the State of Health (SOH) is defined as:

$$SOH(\%) = \frac{Q_{present}}{Q_{initial}} \quad (1.56)$$

Depending on the specific application, a different limiting SOH could be selected before reaching the time of disposal of the battery, called End of Life (EoL).

A virtuous and sustainable procedure is to guarantee a second life to the device, considering a battery adopted in electric vehicles, as SOH reaches 80% its performances aren't suitable anymore for the automotive sector but could be sufficient to operate in stationary applications as renewable energy systems storage.

#### 1.2.2.6.4 C-rate

C-rate is a measure of the rate at which a battery is charged/discharged relative to its specific capacity. If the applied current  $I_{app}$  is  $I_{1C}$  the battery is expected to charge/discharged in 1 hour, but charge/discharged time is practically always lower because of irreversibilities effects. Providing a rigorous definition:

$$C = \frac{I_{app}}{I_{1C}} \quad (1.57)$$

#### 1.2.2.6.5 Voltage

The voltage of the battery defines the specific energy per unit charge of electrons provided to the external circuit. Depending on the electrical/electronic load, it might be required to guarantee a specific input voltage range not to be over or undercome.

#### 1.2.2.6.6 Energy and derived parameters

The energy stored in a battery, commercially expressed in  $Wh$ , could be calculated based on the variation of the state of charge between the initial and final state of charge over the charging or discharging process:

$$E = \int_{SOC_i}^{SOC_f} V(SOC)Qd(SOC) \quad (1.58)$$

The normalization over the mass or the volume of the system allows to calculate the specific energy  $e_m$ , expressed in  $Wh/kg$  or  $Wh/g$ , and the energy density, expressed in  $Wh/m^3$ .

$$e_m = \frac{E}{m_{tot}} \quad (1.59)$$

$$e_v = \frac{E}{V_{tot}} \quad (1.60)$$

#### 1.2.2.6.7 Power and derived parameters

Electrical power is the energy per unit time exchanged between the battery and the external circuit, it could be expressed as the product between voltage and current:

$$P = \frac{dE}{dt} = VI \quad (1.61)$$

The normalization over the mass or the volume of the system allows to calculate the specific power, expressed in W/kg or W/g, and the energy density, expressed in W/m<sup>3</sup>.

$$p_m = \frac{P}{m_{tot}} \quad (1.62)$$

$$p_v = \frac{P}{V_{tot}} \quad (1.63)$$

#### 1.2.2.6.8 Efficiencies

Coulombic (or Faradaic) efficiency defines the charge storage efficiency of the device. A value below 100% implies that a part of the charge transferred during the charging process is not available during the discharge. This behaviour could be due to parasitic reaction occurring or form of leakages inside the battery.

Coulombic efficiency is not fully representing the losses in the system; indeed, another relevant parameter is the voltaic efficiency, defining the impact of polarization effects on voltage hysteresis. The product of the two of them provides the energy efficiency:

$$\eta_{coulombic} = \frac{Q_{dis}}{Q_{char}} \quad (1.64)$$

$$\eta_{voltaic} = \frac{\int_0^{t_{dis}} V_{dis}(\tau) d\tau}{\int_0^{t_{char}} V_{char}(\tau) d\tau} \quad (1.65)$$

$$\eta_{energy} = \eta_{coulombic} \eta_{voltaic} \quad (1.66)$$

### 1.2.2.6.9 Self-discharge rate

Batteries in idle state face a slow reduction in their SOC due to parasitic reactions and to not null electronic conductivity of the electrolyte, resulting in a limited but impacting internal short circuit current. Self-discharge rate could be calculated as:

$$SDR(\%) = \frac{1}{SOC} \frac{dSOC}{dt} \Big|_{idle} 100 \quad (1.67)$$

Self-discharge reduces the shelf life of batteries, which is the main reason leading to a lower SOC of the devices at their first use.

### 1.2.2.7 Cell energy balance

Considering the shape of a generic charge/discharge curve, the energy exchange involved is the result of the voltage integration over the charge transferred in the process (Figure 1.5). Therefore, it is possible to state that the lost electrical work over a cycle could be expressed as the difference between the charge and discharge voltage profiles, resulting in the generation of heat:

$$\Psi = E_{ch} - E_{dis} = \oint V(SOC) Q d(SOC) = Q_{irr} \quad (1.68)$$

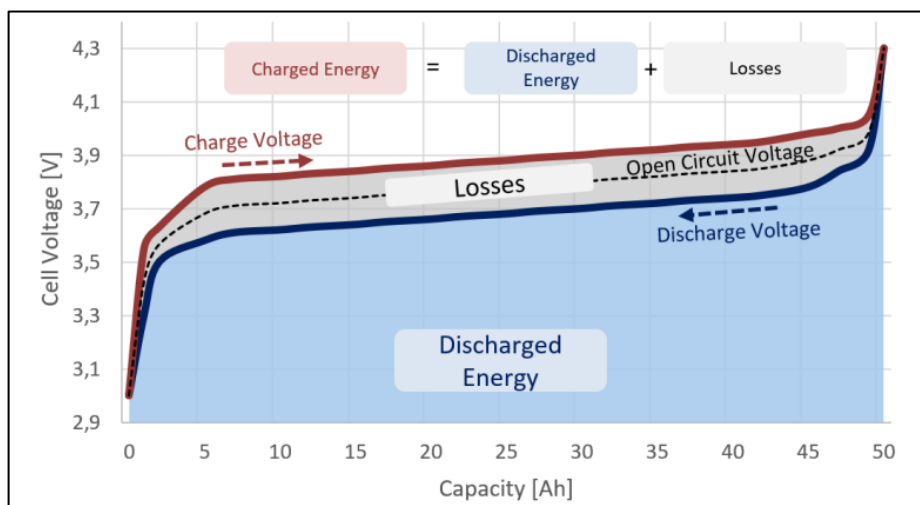


Figure 1. 5 - Effect of voltage hysteresis on a generic battery and lost work [7]

## 1.3 Lithium Sulfur Batteries structure and operation

Before providing a detailed description of the structure and main mechanisms underlying the operation of Lithium Sulfur Batteries (LSBs), it's useful to have a basic understanding of Lithium-Ion Batteries (LIBs) to perform a comparison between these systems.

### 1.3.1 Lithium-Ion Batteries

In the last decades lithium ion-batteries (LIBs) have been the most diffused technology to power most of portable electronics and electric vehicles (EVs/HEVs) due to their superior characteristics (mainly due to adoption of lithium at the anode) compared to the cheaper but lower quality lead-acid batteries or nickel-cadmium batteries [8].

#### 1.3.1.1 Lithium

Lithium is an alkali-metal, characterized by the lowest density between metals and solid elements in general. Metallic lithium is silverish in colour, soft and flammable. Being highly reactive, it is not found in elemental form on Earth.

At the dawn of its technological employment, lithium has been mostly extracted from hard rock, as lithium carbonates or silicates, up to the 80's, while in the 90's the dominant source became the brine from sea, surface deposits and groundwater [9]. As the price of lithium skyrocketed in the last decade due to its high demand, novel processes are investigated for a more efficient mineral extraction, including new spodumene-based ones, due to its high lithium content [10].

The extremely high specific capacity (3860 mAh/g) combined to the lowest potential vs SHE (-3.04 V) would crown the metallic lithium anode as the best choice among the anodes, operating by stripping (discharge) and plating (charge) reaction.

However, several major problems must be addressed, as significant volume change over cycling, high sensibility to air and moisture and an irregular dendritic growth during the charging phase.

The formation of dendrites over cycling would induce a shading effect hindering an uniform deposition of the material. These slender structures could break, lithium particles could diffuse towards the bulk electrolyte and, being unreachable by electrons and not being subjected to coulombic forces (not being charged), cause the permanent loss of active material.

Apart from the technical problem, socioeconomic issues of lithium employment should also be discussed.

Nowadays the majority of world lithium production derives from one brine systems in Argentina, one in Chile and two in China, while most of the mineral extraction occurs from four sites in Australia and one in China. Smaller operations are also present in in USA, Portugal, Bolivia and Zimbabwe [11].

The “Lithium Triangle” is a region between Chile, Argentina and Bolivia, where more than half of the world lithium reserves are present (around 50 million tons).

In these areas, land expropriation from the local population and careless exploitation approach, mostly by foreign companies, lead to socio-economic and environmental issues, increasing soil and water pollution and water shortage. The design and erection of more adequate infrastructures, the development of projects for the benefit of local communities and a less aggressive extraction activity would mitigate the negative impacts discussed [12].

### 1.3.1.2 LIBs structure and operation

#### 1.3.1.2.1 *Electrodes*

The earliest structure of LIBs comprises a  $LiMO_2$  powder adopted at the positive electrode, where the transition metal M is commonly cobalt (*LCO*), and graphite powder at the negative electrode, where lithium ions are intercalated (inserted) in the layered structure during the charge [13].

Over decades, huge effort has been dedicated to the improvement of cathode material.

$Li(Ni, Mn, Co)O_2$  (NMC) composition could provide high capacity, rate capability and high voltage operation. Cobalt is hard to be replaced due to its stabilizing and high electronic conductivity properties.

The  $LiMn_2O_4$  (LMO) spinel structure is a lower cost and safer alternative but shows lower capacity compared to the previously presented chemistry.

A suitable trade-off between price and performance is achieved by adding nickel and cobalt to the previously described structure (e.g.  $Li[Mn_{1.42}Ni_{0.42}Co_{0.16}]O_4$ ) (LNMO), while another opportunity for cathode material is the adoption of phosphates as  $LiFePO_4$  (LFP) [14].

Regarding anodic materials, efforts on researching alternatives to graphite lead to the development of both intercalation-based structure as  $Li_4Ti_5O_{12}$  (LTO) [15] and silicon-graphite composite [16] and alloying structures as Li/Ge, Li/Si, Li/Sn and Li/Sb [17].

Lithium titanate is characterized by no volume change over charge/discharge and operation at almost 1.5 V vs. Li+/Li, allowing to avoid the issue of lithium dendrites formation and electrolyte decomposition, while, as a drawback, provides a lower specific capacity compared to graphite (175 vs 372 mAh/g) [15].

The adoption of Si/Gr composite could guarantee an extremely high specific capacity (2426 mAh/g) as a nano/microstructured anode employing boron doped silicon and CNT wedging layer operating in synergy with graphite layer [16].

Considering alloying anodes, silicon could provide high specific capacity (4200 mAh/g) compared to germanium (1600 mAh/g), the latter feature two orders of magnitude higher Li+ diffusivity and electrical conductivity while ensuring lower working potential.

The main disadvantage of Li/Ge alloy are the high costs and high volume expansion/contraction over the charge/discharge processes.

Solution based on lithium germanate ( $Li_2GeO_3$ ) could allow to increase the specific capacity (2152 mAh/g) and reduce the costs [17].

Due to the low electronic conductivity of both electrodes, an aluminium foil is adopted at cathode and copper foil at anode as current collectors. It is required to employ a binder, such as polyvinylidene fluoride (PVdF) in order to provide structural resistance to the electrodes [18].

#### 1.3.1.2.2 Electrolytes

Regarding the composition of the electrolyte, lithium organic salts, such as the commonly adopted LiTFSI and LiFSI, are dissolved into an organic solvent, as ethylene carbonate (EC)

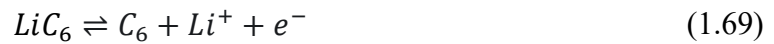
and dimethyl carbonate (DMC). A porous separator is adopted, allowing only ionic conduction, it is usually made of PE, PP or a composite of both materials.

Being the mechanical, thermal and electrical abuse conditions particularly dangerous, partly due to the side reactions involving the liquid electrolyte decomposition and leakage, the adoption of solid-state electrolyte (e.g. polymer based) is being considered due to higher intrinsic safety, at the price of higher costs and lower ionic conductivity.

### 1.3.1.2.3 LIBs reaction mechanism

An example of a basic LIBs operating mechanism is provided.

During the discharge phase, the deintercalation of  $\text{Li}^+$  at the anode occurs.



Ions are conducted towards the positive cathode, where they are housed in the metal oxide framework, and electrons are conducted throughout an external circuit from anode to cathode.



Being the full reaction:



In the charging phase the opposite process takes place, the rated voltage of the device is 3.6-3.7V.

During the first charge/discharge cycles, the decomposition of the electrolyte at the anode occurs, allowing the formation of an electrically insulating but lithium ions conductive solid layer, protecting the electrode from corrosion [13].

The formation of the solid electrolyte interphase (SEI) is essential for the correct functioning of the battery.

The operation within a limited SOC band, avoiding deep charge and deep discharge, would allow to preserve the performance of LIBs over cycling.

It's recommended to store and operate the battery within a narrow temperature range to reduce the impact of self-discharge and to avoid safety hazards, which might occur by direct exposition of the device to direct sunlight or to a different heat source. It is important not to open their casing to avoid disconnection with the internal safety circuit preventing fire and explosion [13].

### **1.3.2 Lithium Sulfur Batteries**

The basic cell, studied since the '60s, had a simple composition, presenting a lithium anode, a sulfur cathode and an organic electrolyte, while nowadays more complex structures are considered to assess most of the LSBs main defects.

Adopting metallic lithium in a LSB coin cell, the issue of dead lithium is a minor problem due to the excess of anode material compared to the cathode loading, considering the average anodic capacity being dozens of times higher than the cathodic one, the loss of anodic active material over cycling is negligible [19]

The presence of a current collector is mandatory to allow electronic conduction between the cathode and the external circuit, while the lithium electrode is highly conductive by itself, thus not requiring an extra component.

The development of these devices have not reached yet the commercial success of LIBs due to critical drawbacks, as the "shuttle effect", leading to capacity fading, strongly reducing the battery lifetime (200-300 cycles) and causing self-discharge.

#### **1.3.2.1 Sulfur**

Sulfur is a nonmetallic element, odourless, tasteless, very abundant on Earth and well distributed, thus it's cheap. It's present in its largest share in sulphides and sulphates.

Sulfur is also present in fossil fuels as coal and oil and mostly extracted from them by Frasch process, which consists in injecting a pressurized water vapour and air mixture in the reservoir to extract the molten material.

The presence of a residual sulfur share leads to SO<sub>x</sub> emissions as a combustion byproduct, reacting with oxygen and moisture producing sulphuric acid, leading to acid rains, thus acting as a local pollutant.

The adoption of sulfur as a cathodic material is an optimal choice considering its high specific capacity (1675 mAh/g) and cost reduction. Instead, its main issues are the volume variation of sulfur over its reaction and its insulant nature, requiring a large share of electronically conductive element (e.g. carbon/conducting polymers), resulting in a reduction in specific energy/energy density.

Despite its problems, the adoption of sulfur as a cathodic material is sustainable from an economic, social and environmental point of view, in substitution of rare transition metals as cobalt, resulting in one third of the costs compared to LIBs.

#### 1.3.2.2 LSB main reactions

The structure of LSB has been object of several studies to improve their performances: in this chapter the main chemical reactions occurring during the discharge are discussed.

The theoretical complete reaction which should drive the LSB operation is the following:



At the anode, lithium oxidation takes place:



At the cathode the reaction mechanism is complex and it will be analysed in detail.

The characteristic reactions underlying the operating behaviour of LSBs are still a matter of debate, several studies were performed over the last years, adopting different experimental techniques, to determine the reduction path of octasulfur [20].

The process of cathode lithiation and delithiation involves complex electrochemical and chemical steps, challenging to be introduced in a physical model of the system.

The main reactions determining the LSB charge/discharge behaviour are presented for a basic cell employing a standard C/S cathode, highlighting the ones representing the most relevant steps which are integrated in the model described and analysed in the present thesis.

### 1.3.2.2.1 Sulfur Dissolution

Studies performed on different cathode morphologies and C/S mixing degrees show no significant effect of these variables in determining the electrochemical performances, in contrast to the insulating property of sulfur, which should induce a high resistance in the solid-state reaction.

The reaction products ( $Li_2S_x$ ) would also dissolve, causing the loss of electrical contact, making the sulfur particle unusable for further reduction [21] (Figure 1.6).

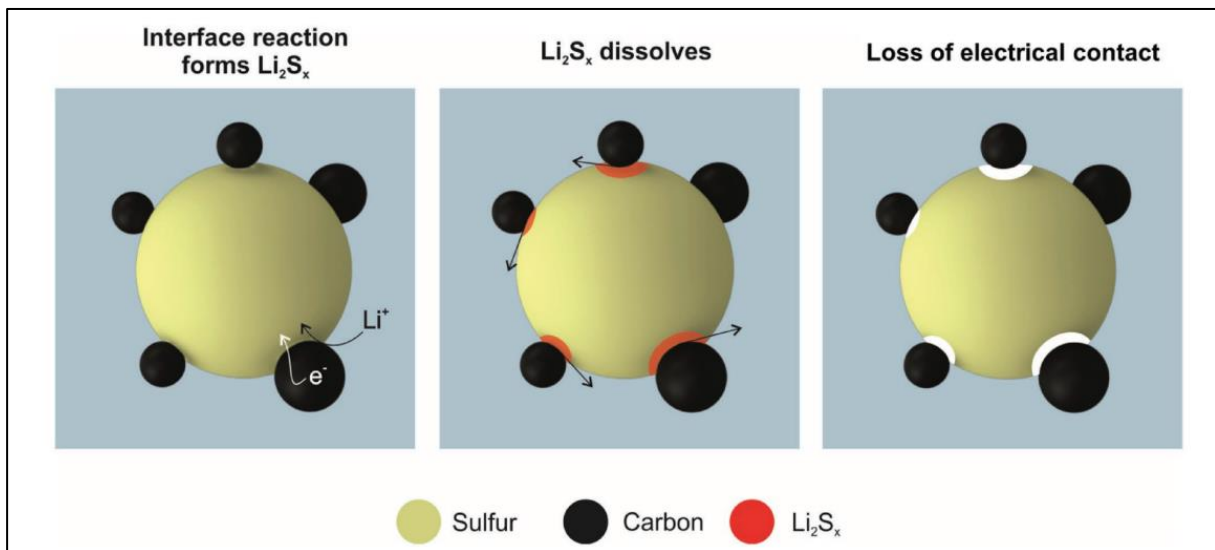


Figure 1. 6 – Loss of electrical contact in the case of solid-state  $S_8$  reduction [21]

Sulfur dissolution in the electrolyte solution is the key phenomenon solving the abovementioned issues, being only apparently in contrast with its proven low solubility in organic solvent. Usually what affects most the performances is the dissolution rate, which is not limiting at the low C-rates employed in LSB. [21].

The mentioned non-faradaic reaction (implemented in the model) occurs due to the continuous consumption of sulfur in the liquid phase over the discharge process, leading to the drop below the solubility limit of sulfur concentration in the solution.

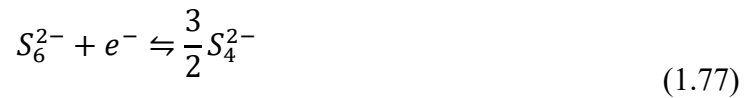


### 1.3.2.2.2 Sulfur reduction

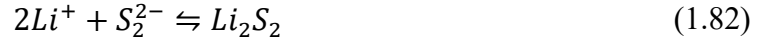
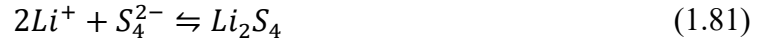
At the cathode, dissolved sulfur reacts with lithium ion, producing sulfides characterized by different chain lengths, known as lithium polysulphides (LPS), in a multi-step reduction process.

These salts are classified as “high order” (5-8 S atoms) and “low order” ones (1-4 S atoms).

The possible reaction pathways involving LPS are quite numerous, the ones acknowledged for the simulation model development consider the high solubility product of these species, thus representing the reduction reactions involving polysulphide anions (PS) as follow [22]:



During the discharge phase, long chains polysulphides are progressively reduced to small chains ones, while the opposite occurs during the charge. The LPS products are included in the model by precipitation reaction, this choice is not necessarily functional for short-chain LPS which might react by solid-state reduction.



At the end of the discharge phase, mostly  $Li_2S$  could be detected, being the final discharge product while other LPS are highly soluble in the electrolyte.

### 1.3.2.3 A focus on the role of polysulphides

As the fundamental mechanisms underlying LSBs operation are still a matter of research, there is no unequivocal consensus neither on the specific set of reactions characterizing the charge and discharge processes nor on their equilibrium and rate constants, which could be hard to assess, thus the following reactions involving PS, while considered worthy of mention, are not included in the model.

Polysulfides anions are present in the electrolyte both as singly charged radical monoanion and dianion, being symbiotic in a solution, as it could be expressed by [23]:



Interaction between polysulfides could occur by a comproportionation/disproportionation reaction, where two reactants (in this case both PS) contain the same element with different oxidation numbers the product is characterized by an intermediate one. The reverse process is also possible:



Polysulfides are in general highly reactive, sensible to air, moisture and to the type of solvent.

PS state in aqueous solution result in abundant  $S_4^{2-}$  and  $S_5^{2-}$ , while in polar non-aqueous solution are characterized by  $S_6^{2-}$  and  $S_8^{2-}$  higher concentration.

### 1.3.2.3.1 The Shuttle Effect

During the discharge the highly soluble long chain polysulfides leak from the cathode and migrate towards the anode, where they could directly react with lithium. This can cause both the precipitation of insoluble  $Li_2S$  (reducing the capacity and increasing ionic resistance) and the occurrence of disproportionation reactions, inducing locally produced PS.

This mechanism leads to a withdrawal of a share of the charging current which is purely dedicated to feed the shuttle effect. For example, charging at low C-rate, the current share could reach 100%, resulting in infinite charge.

PS shuttle dynamic could be expressed by the following first order ODE exploiting the knowledge of first plateau capacity  $q_H$ :

$$\frac{d[S_H]}{dt} = \frac{I}{q_H} - k_s[S_H] \quad (1.86)$$

Where  $[S_H]$  represents the concentration of high order polysulfides at anode,  $I$  the current and  $k_s$  the shuttle constant.

During the charge process ( $I = I_c > 0$ ), the increase of  $[S_H]$  is limited by the parasitic reduction reactions.

Solving the proposed ODE and performing further assumptions, the charge-shuttle factor is defined:

$$f_c = \frac{k_s[S_{total}]q_H}{I_c} \quad (1.87)$$

Analogously as the previous considerations,  $f_c < 1$  implies charging could be completed while  $f_c > 1$  implies that it won't [24].

### 1.3.2.3.2 Kinetics enhancing effects

Despite the abovementioned issues, PS are also involved in beneficial effects in LSB by enhancing the sulfur redox reaction kinetics. During the discharge phase, dissolution of PS allows a shorter path for both ions and electrons, increasing electronic and ionic conductivities.

By comproportionation reactions, the bulk sulfur structure could be dissolved in the electrolyte, resulting in sulfur redistribution over the electrode surface. The presence of high mobility PS migrating toward active spots, ready to be reduced over the conductive host surface, allows a strong increase of the area available for reaction (Figure 1.7).

The contribution to kinetics is also present in the charging phase by enhancing lithium sulphides oxidation.

Sulfur redistribution contributes to increase active material utilization and longer lifetime [19].

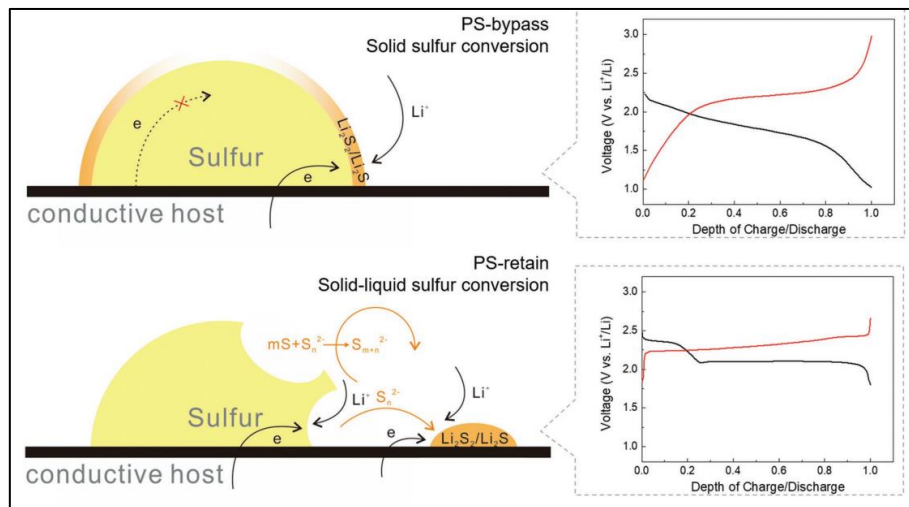


Figure 1. 7 – PS driven sulfur redistribution over the conductive host [19]

### 1.3.2.3.3 PS management techniques

Two strategies are adopted to manage PS, being PS-bypass and PS-retain.

The intent of PS bypass is to prevent the formation of PS anions by acting on the cathode or the electrolyte.

It is possible to act on the cathode structure by confining sulfur allotropes  $S_{2-4}$  in a microporous carbon matrix (<0.5 mm), spatially hindering the PS production, or adopting sulfurized organics as active material. Both the presented methodologies have the drawback of low sulfur content.

Focusing on the electrolyte, a low electrolyte/sulfur ratio (e.g. 3ml/g) would lower the costs but would also amplify PS concentration, thus their negative behaviour. A possible solution to hinder PS solubility is the adoption of Solid-State Electrolytes (SSEs) which are described in detail in a following paragraph.

Regarding PS Retain, the intent is to take advantage on the PS positive effects on kinetics while minimizing the shuttle effect, selected techniques belonging to this category are presented.

The PS confinement consists in the immobilization of PS by physisorption on carbon structure or chemisorption adopting polar binders, which would anchor them to conductive substrate and improve the kinetics.

This PS blocking option consists in blocking PS diffusion towards the anode by adopting an ion selective layer separator as by metal-organic framework (MOF) crystals or by an anion-repelling or size-selective polymers and inorganics.

An interlayer between the cathode and the separator made by carbon, metallic salts or functional polymers could help capture and reutilization of PS. Adopting polar materials for this scope could help enhancing kinetics of reactions, catalysing lithium sulphide precipitation.

The presence of  $LiNO_3$  in the electrolyte leads to the formation of a SEI rich in N and S (from PS reacting), preventing an excessive decomposition of the electrolyte and dendrites formation.

A second approach is the substitution of the anode with previously presented structures adopted for LIBs.

It could also be considered to adopt nonlithiated anode, to compensate for lithium absence, a  $Li_2S$  cathode must be adopted, with the advantages of lower volume expansion and higher thermal stability while the presence of encapsulated sulfur inhibits PS dissolution. The main drawbacks would be the high cost and air/moisture sensitivity.

To sum up, the PS-bypass allows to increase the cyclability and increase the anode sustainability by keeping its structure as simple as possible, while the PS-retain allows to increase the kinetics, capacity, voltage output and sulfur content of the cathode [23].

### 1.3.2.4 The LSB Cathode

#### 1.3.2.4.1 *Carbon-host structures*

LSB cathode could be composed by a carbon/sulfur mixture, where the first provides electronic conductivity and an electrochemically active surface, in which sulfur (present in a cyclo-S<sub>8</sub> rings), which is the active material, is embedded.

Carbon can be present in form of porous carbon framework, carbon nanotubes (CNTs), carbon nanofibers (CNFs) [19].

Porous carbon is a particularly suitable option in terms of high specific surface area and high sulfur loading.

Pores could be classified as micropores ( $d < 2$  nm), mesopores ( $2 < d < 50$  nm) and macropores ( $d > 50$  nm). The optimal management of the pore diameters would allow the ideal electrolyte infiltration and matching with the lithiation/delithiation expansion/contraction.

CNTs and CNFs present optimal properties, multiwall CNTs and mesoporous carbon fibers perform excellently in terms of PS retention and electrical conductivity.

Graphene is a valid alternative, due to its high electrical conductivity, its immobilizing effect on PS (hindering the shuttle effect) and the ability to adapt to sulfur volume change in charge/discharge phases [19].

Another opportunity is represented by hollow structured carbon, the main advantage of this option is the resulting high sulfur loading.

To compare the different carbon-based options, sulfur loading ranges between 50-80% while the gravimetric capacity ranges from 600-1000 mAh/g for 3D graphene and CNF/CNT to much higher values for porous and hollow carbon, peaking at 1200 mAh/g.

It is crucial to notice that the increase in sulfur loading doesn't lead to a proportional increase in capacity, being the electrical conductivity necessarily hindered.

The trade-off point in sulfur content depends on the topology of the structure, shifting to higher values for better designed ones [19].

#### 1.3.2.4.2 *Functionalized structures*

Carbon hosts develop weak interactions with polysulfides, therefore new functional cathodes with enhanced chemisorption properties could significantly improve the shuttle effect mitigation, by the interaction between polar functional groups and polar polysulphides.

The adoption of metal oxide as  $MnO_2$  is a possible choice due to the polar metal-oxygen bond which is effective in PS trapping by physisorption, yet its low electrical conductivity is detrimental thus, its combination with a conductive matrix is required.

Metal sulphides are a suitable alternative to MO, the polar bond with PS is weaker, reducing the risk of interacting with the Li-S bond in the PS structure, being beneficial for the integrity of sulfur active material and represents a more balanced option, (e.g., cobalt sulphides).

MS are better in PS retaining compared to carbon structure and better in kinetics performance compared to MO. The main problem is that their low electronic conductivity leads to a lower sulfur utilization, thus capacity loss. Combining sulphides nanostructures with a 3D conductive framework could solve the problem [19].

An alternative solution is implementing a molybdenum disulfide/polyaniline interlayer (MoS<sub>2</sub>/PANI), where the first material is both electronically conductive and performs PS blocking by physisorption, while the second improves the electrochemical performance of the cathode by its catalytic activity, enhancing the kinetics of PS conversion reactions [25].

An internal layer of graphitic carbon nitride ( $g - C_3N_4$ ) could physically interact with PS to trap them at cathode side [26].

#### 1.3.2.5 The LSB Electrolyte

The electrolyte has the fundamental role to allow ionic species transport while hindering electronic conduction to avoid internal short circuit.

The ideal electrolyte would also feature a high thermal stability and wide electrochemical window (no decomposition at working potentials), inhibit the shuttle effect (specific for LSBs), being also cheap, safe for the user and the environment (non-toxic).

#### 1.3.2.5.1 Non-aqueous liquid electrolytes

Commonly adopted solvents in lithium-ion batteries, as ethylene carbonate (EC) and diethyl carbonate (DEC), aren't suitable for LSBs as they irreversibly react with polysulfides.

The 1,3-dioxolane (DOL) shows high dissolution ability of polysulfides and stability in contact with metallic lithium. Along with 1,2-dimethoxyethane (DME) it represents an optimal choice, also considering that the potential range vs  $\text{Li}^+/\text{Li}$  is much lower than LIBs, included in the stability range of ether solvents.

Considering the solute employed, the organic lithium bis(fluorosulfonyl)imide (LiFSI) and lithium bis(trifluoromethanesulfonyl)imide (LiTFSI) are optimal choices due to their thermal stability, the opportunity to provide high ionic conductivity, good dissociation ability with DOL/DME solvent, leading to high initial capacity and the absence of side reactions with PS

LiTFSI allows better performance compared to LiFSI, in terms of both stability and capacity retention, but these structures seem more prone to allow LPS deposition at anode [24].

$\text{LiNO}_3$  is a widely used additive in LSB electrolytes, promoting the formation of  $\text{Li}_x\text{NO}_y$  enriched SEI, protecting the anode from corrosion. Discharging the LSB below 1.7V would lead to an irreversible reduction of  $\text{LiNO}_3$  on the cathode, negatively affecting the cyclability.

$\text{LiNO}_3$  also performs a catalytic activity in the formation of elemental sulfur at the end of the charging process.

The amount of free solvent has a major role in the dissolution ability of the LPS, as the higher it is the stronger are the intermolecular forces tearing apart LPS molecules. Also, the salts concentration plays a key role, as the initial increase in ionic conductivity is balanced, at specific concentrations, by the increase in viscosity limiting the diffusive effects.

High concentration of salt could show a beneficial effect in mitigating the lithium dendrite growth in the charging phase ( $> 4.0$  M LiFSI). Moreover, replacing metallic lithium anode with graphite anode, a high concentration of LiTFSI ( $> 5.0$  M) could be beneficial to mitigate PS diffusion and to allow compatibility with ether-based solvents [28].

#### 1.3.2.5.2 *Ionic Liquid Electrolytes*

Ionic Liquids are salts in the liquid state; therefore, they are entirely constituted by ions. They show suitable properties as low-flammability, high ionic conductivity, wide stability window and lithium dendrites formation inhibitions.

ILs with larger ions are found to have higher solubility for LPS, leading to steep capacity drop over cycling due to enhanced polysulfides shuttling, but inhibition of this behaviour could occur adopting specific anions as  $TFSI^-$  or  $PF_6^-$ .

High viscosity of these liquids is detrimental at high C-rate, but limitation on Li transportation might be overcome at slightly higher temperatures (60°C).

The adoption of ILs leads to the formation of a SEI characterized by a peculiar morphology, with beneficial impact on the anode corrosion protection.

At present, the high cost of this solution is the main disadvantage, hybrid solution mixing ILs and non-aqueous liquid electrolytes represents good compromise between costs and performances [28].

#### 1.3.2.5.3 *Solid-State Polymer Electrolytes*

Solid state electrolytes might significantly improve the intrinsic safety of the battery: the choice of specific polymers allows to avoid leakages and combustion in abuse conditions and the very low density helps increasing the specific energy of the battery.

The adoption of poly(ethylene oxide) (PEO) is optimal as a specific movement of the chain structure would allow  $Li^+$  migration.

To avoid phase transition from amorphous to crystalline, negatively impacting on ionic conductivity, the operation temperature of the battery must be close or higher than standard environmental one. The adoption of specific inorganic fillers might help adjusting the characteristic temperatures of the structures to more suitable values, by reducing the glass-transition temperature.

SPEs based electrolytes require specific lithium salts as LiTFSI or LiFSI, where the last one is preferred. Thus, a suitable coupling would be a LiFSI/PEO structure, characterized by good PS shuttle inhibition at low temperatures.

Reducing the price, increasing ionic conductivity and improving lifecycle are the current goals to be pursued [28].

#### 1.3.2.5.4 *Gel Polymer Electrolytes*

Gel is a semi-solid structure characterized by at least a liquid phase, when a solid phase is included, the liquid lies inside while avoiding the collapse of the system by its surface tension.

In GPEs the liquid electrolyte is trapped in the polymer, allowing good thermal and chemical stability, wide electrochemical window and might mitigate PS diffusion and lithium dendrite growth.

The structure could be PEO based, as SPEs, and might be adopted as bulk electrolyte or as a cathode coating layer [28].

#### 1.3.2.5.5 *Ceramic Electrolytes*

Ceramic electrolytes are an inorganic alternative electrolyte for LSBs, featuring a wide electrochemical window, thermal stability and suitable ionic conductivity.

Perovskites, particularly Lithium Lanthanum Titanate (LLTO), represent an interesting choice: their characteristic structure  $ABX_3$  comprises a large metal cation (as  $Ca^+$ ), a smaller transition metal cation (as  $Ti^{4+}$ ) and an anion (usually  $O^{2-}$ ).

NASICON ( $Na^+$  superionic conductor) is a material featuring a tunnel structure for  $Na^+$  transportation, where this cation could be replaced by  $Li^+$ , offering another valid choice among inorganic electrolytes [28].

### 1.3.2.5.6 Composite Electrolytes

Composite materials are developed with the purpose of exploiting the best characteristics of specific classes of materials and reducing at minimum their related drawbacks. These structures are composed by a matrix and one or more second phases, as particles, fibres or layers of different sizes, providing unique properties to the system.

An interesting solution is adopting a PEO-based matrix with ceramic nanoparticles as the previously mentioned LLTO to both decrease the PEO crystallinity and increase ionic conductivity [28].

A recap of the main properties of different classes of electrolytes is proposed in Figure 1.8.

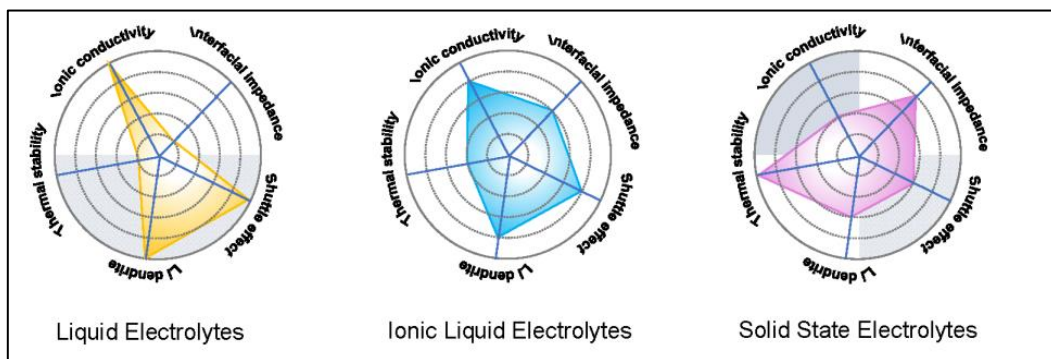


Figure 1. 8 – Main characteristics of different electrolytes typologies [28]

### 1.3.2.6 The LSB Anode

Different solutions are available to overcome the limitations of the commonly adopted metallic lithium anode.

Lithiated silicon-based anodes, also adopted in LIBs, could provide high theoretical capacity and energy density, while the extreme volume expansion might be overcome by the adoption of nanopowders. The first and second plateau potentials occur at lower voltage due to the lithium-silicon interaction at values of 2.1V and 1.85V, respectively. The adoption of tin as anode material is also under investigation, despite showing a lower capacity of 990 mAh/g.

The reaction mechanism is based on the formation of Li/Sn alloy [19].

## 2. Modelling

The main purpose of modelling is to simulate the operation of a device by performing virtual experiments, employing a set of mathematical equations to be solved adopting proper computational tools, to support activities improving the system design.

At first, it is required to analyse the device operation (PF), as can be seen in Figure 2.1. Then, a restricted number of major physical phenomena involved can be selected with the purpose to set fundamental equations (PM). Phenomena providing a milder contribution to the accuracy of the model can be neglected, and an error ( $e_m$ ), that causes the deviation of the analytical solution  $x$  from the real physical problem solution  $x_f$ , can be computed.

Secondly, if the equations are not analytically solvable (as in our case), a manipulation is compulsory to arrange them in a form to be solved by numerical methods (PN), introducing an error ( $e_t$ ) between the numerical solution  $x_n$  and  $x$ .

At last, the numerical methods must be solved by a computer, resulting in a further deviation  $e_a$  between its solution  $\hat{x}$  and  $x_n$ .

Every step brings into play a source of errors interplaying with each other in a nonlinear way. So, an exact representation of the data of a real experiment is not possible, but efforts in analysing the intermediate processes could lead to satisfying results (Figure 2.1).

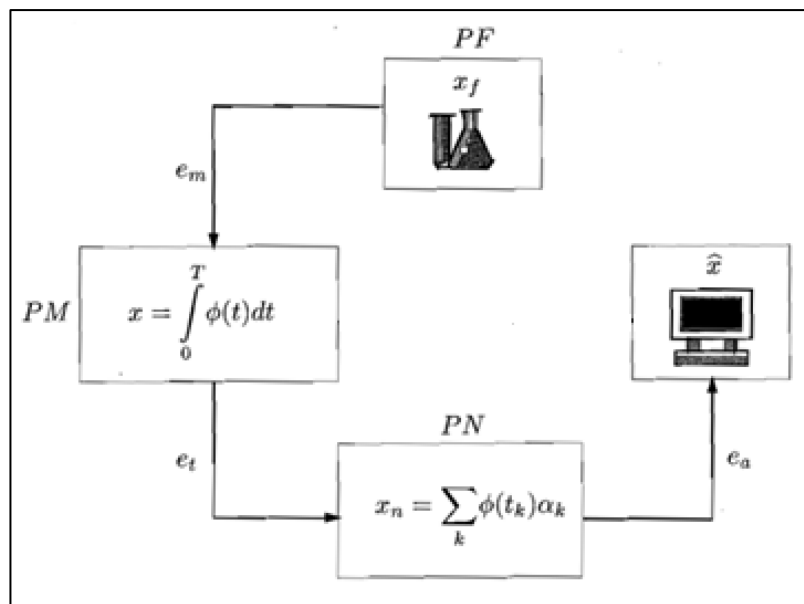


Figure 2. 1 - From the physical problem to the computational solution [29]

The goal of this thesis is to act on the equations parameters and shape in order to reduce as much as possible the source of error  $e_m$ , while the other deviations are due to the simulation software [29].

## 2.1 Modelling tool and interface

The program adopted to perform the modelling of LSB is COMSOL Multiphysics, a finite element analysis simulation tool able to solve coupled systems of algebraic equations, Ordinary Differential Equations (ODEs) and Partial Differential Equations (PDEs).

COMSOL presents a graphical user interface allowing to choose among several modules according to the prefixed study.

For this thesis, the Electrochemistry Module is employed, allowing to model electrochemical cells as fuel cells, electrolyzers and batteries, featuring specific tools to implement detailed description of each domain under analysis, as the anode, separator and cathode.

The effect of adopting different materials, geometry and operating conditions could be investigated.

The “Tertiary Current Distribution, Nernst Planck Interface” is selected to allow the description of the current and electric potential distribution in an electrochemical cell. The effect of transport of charged and uncharged species is considered, being driven by diffusion, electromigration and convection, by adopting the Nernst-Planck Equations.

The “Time-Dependent with Initialization Study” is employed for transient electrochemical problems containing a Deformed Mesh physics interface.

The study consists of two steps: a “Current Distribution Initialization” step, which solves for the potential fields only, followed by a “Time Dependent study step”, for which the field computed by the first step is used as initial values.

The charge conservation is ensured by the condition of Electroneutrality, allowing to calculate the concentration of a dependent species, selected to be the anion of the lithium salt, knowing the value of the concentrations of other species [30].

Since the radius of the analyzed cell is much bigger than the thickness, the edge effects could be neglected, thus 1-D study can be selected.

## 2.2 The Porous Electrode Theory (PET) applied to LSBs

Porous electrodes allow an intimate contact between the electrode materials and the electrolyte, that permeates the voids, increasing the available specific surface area and promoting reaction kinetics [31].

The need of a specific theory to model these systems arises from their complexity since polarization inducing transport phenomena occurs both in series and in parallel throughout the device,

The geometry of the pores is neglected: the morphology of the structure is indeed defined by averaged parameters that describe the characteristics of a volume of the structure. This volume is small enough to grasp the macroscopic change in characteristic variables within the electrode/separator, but much larger than the pores volume [31].

Being the electrode of a lithium-sulfur battery constituted by a mixture of porous electronically conducting and non-conducting solids, where the first is carbon black and the second is sulfur (the active material), the averaging procedure is both spatial and material based.

Parameters as the porosity  $\epsilon$ , which is the ratio between the pore volume and the total volume, and tortuosity  $\tau$ , which is the ratio between the length of a curved path and the segment connecting the ends, are defined according to the following formulas.

$$\epsilon = \frac{V_{void}}{V_{tot}} \quad (2.1)$$

$$\tau = \frac{L_p}{L_{cv}} \quad (2.2)$$

Where  $L_p$  represent the effective path of a particle throughout a control volume and  $L_{cv}$  its effective thickness, as shown in Figure 2.2.

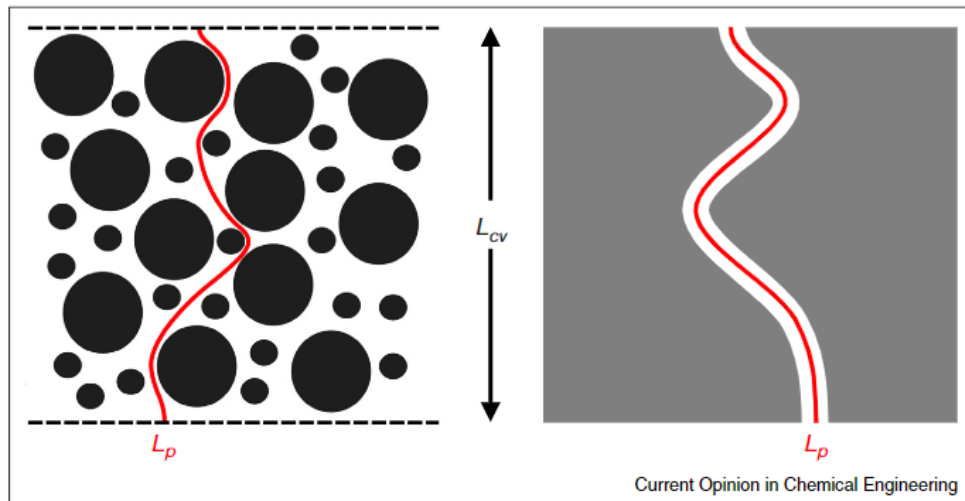


Figure 2. 2 - Graphical representation of tortuosity [31]

Superposition principle is employed to account for the presence of different phases within the same structure.

The solution of the equations provides the spatial distribution and time evolution of relevant properties, to analyze the charge and mass transport phenomena and compute the kinetic contributions to the system behaviour.

PET has been adopted by Kumaresan [22] and later by Zhang [32] to describe LSB behaviour by solving the characterizing equations for both the cathode and the separator, while the presence of the anode, has been included in the form of boundary conditions.

## 2.2.1 Model Equations

### 2.2.1.1 Mass transfer equations

The Nernst-Planck equation extends Fick's laws for diffusion to model charged species transport affected by the presence of electric field.

To fit into the Porous Electrode Theory, proper adaptation of the equation is required, along with the explication of the molar flux ( $N_i$ ) driving forces.

Considering the material balance in the porous phase:

$$\frac{\partial \epsilon C_i}{\partial t} = -\nabla \cdot \mathbf{N}_i + r_i - R_i \quad (2.3)$$

$$\mathbf{N}_i = C_i \mathbf{u} - D_i^{eff} \nabla C_i - z_i \frac{D_i^{eff}}{RT} F C_i \nabla \phi_2 \quad (2.4)$$

The equation (2.3) is a volume averaged continuity equation, describing the rate of change of the  $i$ -th species concentration in time due to the accumulation/depletion of the species by its motion ( $\nabla \cdot \mathbf{N}_i$ ), or due to its participation in electrochemical or in non-faradaic reactions, through source and sink terms ( $r_i$ ) and ( $R_i$ ).

The term  $\mathbf{N}_i$  represents the molar flux, a vector quantity describing the direction and magnitude of molar flow rate of the  $i$ -th chemical species per unit area.

Considering  $C_i$  as the solution-phase concentration of the  $i$ -th species,  $\epsilon C_i$  will represent the concentration in the porous phase of the material.

A relevant number of transport problems are set following the approach  $\dot{F} \propto \nabla C$ , linearly relating a term representing a flux  $\dot{F}$  of mass or energy to a potential gradient. As an example, in Fourier's law the heat flux is related to the temperature gradient, in Ohm's law the charge flux (current) is related to electric potential gradient [33].

The same approach is adopted in the equation (2.4), describing the motion of ionic species in the porous medium as a function of advection, concentration gradient and electrolyte-phase potential gradient, where  $D_i^{eff}$  is the effective diffusion coefficient.

The advective term  $C_i \mathbf{u}$  is null in the specific case of LSB simulation as the solvent is at rest.

The second term of the equation is valid for both ions ( $Li^+$ ,  $S_8^{2-}$ ,  $S_6^{2-}$ ,  $S_4^{2-}$ ,  $S_2^{2-}$ ,  $S^{2-}$ ) and not charged species ( $S_{8d}$  and LPS) due to the exclusive contribution of diffusive flux by concentration gradient, while the third term is accounted for charged species only [31].

### 2.2.1.2 Thermodynamics equation

The previously cited OCV obtained by the Nernst Equation is adequately modified, considering that the concentrations of reactants and products deviate from the standard conditions ( $U_j^\theta$ ) in the initial state  $C_{i,ref}$ . A correction factor of 1E3 is applied to perform the conversion from mol/l to mol/m<sup>3</sup>:

$$U_{j,ref} = U_j^\theta - \frac{RT}{n_j F} \sum s_{i,j} \ln \left( \frac{C_{i,ref}}{10^3} \right) \quad (2.5)$$

Where  $s_{i,j}$  is the stoichiometric coefficient in the j-th reaction of the i-th species and  $n_j$  is the number of electrons transferred.

$U_j^\theta$  must be defined for each of the previously discussed reduction reaction involving all the species of sulfur and for the lithium oxidation.

### 2.2.1.3 Electrochemical kinetics equations

The extended Butler-Volmer equation is adopted to predict the current densities  $i_j$ , at the interface between solid and electrolyte, arising from electrochemical reaction, considering the influence of the mass transfer:

$$i_j = i_{0j} \left\{ \prod_i \left( \frac{C_i}{C_{i,ref}} \right)^{p_{i,j}} \exp \left( \frac{0.5F}{RT} \eta_j \right) - \prod_i \left( \frac{C_i}{C_{i,ref}} \right)^{q_{i,j}} \exp \left( \frac{0.5F}{RT} \eta_j \right) \right\} \quad (2.6)$$

Being  $p_{i,j}$  and  $q_{i,j}$  stoichiometric coefficient for species to be oxidized and reduced, the last ones with negative sign.

This expression considers the spatial distribution of the concentration of the electroactive species in the precise location of the reaction, which is different from the reference one.

The activation overpotential of the j-th reaction is expressed as:

$$\eta_j = \phi_1 - \phi_2 - U_{ref,j} \quad (2.7)$$

Merging the approximation of the Butler Volmer Equations and Porous Electrode Theory, the total voltage drop between the electrode surface and the bulk electrolyte is considered to be localized within the Stern layer (BV). This one is estimated to be small enough compared to the volume of the pores (PET) such that, by the continuum modeling approach, two potential values for the same point in space  $\mathbf{P}(x, y, z)$  could be defined. These two potentials,  $\phi_1(\mathbf{P})$  and  $\phi_2(\mathbf{P})$ , represent the solid-phase potential and the electrolyte-phase potential, respectively [31].

The reference exchange current density is strongly influenced by the specific electrolyte adopted in the lithium-sulfur battery under analysis.

The parameter  $r_i$  represents the rate of electrochemical reactions, related to the current densities by:

$$r_i = a_v \sum_j \frac{S_{i,j} i_j}{n_j F} \quad (2.8)$$

Where  $a_v$  is the specific surface area of the porous medium.

Each species might be involved in multiple electrochemical reactions, thus the contribution of each j-th one should be included to assess its impact in concentration variation.

#### 2.2.1.4 Electroneutrality and charge conservation

Considering the EDL theory, the charge carrier's net electrostatic effect in a solution is confined in a region of space delimited by the Debye length, where this interface layer lays between the charged conductive solid material and the bulk of the solution.

Outside this region, the condition of electroneutrality effectively holds.

As the non-electroneutral volume accounts for a minimum share of the total volume of the pore, the condition of electroneutrality is extended, as an approximation, to the total volume of the pores.

The solid-phase current  $\mathbf{i}_s$  is expressed as:

$$\mathbf{i}_s = -\sigma_s \nabla \phi_1 \quad (2.9)$$

which is proportional to the gradient of  $\phi_1$  by the electronic conductivity  $\sigma_s$ .

Neglecting advection, the electrolyte phase current is related to the molar fluxes by:

$$\mathbf{i}_e = F \sum_i z_i \mathbf{N}_i = -\sigma_i \nabla \phi_2 - F \sum_i (z_i D_i^{eff} \nabla C_i) \quad (2.10)$$

$$\sigma_i = \sum_i \left( z_i^2 \frac{D_i^{eff}}{RT} F^2 C_i \right) \quad (2.11)$$

At the electrolyte-solid interface, the ionic current is produced by electrochemical reactions:

$$\nabla \cdot \mathbf{i}_e = a_v \sum_j i_j \quad (2.12)$$

The electroneutrality condition leads to the current continuity equation:

$$\nabla \cdot \mathbf{i}_e + \nabla \cdot \mathbf{i}_s = 0 \quad (2.13)$$

Thus, in the porous electrode, charge could be transferred between ionic and electronic species, not created nor destroyed.

Considering the phenomena occurring in a battery separator, the solid-phase current density is null as the second term of the latter equation, thus charge balance occurs within the ionic species:

$$\sum_i z_i C_i = 0 \quad (2.14)$$

#### 2.2.1.5 Morphological and non-faradaic reactions kinetics relationships

The specific area of the porous medium  $a_v$  is expressed as a function of the change in porosity as precipitates form at the electrode:

$$a_v = a_0 \left( \frac{\epsilon}{\epsilon_0} \right)^\xi \quad (2.15)$$

where  $a_0$  is the initial specific surface area of the electrode and  $\xi$  describing the morphology of the precipitate.

Regarding diffusion, the porous cathode and the separator are considered as media constituted by two phases, the solid material and the electrolyte, where the first one is referred to as insulating, being the species transport negligible.

The bulk diffusion coefficients must be related to the effective diffusion coefficients. High porosity promotes the  $i$ -th particle motion throughout the medium, while high tortuosity hinders the process:

$$D_i^{eff} = D_i \left( \frac{\epsilon}{\tau_f} \right) \quad (2.16)$$

Where  $\tau_f$  is the tortuosity factor, related but not equal to tortuosity  $\tau$ .

Adopting the Bruggeman relationship in the case of spherical insulating particles [33]:

$$\tau_f = \epsilon^{-\frac{1}{2}} \rightarrow D_i^{eff} = D_i(\epsilon)^{1.5} \quad (2.17)$$

The concentration evolution in time is also affected by non-faradaic reactions as dissolution and precipitation, where their rate is expressed as follows:

$$R_i = \sum_k \gamma_{i,k} R'_k \quad (2.18)$$

Where the  $k$ -th solid species reaction involved is denoted by a  $R'_k$ , that is the rate of reaction, while the number of ionic species involved is  $\gamma_{i,k}$ .

The parameter  $R'_k$  is determined by the expression below:

$$R'_k = k_k \epsilon_k \left[ \prod_i C_i^{\gamma_{i,k}} - K_{sp,k} \right] \quad (2.19)$$

Being  $k_k$  the rate constant of precipitation/dissolution,  $\epsilon_k$  the volume fraction of the  $k$ -th solid species and  $K_{sp,k}$  the solubility product of  $k$  in the electrolyte.

The proportionality  $R'_k$  with  $\epsilon_k$  states that the rate of reaction increases with the amount of product which is already precipitated. The product precipitating/dissolving in a LSB includes LPSs and solid sulfur.

It is crucial to determine the rate of change in morphology with time in the domain of cathode and separator, because it affects the diffusion phenomena:

$$\frac{\partial \epsilon_k}{\partial t} = \tilde{V}_k R'_k \quad (2.20)$$

Thus, the volume fraction for the k-th species changes proportionally to the corresponding rate of reaction, converted by a factor of the molar volume  $\tilde{V}_k$ .

The change in pore volume fraction of the domains of cathode and of separator is related to the expression above by the following relationship:

$$\frac{\partial \epsilon}{\partial t} = - \sum_k \frac{\partial \epsilon_k}{\partial t} = - \sum_k \tilde{V}_k R'_k \quad (2.21)$$

Thus, if precipitation overcomes dissolution, the porosity will increase and viceversa [31].

## 2.2.2 Boundary Conditions

Boundary conditions are required to express how the LSB interacts with the external environment by defining the mass/charge transport and setting reference values for potentials; both Kumaresan and Zhang applied the same BCs to their model.

### 2.2.2.1 Anode/Separator interface

Ten BCs are required at the anode/separator interface ( $x = 0$ ) due to the presence of ten differential equations describing the separator behaviour.

The first one expresses a reference for solid-phase potential, prescribing a null value at the anode:

$$\phi_1(0) = 0 \quad (2.22)$$

No molar flux crosses the anode boundary except for  $\text{Li}^+$  ions, which are set to be generated to account for the anodic reaction of lithium oxidation without the need to model the electrode, thus 8 BCs are imposed:

$$N_i(0) = 0 \quad (2.23)$$

$$|N_{\text{Li}}(0)| = \frac{i_{\text{Li}}}{F} \quad (2.24)$$

The 10<sup>th</sup> BC is an obvious consequence of the latter one and, so an ionic current density is imposed:

$$i_e(0) = FN_{\text{Li}} \quad (2.25)$$

#### 2.2.2.2 Separator/Cathode interface

Since the separator is ionically conductive, the molar fluxes of the species is preserved, along with the ionic current density:

$$N_i|_{L_s}^- = N_i|_{L_s}^+ \quad (2.26)$$

$$i_e|_{L_s}^- = i_e|_{L_s}^+ \quad (2.27)$$

Being  $L_s$  the thickness of the separator.

The electronically insulating nature of the separator leads to a null solid-phase current density crossing the interface:

$$i_s(L_s) = 0 \quad (2.28)$$

The imposed BCs are ten as the differential equations applied at both sides of the interface.

### 2.2.2.3 Cathode/Current collector interface

The current collector is employed uniquely to allow solid-phase current exchange, being not porous. The transport of species across the interface with the cathode is not allowed, thus:

$$N_i(L_s + L_c) = 0; \quad (2.29)$$

$$i_e(L_s + L_c) = 0 \quad (2.30)$$

Being  $L_c$  the thickness of the cathode.

The solid-phase current density depends on the applied current density, which is the ratio between the applied current  $I_{app}$  and the current collector area  $A$ :

$$i_s(L_s + L_c) = \frac{I_{app}}{A} \quad (2.31)$$

The imposed BCs are ten as the differential equations to be solved at the porous cathode.

## 2.3 Analysis of the models available in the literature

The Kumaresan and Zhang models are described and the differences in terms of adopted parameters are highlighted. The reactions occurring in each domain are depicted in Figure 2.3.

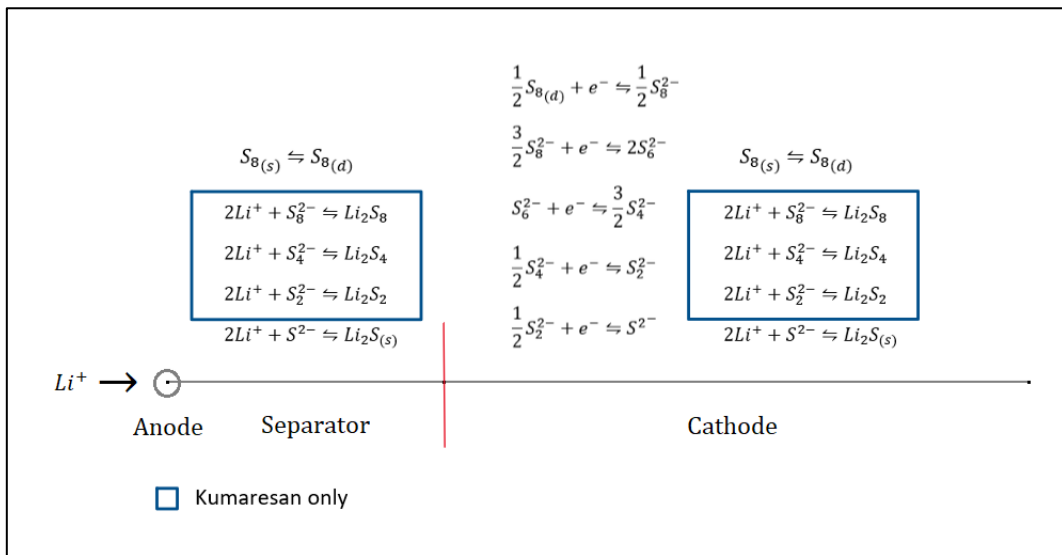


Figure 2. 3 – Visual comparison between Kumaresan and Zhang model

### 2.3.1 Comparison between K. and Z. adopted parameters

As a simplifying assumption, the only lithium polysulphides considered is  $Li_2S$  as higher orders LPS are neglected in Zhang model due to their high solubility products.

A list of the model parameters to be determined is presented.

- ❖  $D_i$ : diffusion coefficient of the i-th species in the electrolyte;
- ❖  $C_{i,ref}$ : reference/initial concentration of the i-th species in the electrolyte;
- ❖  $\epsilon_{x,0}$ : reference/initial volumetric fraction of the electrolyte in the separator/cathode (x);
- ❖  $\epsilon_{y,x}$ : volumetric fraction of the solid species (y) in the separator/cathode (x);
- ❖  $A_{cell}$ : cross sectional area;
- ❖  $a_{v,0}$ : specific surface area of the porous cathode;
- ❖  $\sigma_s$ : electronic conductivity of the cathode;
- ❖  $k_{s,j}$ : rate constant of the j-th non faradaic reaction;
- ❖  $K_{sp,j}$ : solubility product of the j-th non faradaic reaction;
- ❖  $i_{0,j}$ : exchange current density for the j-th faradaic reaction at  $C_{i,ref}$ ;
- ❖ c-rate;
- ❖  $T$ : operating temperature
- ❖  $E_j^0$ : standard reduction potential of the j-th semi-reaction with reference to the anodic one;
- ❖ Nominal Capacity;

All the terms defined as  $\alpha_0$  or  $\alpha_{ref}$  represent initial conditions to be set in order to solve the equations (Table 2.1).

Table 2. 1 - Kumaresan and Zhang list of parameters

Parameter	Kumaresan	Zhang	UM	Description
D_Li_1p	1E-10	8,80E-13	m <sup>2</sup> /s	Diffusion coefficient, $Li^+$
D_S8	1E-09	8,80E-12	m <sup>2</sup> /s	Diffusion coefficient, $S_{8(d)}$
D_S8_2m	6E-10	3,50E-12	m <sup>2</sup> /s	Diffusion coefficient, $S_8^{2-}$
D_S6_2m	6E-10	3,50E-12	m <sup>2</sup> /s	Diffusion coefficient, $S_6^{2-}$
D_S4_2m	1E-10	1,75E-12	m <sup>2</sup> /s	Diffusion coefficient, $S_4^{2-}$
D_S2_2m	1E-10	8,80E-13	m <sup>2</sup> /s	Diffusion coefficient, $S_2^{2-}$
D_S_2m	1E-10	8,80E-13	m <sup>2</sup> /s	Diffusion coefficient, $S^{2-}$

D_A_1m	4E-10	3,50E-12	m <sup>2</sup> /s	Diffusion coefficient, A <sup>-</sup> (salt anion)
c_Li_1p_ref	1001,04	1001	mol/m <sup>3</sup>	Reference concentration, Li <sup>+</sup>
c_S8_ref	19	19	mol/m <sup>3</sup>	Reference concentration, S <sub>8</sub>
c_S8_2m_ref	0,178	0,18	mol/m <sup>3</sup>	Reference concentration, S <sub>8</sub> <sup>2-</sup>
c_S6_2m_ref	0,324	0,32	mol/m <sup>3</sup>	Reference concentration, S <sub>6</sub> <sup>2-</sup>
c_S4_2m_ref	0,02	0,02	mol/m <sup>3</sup>	Reference concentration, S <sub>4</sub> <sup>2-</sup>
c_S2_2m_ref	5,229E-07	5,23E-07	mol/m <sup>3</sup>	Reference concentration, S <sub>2</sub> <sup>2-</sup>
c_S_2m_ref	8,267E-10	8,27E-10	mol/m <sup>3</sup>	Reference concentration, S <sup>2-</sup>
c_A_1m_ref	1000	1000	mol/m <sup>3</sup>	Reference concentration, A <sup>-</sup>
L_sep	9E-06	2,50E-05	M	Separator thickness
L_pos	41E-06	2,00E-05	M	Electrode thickness
A_cell		0,28	m <sup>2</sup>	Cell area
Av_0	132762	132762	m <sup>2</sup> /m <sup>3</sup>	Specific surface area
epsl_sep_0	0,37	0,5	-	Electrolyte volume fraction of separator without deposits
epsl_pos_0	0,778	0,7	-	Electrolyte volume fraction of positive electrode without deposits
eps_S8_s_sep_0	1,00E-12	1,00E-12	-	Initial volume fraction in separator of S <sub>8</sub> (s)
eps_S8_s_pos_0	0,16	0,166	-	Initial volume fraction in electrode of S <sub>8</sub> (s)
eps_Li2S_s_sep_0	1,00E-07	1,00E-07	-	Initial volume fraction in separator of Li <sub>2</sub> S(s)
eps_Li2S_s_pos_0	1,00E-07	1,00E-07	-	Initial volume fraction in electrode of Li <sub>2</sub> S(s)
sigma_s	X	1	S/m	Electric conductivity, electrode
k_S8_s	1	5	1/s	Rate constant, S <sub>8</sub> (s) deposition-dissolution
Ksp_S8_s	19	19	mol/m <sup>3</sup>	Solubility product

Vm_S8_s	1,24E-04	1,24E-04	m <sup>3</sup> /mol	Molar volume, S <sub>8</sub> (s)
k_Li2S_s	27,5	3,45E-05	m <sup>6</sup> *mol <sup>-2</sup> /s	Rate constant, Li <sub>2</sub> S <sub>(s)</sub> deposition-dissolution
Ksp_Li2S_s	3E-05	1,00E+02	mol <sup>3</sup> *m <sup>-9</sup>	Solubility product
Vm_Li2S_s	2,768E-05	2,40E-05	m <sup>3</sup> /mol	Molar volume, Li <sub>2</sub> S <sub>(s)</sub>
M_Li2S_s	(32,07+2*6,94)	(32,07+2*6,941)	g/mol	Molar mass, Li <sub>2</sub> S <sub>(s)</sub>
M_S8_s	8*32,07	8*32,07	g/mol	Molar mass, S <sub>8</sub> (s)
i0_Li_ref	0,394	0,5	A/m <sup>2</sup>	Exchange current density at reference concentrations, Li/Li <sup>+</sup> reaction
i0_1_ref	1,972	1,9	A/m <sup>2</sup>	Exchange current density at reference concentrations, reaction 1
i0_2_ref	0,019	0,02	A/m <sup>2</sup>	Exchange current density at reference concentrations, reaction 2
i0_3_ref	0,019	0,02	A/m <sup>2</sup>	Exchange current density at reference concentrations, reaction 3
i0_4_ref	1,97E-04	2,00E-04	A/m <sup>2</sup>	Exchange current density at reference concentrations, reaction 4
i0_5_ref	1,97E-07	0,00000002*0+2e-7	A/m <sup>2</sup>	Exchange current density at reference concentrations, reaction 5
C	X	X		C-rate
T	30	30	degC	Temperature
E0_Li+	0	0	V	Equilibrium potential at STC Li/Li <sup>+</sup> reaction

E0_1	2,39	2,41	V	Equilibrium potential at STC reaction 1
E0_2	2,37	2,35	V	Equilibrium potential at STC reaction 2
E0_3	2,24	2,23	V	Equilibrium potential at STC reaction 3
E0_4	2,04	2,03	V	Equilibrium potential at STC reaction 4
E0_5	2,01	2,01	V	Equilibrium potential at STC reaction 5
Nominal Capacity	X	3,4	Ah	Nominal Capacity
b	1,5	1,5	-	Bruggeman Coefficient

The discrepancy of the presented parameters between the two models is partially due to the adoption of different electrolyte, as confirmed by Zhang, describing a “*sulfolane containing solvent*”, exhibiting a higher viscosity compared to ether-based solvent, while the composition of Kumaresan electrolyte is unknown. The discrepancy is also due to specific modeling preferences, as explained in the following paragraph.

Focusing on the reference concentration, the (a) values are assumed while the (b) values are stated to be calculated on the OCP.

Table 2. 2 - Focus on OCV discrepancy

Zhang	OCPi (V)	OCPi-OCP_Li (V)	Kumaresan	OCPi (V)	OCPi-OCP_Li (V)
Eeq_Li_ref	0.0058502	-	Eeq_Li_ref	0.00585	-
Eeq_1_ref	2.4709	2.4650498	Eeq_1_ref	2.451	2.4451498
Eeq_2_ref	2.4326	2.4267498	Eeq_2_ref	2.4515	2.4456498
Eeq_3_ref	2.4438	2.4379498	Eeq_3_ref	2.4541	2.4482498
Eeq_4_ref	2.447	2.4411498	Eeq_4_ref	2.457	2.4511498
Eeq_5_ref	2.4576	2.4517498	Eeq_5_ref	2.4576	2.4517498

By rearranging the Nernst Equation, the following formula could be implemented:

$$C_{red} = \left\{ C_{ox}^{vox} \exp \left[ - \left( E_{eqref,i} - E_{eq,i}^0 \right) \frac{ZF}{RT} \right] \right\}^{\frac{1}{v_{red}}} \quad (2.32)$$

As its results match with the provided numerical values, its adoption in the simulation software would allow to compute automatically reference concentration variation.

Focusing on the standard reduction potentials (Table 2.2), the suggested values vary slightly between the studies, while the reference OCPs, which should be equal between the different reactions, deviate much more in the second model compared to the first one.

While the rate constant for  $S_8$  dissolution slightly differs, the deviation in its solubility product by 7 orders of magnitude is significant.

### 2.3.2 A focus on the Zhang model

#### 2.3.2.1 Analysis on the dissolved species concentrations over the discharge

In Figure 2.4, the discharge curve at C/10 of a simulated LSB is depicted, along with the evolution of the average concentration of the dissolved species, over the discharge capacity, with the purpose of analysing the time evolution of these quantities.

As the discharge begins, dissolved octasulfur is available to react and its concentration is a function of two phenomena resulting in opposite effects. The first is the reduction to  $S_8^{2-}$  that implies its depletion, while the second is the material dissolution from the solid structure, that replenishes it.

At the end of the first plateau of the discharge curve, the depletion strongly overcomes dissolution, thus  $C_{S_8(d)}^{avg}$  steeply reduces, while  $C_{S_8^{2-}}^{avg}$  peaks and  $C_{S_6^{2-}}^{avg}$  become the highest among long chain PS.

Over the descending branch of the discharge curve, both  $C_{S_8(d)}^{avg}$  and  $C_{S_8^{2-}}^{avg}$  become negligible, while the proceeding reduction reactions lead to the supersaturation peak, where the

predominant PS species is  $S_4^{2-}$  and  $C_{S_4^{2-}}^{avg}$ ,  $C_{S_2^{2-}}^{avg}$ ,  $C_{S^{2-}}^{avg}$ ,  $C_{Li^+}^{avg}$  reach their maximum over the discharge process.

The effect of  $S_8$  dissolution could be clearly observed by the increase in cathode porosity from the beginning of the discharge up to half the descending branch capacity (Figure 2.5).

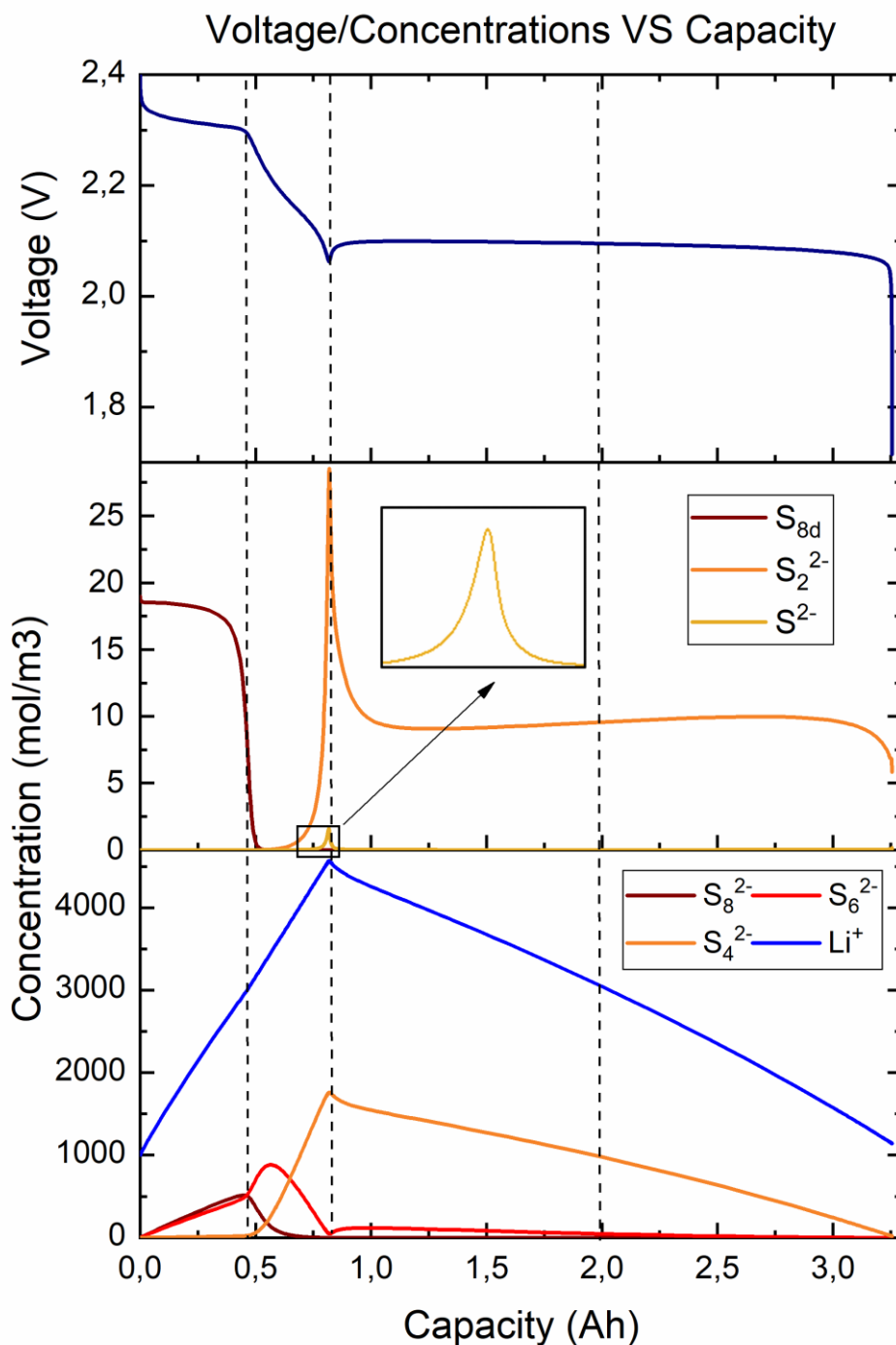


Figure 2. 4 – Evolution of the dissolved species average concentrations over the discharge

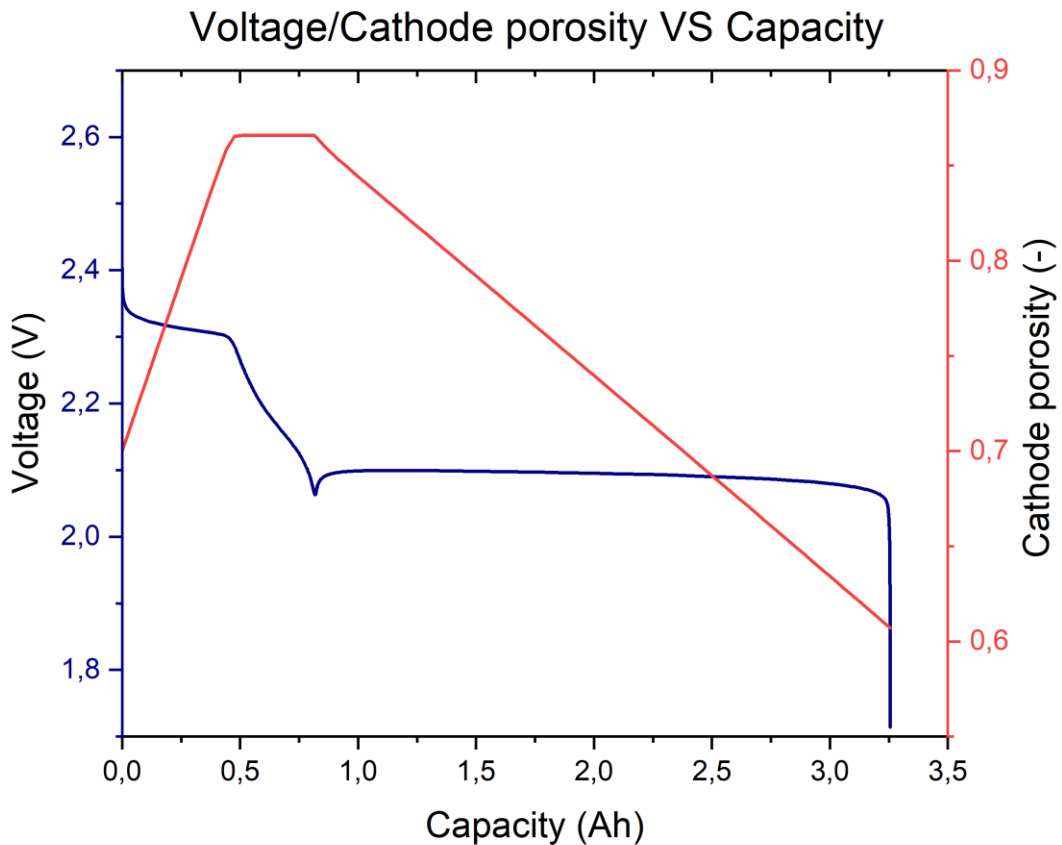


Figure 2. 5 - Evolution of the cathode porosity over the discharge

The reversal in the trend of  $C_{Li^+}^{avg}$  is a clear indicator of the kinetic insurgence of  $Li_2S$  precipitation, that is the only phenomenon responsible for the sink term in  $Li^+$  balance equation.

The cathodic volumetric fraction of  $Li_2S$  increases, lowering the cathode porosity, along with the depletion of intermediate chain PS, which are converted into short chain species.

The only noteworthy behaviour occurring over the second plateau is the trend of  $C_{S_2^{2-}}^{avg}$ , whose value is approximately constant due to its kinetically balanced electrochemical production and consumption.

### 2.3.2.2 Sensitivity of the model to external conditions

In this paragraph, the results of Zhang model sensitivity to external conditions are presented, varying the applied current and temperature, while adopting its basic geometrical and physico-chemical parameters.

#### 2.3.2.2.1 *Parametric sweep on C-rates*

One of the pillars of Zhang’s model is the reduction of the diffusion coefficients orders of magnitude, compared to the values proposed by Kumaresan, to effectively reduce the discharge capacity when increasing the applied C-rate.

In his paper, Zhang tests his model to highlight the relevant capacity drop in predicted discharge curves by increasing the applied current, limiting its sensitivity analysis from C/2 to 1C.

The model sensitivity has been extended to lower c-rates, being significantly more of interest as LSBs are adopted as “energy batteries” (slow charge/discharge).

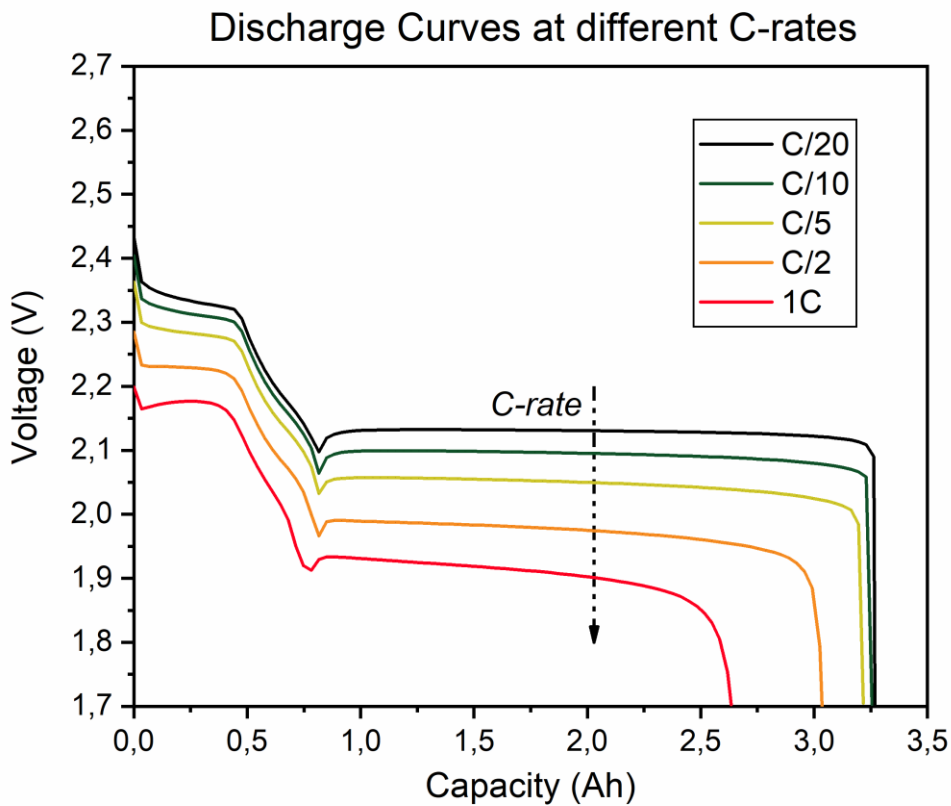


Figure 2. 6 - Extending Zhang model self-testing to lower c-rates

By figure 2.6, it's possible to evaluate how the C-rate affects relevant characteristic features of the discharge curve.

Regarding the first plateau, a mild polarization effect occurs while not affecting its shape up to C/5, while the polarization strongly increases and its voltage behaviour is mostly affected in C/2 and 1C, where a local voltage maximum is spotted.

The descending branch steepness and capacity is almost not affected, while the supersaturation peak before the second plateau widens, probably due to a kinetic limitation of  $Li_2S$  precipitation to restore the solvent viscosity, reducing the amount of free  $Li^+$  and  $S^{2-}$  ions in the electrolyte.

Figure 2.6 clearly shows that the predictivity of the model in terms of C-rate dependant capacity fade strongly reduces towards C/20, this phenomenon could be explained by considering the underlying rationale of the Zhang assumption.

The system response due to the slow transport of lithium ions across the cell results in the PS motion towards the separator to compensate for the high local  $Li^+$  concentration (electroneutrality), causing the loss of active material.

It's appropriate to depict this phenomenon by plotting the spatial distribution of ions,  $S_4^{2-}$  (as PS representative) and  $Li^+$  at DOD = 100% at different C-rates.

The resulting difference in spatial distribution of the ions at varying c-rate is depicted in Zhang et al. paper (Figure 2.7). Its study is extended at lower C-rates (Figure 2.8)

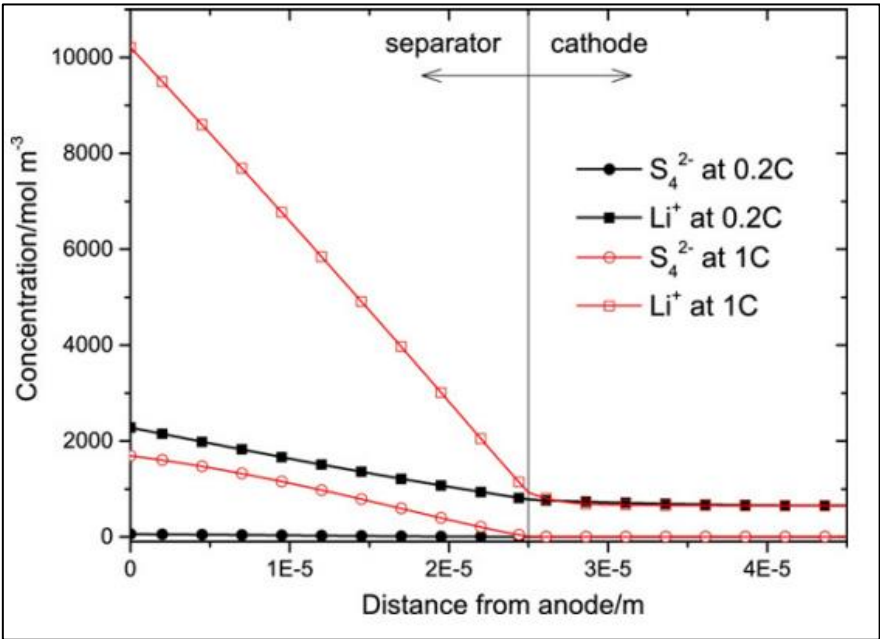


Figure 2. 7 - Species distribution at DOD = 100%, high c-rates [32]

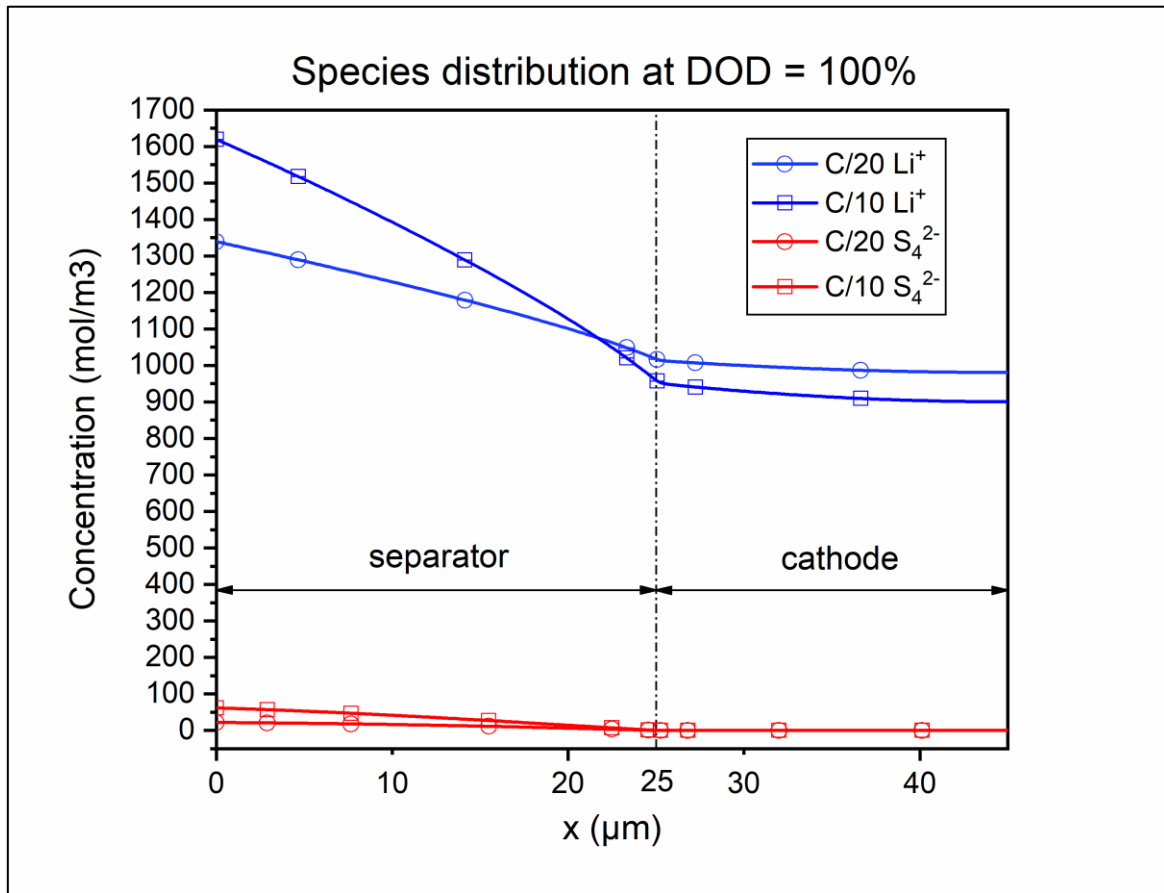


Figure 2. 8 - Species distribution at DOD = 100%, low c-rates

Comparing Figure 2.7 and Figure 2.8, it possible to notice that, at lower C-rates, the discrepancy in  $Li^+$  concentration gradient is far less steep as diffusion limitation to the cell discharge is less impacting, thus a milder reduction in the driving force for PS attraction towards the separator (hindering their further reduction) occurs, resulting in limited discrepancy in discharge capacity.

#### 2.3.2.2.2 Parametric sweep on cell temperature

The behaviour of the model at different temperatures is investigated.

It must be stressed out that the imposed values are homogeneous internal temperatures of the battery, not environmental ones, but an easy correlation between them could be performed in a heat transfer study.

## Discharge Curves at different temperatures

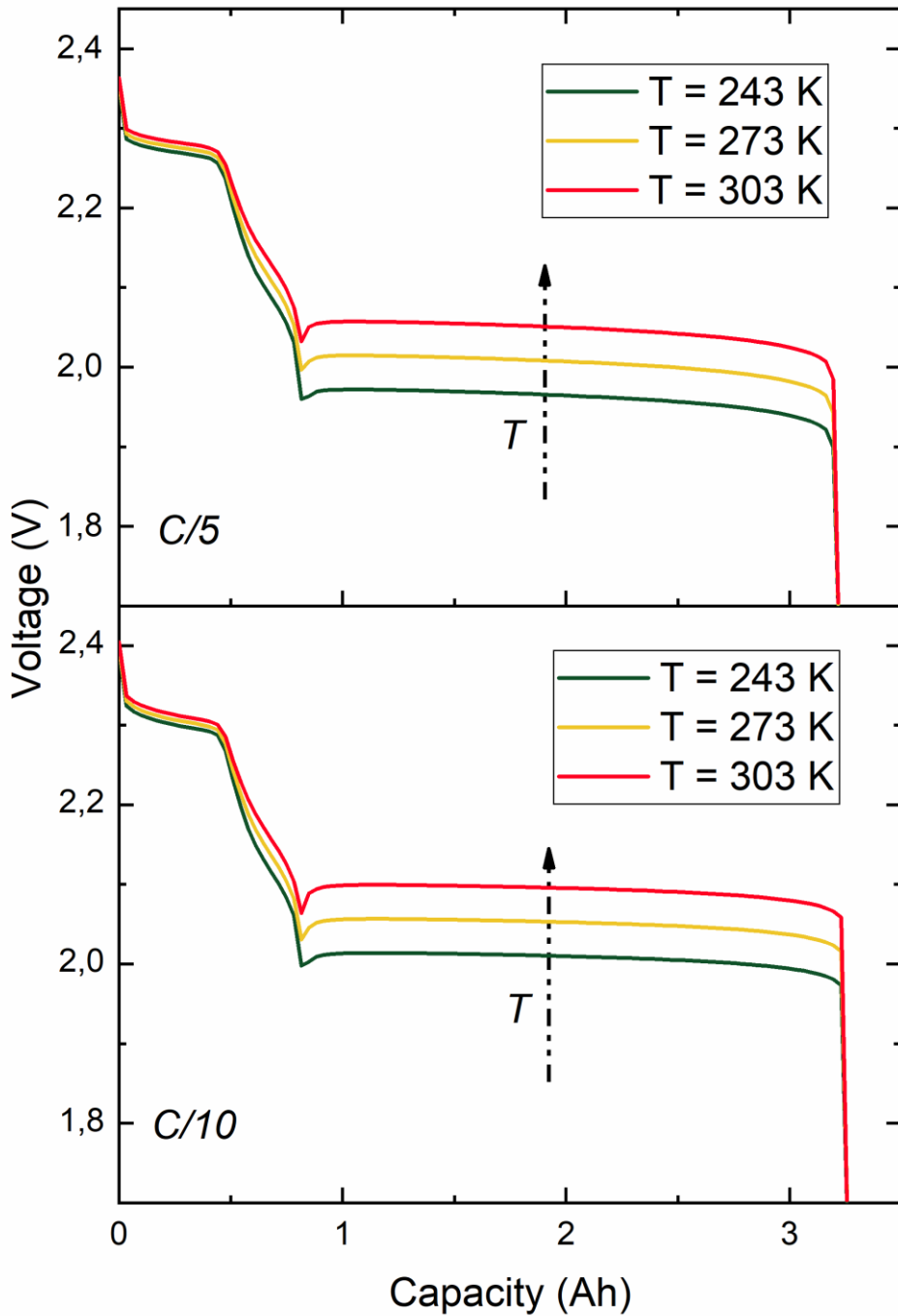


Figure 2.9 – Testing the model temperature sensitivity

In Figure 2.9, the effect of internal temperature variation over C/5 and C/10 discharge is depicted. As the battery gets hotter, the polarization effects reduce, thus both plateaus occur at higher voltages, being the first one slightly affected compared to the second one.

Differently from what experimental evidence suggests [34] no variation in cell capacities occurs.

The supersaturation peak appears more pronounced at high temperature. This effect could be related to a less impacting positive effect on  $\text{Li}_2\text{S}$  precipitation kinetics compared to electrochemical reactions, similarly to the previously provided description.

It is mandatory to point out that Zhang model is not capable to compute the real time temperature distribution of the cell as it lacks of a thermal subset of equation, thus it adopts the initial value as reference constant during the whole discharge.

The set of equation which could be introduced to account for the thermal phenomena are explained.

During the operation of a battery, heat is generated and it can be distinguished in two different contributions:

- 1) Reversible heat is generated by the  $j$ -th reaction occurring in the cell, accounts for the heat of reaction, employing the Faraday's law, and it is defined as:

$$Q_{rev,j} = \left[ \frac{\Delta H_j}{n_j F} - \frac{\Delta G_j}{n_j F} \right] i_j = T \frac{\Delta S_j}{n_j F} i_j = T \frac{\partial E_{eq,j}}{\partial T} i_j \quad (2.33)$$

- 2) Irreversible heat is generated by the activation polarization effect and Joule effect in electrodes and electrolyte as ionic/electronic and ionic only current flow.

Considering the activation polarization heat for the  $j$ -th reaction, it could be expressed by:

$$Q_{P,j} = \eta_{act,j} i_j = (\phi_1 - \phi_2 - E_{eq,j}) i_j \quad (2.34)$$

Joule heating accounts for charge migration dissipation effect, expressed in local form as:

$$Q_{JH} = -(\mathbf{i}_s \cdot \nabla \phi_1 + \mathbf{i}_e \cdot \nabla \phi_2) \quad (2.35)$$

The total electrochemical heat for the  $j$ -th reaction is the sum between the reversible heat and the activation polarization heat:

$$Q_{R,j} = Q_{rev,j} + Q_{P,j} = \left( T \frac{\partial E_{eq,j}}{\partial T} + \phi_1 - \phi_2 - E_{eq,j} \right) i_j \quad (2.36)$$

The total heat source accounting for both reversible and irreversible heating is:

$$Q_{TOT} = Q_{JH} + \sum_j a_v Q_{Rj} \quad (2.37)$$

As LSBs operate at low c-rate, it's fair to consider that the increase in cell internal temperature compared to the environmental one should be negligible due to the abovementioned contributions.

## 3. Experimental validation of the model

In this chapter, the phases of calibration and validation of the model are carried out: the first refers to the selection of the parameters to be adopted, complying with experimental results and literature data, while the second refers the comparison between simulation and experimental results.

### 3.1 Battery assembly and testing

Experimental data are obtained by assembling and testing lithium sulfur coin cells (CR2032) in the Electrochemistry laboratory at Department of Applied Science and Technology (DISAT).

#### 3.1.1 Coin cells assembling

The procedure employed to assemble lithium sulfur coin cells is described in detail starting from the preparation of the active cathodic material.

##### 3.1.1.1 Preparation of the cathodes

###### 3.1.1.1.1 *Preparation of the slurry*

The tape casting method is employed. At first, octasulfur ( $\geq 99.5$  % Sigma Aldrich) is mixed with highly electronically conductive Carbon Black, Ketjenblack® (KjB, EC-300J, AkzoNobel) in a specific weight ratio to overcome the limitation of the insulating nature of the active material.

Both substances are available in form of powders. An initial mixing process, simple and easily reproducible is performed in an agate mortar with a pestle to guarantee a sufficient homogeneity of the blend (Figure 3.1).

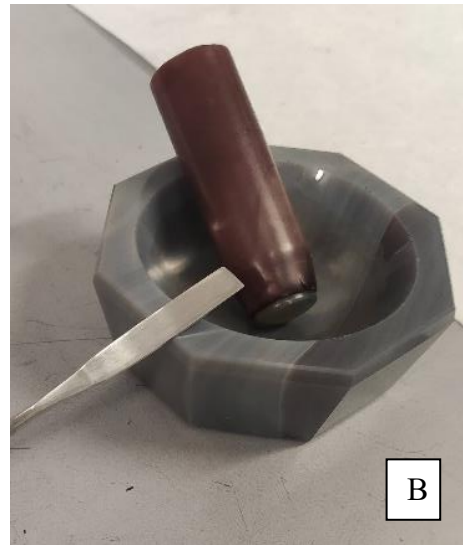
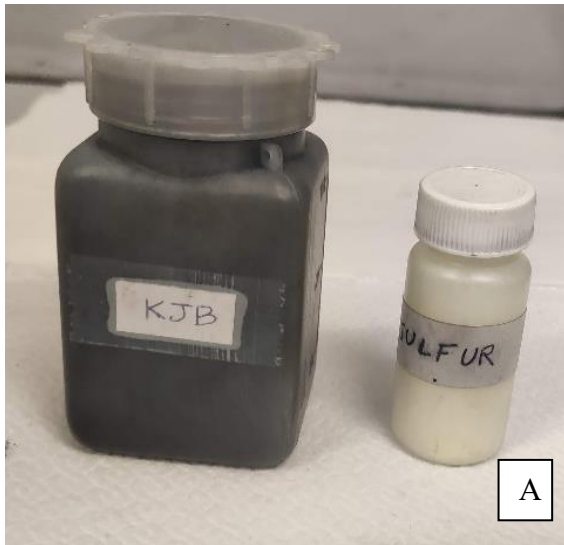


Figure 3. 1 – KJB and octasulfur in powder containers (a), mortar, pestle and spatula to handles powders (b)

A 8% wt. solution of Polyvinylidene fluoride (PVdF) in N-Methyl-2-pyrrolidone (NMP) is employed as a binder.

PVdF is inert and allows to hold the cathodic powdered material structure together and ensure contact with the current collector, while the liquid NMP supports the deposition process.

The solution is extracted by a calibrated micropipette and injected in a test tube, jointly with the powder and two zirconia spheres, to aid the subsequent ball milling process (Figure 3.2)

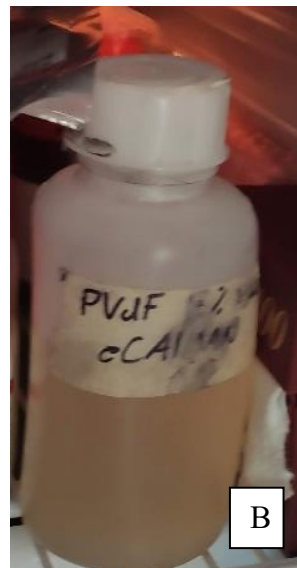
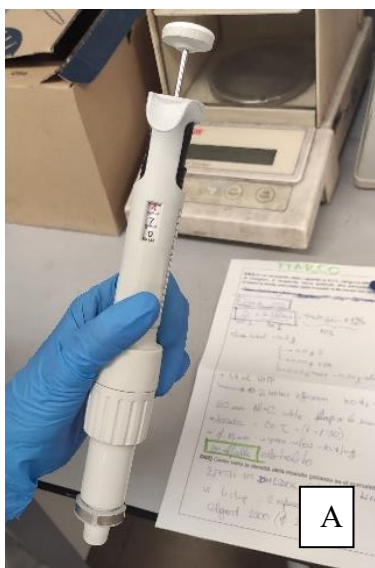


Figure 3. 2 – Micropipette (a), PVdF in NMP solution (b), slurry in the test tube (c)

The mass ratio is  $S_8:KJB:PVdF$  60: 30: 10% (wt) and the calculation on PVdF contribution is carried out considering the concentration of the solute in the solution.

Ball milling is performed to guarantee the homogeneity of powder dispersion, the frequency and milling time chosen are 30 Hz and 15 minutes (Figure 3.3).



Figure 3. 3 - Ball milling machine

### 3.1.1.1.2 Tape casting

The slurry is manually deposited on a 20  $\mu\text{m}$  carbon coated aluminium foil, ready for tape casting. The tape casting process is performed adopting a 200  $\mu\text{m}$  doctor blade thickness, while the speed is set at 50 mm/s on the automatic film applicator (Figure 3.5). The film is then pre-dried in an oven, setting the temperature at 50°C for almost 2 hours.

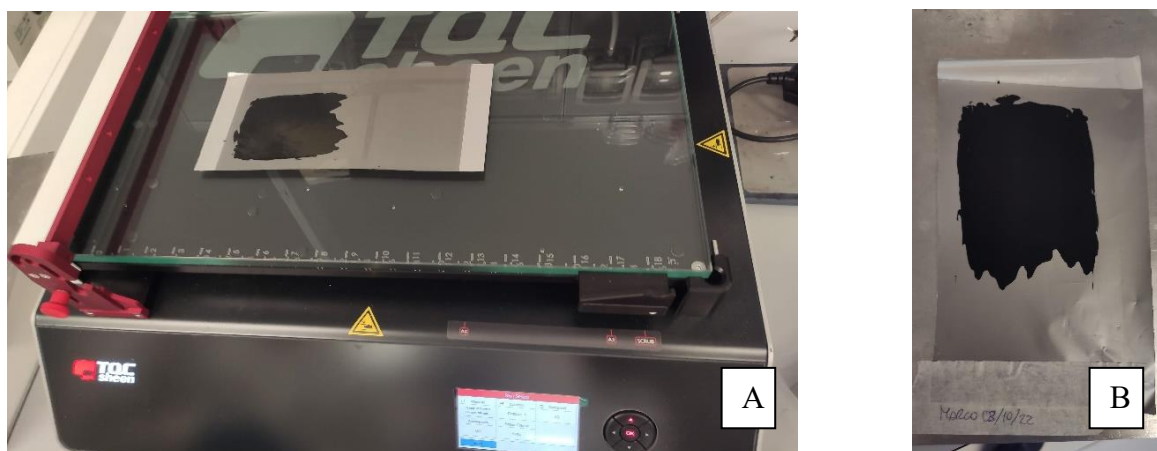


Figure 3. 4 - Tape casting (a) and slurry after drying in the oven (b)

The purpose of this process is to obtain a layer constituted by homogeneously spread components which will be then properly cut to carve out cathodes.

### 3.1.1.1.3 Cutting, weighting and sorting

The as prepared coated foil is ready for the cutting process, being carried out by employing a specific manually operated tool to carve disks of the proper size (15 mm diameter), according to the CR2032 standards.

Out of the first layer, 19 disks are obtained, weighted and sorted to proceed with a proper classification.

The lighter ones (insufficient mass loading) and the heaviest ones are discarded as outliers, 11 disks are preserved and subsequently their thickness measured by a calibrated micrometer.

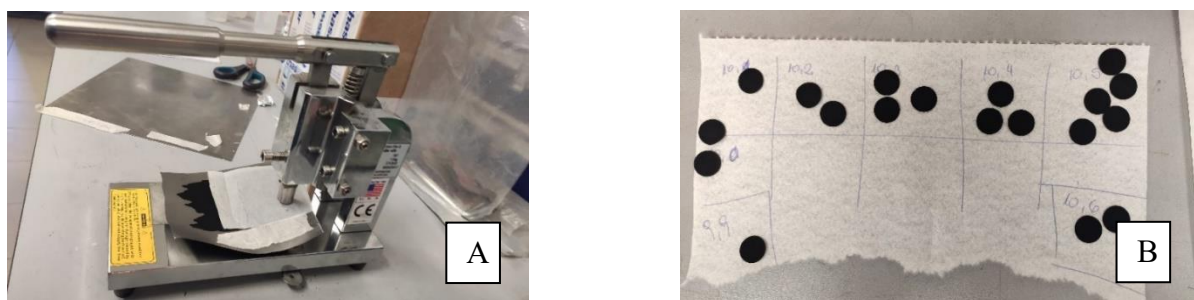


Figure 3. 5 – Cutting tool (a) and weight-based sorting (b)

A vacuum oven is employed to remove remaining air and moisture from the cathodes, adopting a vacuum BUCHI glass oven (Figure 3.6), after properly setting the required time on the control system.

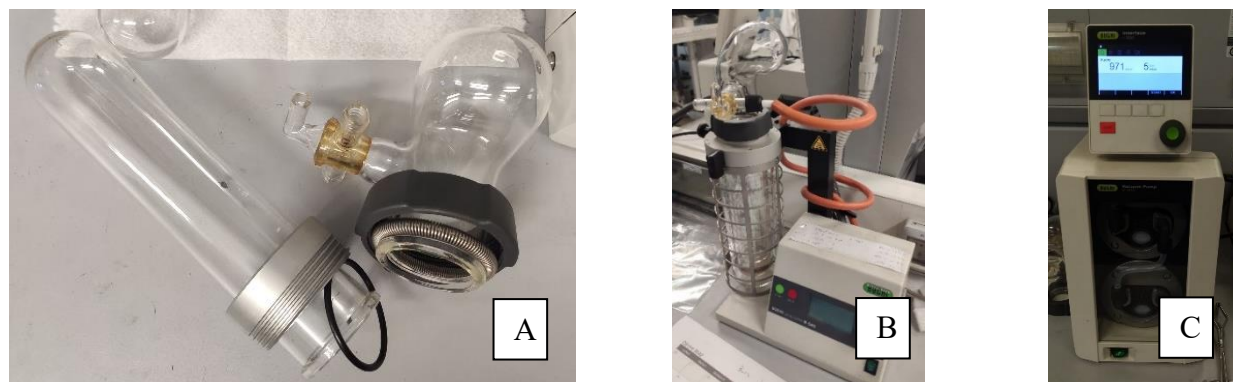


Figure 3. 6 – Vacuum chamber (a), control system (b), vacuum pump (c)

### 3.1.1.2 Preparation of the electrolyte

The following activities are performed in a glovebox, that is a sealed container in an argon atmosphere with adjustable pressure (MBraun Labstar,  $H_2O$  and  $O_2$  content  $< 1$  ppm). The access to the internal environment is allowed by the presence of gloved ports where the user can insert their arms to operate.



*Figure 3. 7 – Glovebox at DISAT Electrochemistry Lab [35]*

The exchange of material between internal and external environment is achieved by an antechamber, where the vacuum, argon filling and door closure are controlled by a valve.

The preparation of the electrolyte is carried out, the solvent adopted is a mixture of 1,2-Dimethoxyethane (DME) and 1,3-Dioxolane (DOL) in 1:1 volume ratio. A micropipette is adopted to transfer both liquids into a flask to determine the correct volume.

1 M Lithium bis(trifluoromethanesulfonyl)imide (LiTFSI) and 0.25 M lithium nitrate ( $LiNO_3$ ) are the lithium salts added as solutes, , and left to solubilize for one night.

An additional quantity of solvent is added to reach the exact volume required, adding a small amount in steps and checking for the concave meniscus position.

### 3.1.1.3 Final cell assembly

The following components are required to assemble the coin cells in the glovebox (Figure 3.8):

- 1) Positive case: in contact with the positive terminal of the electronic device to power;
- 2) Spacers: conductive material disks (0.5 mm thick) required to fill the extra space within the cases;
- 3) Cathode: sulfur-based cathode electrode ( $\varnothing$  15 mm);
- 4) Separator: Celgard 2500, a 25  $\mu$ m Monolayer Microporous Membrane (PP) ( $\varnothing$  20 mm)
- 5) Anode: metallic lithium disk ( $\varnothing$  15 mm);
- 6) Spring: inserted at the anode side to hold the internal structure in slight compression;
- 7) Negative case: in contact with the positive terminal of the electronic device to power;

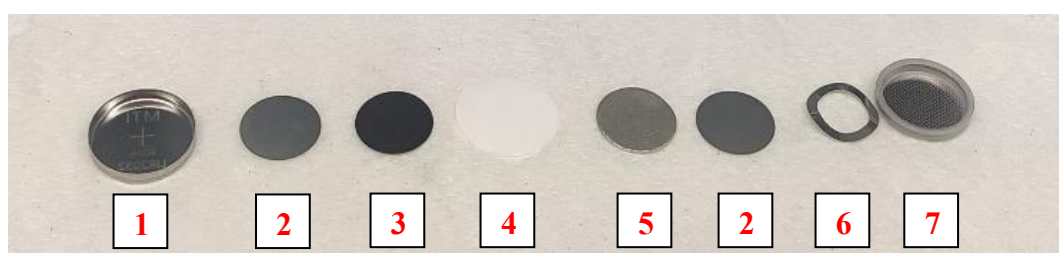


Figure 3. 8 – Coin cell components

Before proceeding to the assembly, the cathode disks are weighted and the  $I_{1C}$  is calculated for subsequent testing purposes as it will be explained in the following chapter.

At first, spring, bottom spacer and lithium disk are inserted in the negative case, then a share of electrolyte (10  $\mu$ l) is deposited on the top of the structure.

The separator is positioned at the top, the remaining electrolyte is deposited (10  $\mu$ l), subsequently the cathode, top spacer and the positive case are placed. A slight compression is performed as a pre-closure of the cell (Figure 3.9).

The cells are brought out of the glovebox, then closed by a manual machine and tested by a voltmeter to be sure of them not being in in short circuit.



*Figure 3. 9 – Pre-closed cells*

### **3.1.2 Battery Testing**

#### **3.1.2.1 Galvanostatic Cycling**

Galvanostatic cycling is a straightforward method in battery testing which allows to obtain relevant information as the shape of charge/discharge curves over battery lifetime and their sensitivity to the adopted C-rate. In Figure 3.10, the Arbin battery cycler employed to perform the GC testing.

The term “galvanostatic” refers to a constant applied current during a single charge/discharge step.

The testing procedure is programmed on a proprietary software adopting a simple user interface:

- 1) The cell is set to rest for 1 hour to measure and stabilize its OCV evolution;
- 2) The lower and upper voltage thresholds are set as 1.8V and 2.6V;
- 3) The number of cycles and the C-rate adopted are selected.

As a common practice for commercial cells, initial conditioning cycles at low C-rate (e.g. C/10) could be performed to promote the formation of a stable SEI.

### 3.1.2.1.1 Galvanostatic Cycling experimental results

Considering a cell tested at DISAT electrochemistry lab (Figure 3.11), the specific capacity is plotted, being the ratio between capacity and the mass of sulfur employed.

An evident drop in discharge capacity between the first two conditioning cycles at C/10 occurs. After the first three cycles at C/10, the cell is subsequently discharge at C/5 for additional 326 cycles, showing a strong capacity fade.



Figure 3. 10 - Arbin battery cycler

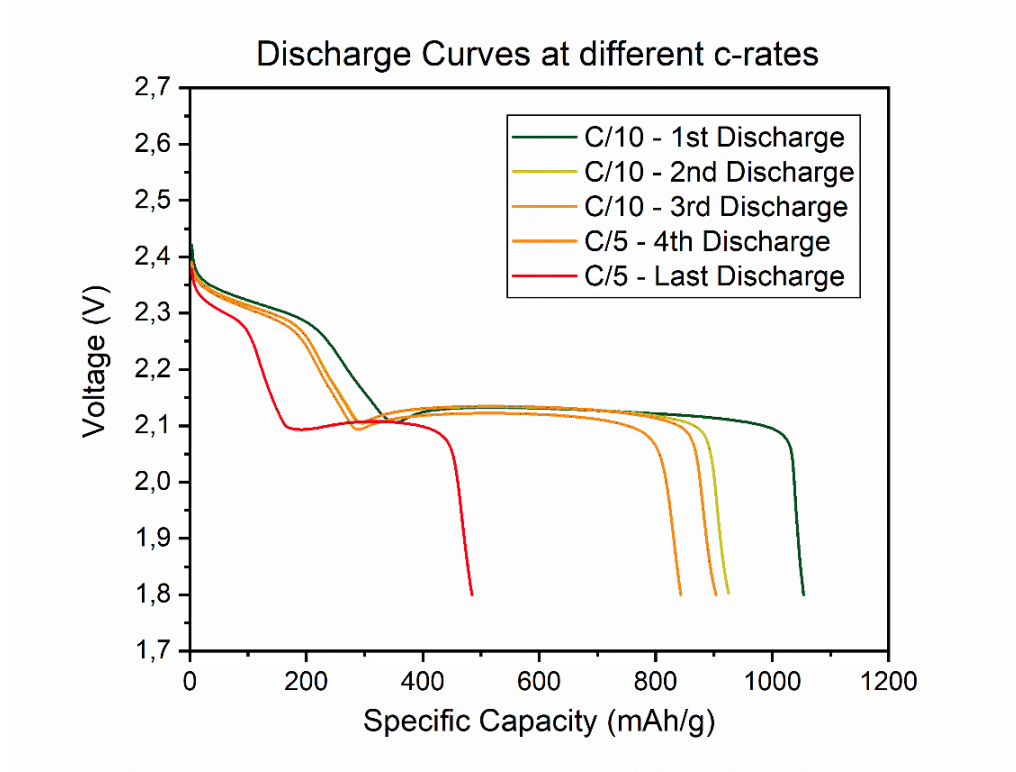


Figure 3. 11 – Discharge behaviour of a coin cell over C/10 formation cycles and subsequent C/5 cycling

The charge/discharge capacity could be easily computed by multiplying the charge/discharge time by the applied current, allowing to calculate the coulombic efficiency. The evolution of these parameters is an indicator of the battery capacity fading (Figure 3.12).

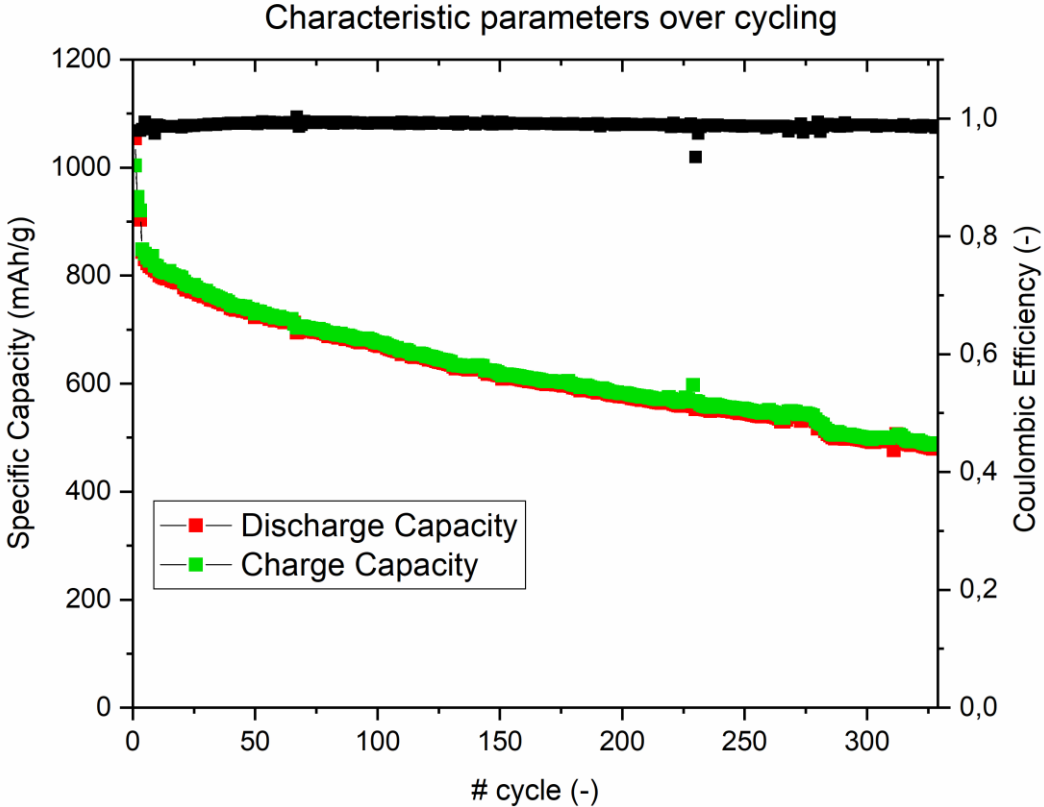


Figure 3. 12 – Cycling behaviour in terms of capacity fade and coulombic efficiency fluctuations

The availability of dozens of assembled cells allowed to perform several GC tests at different C-rates, most of the data resulted to be outliers, presenting critical deviations compared to the commonly accepted shapes for LSBs, thus only two of them are considered to be worthy of being shown and adopted in the validation process (Figure 3.13).

The choice to adopt only discharge curves from the first cycles for the validation process is rooted on the limitation of the model, which is incapable to simulate the phenomenon of SEI formation and its impact on battery performance.

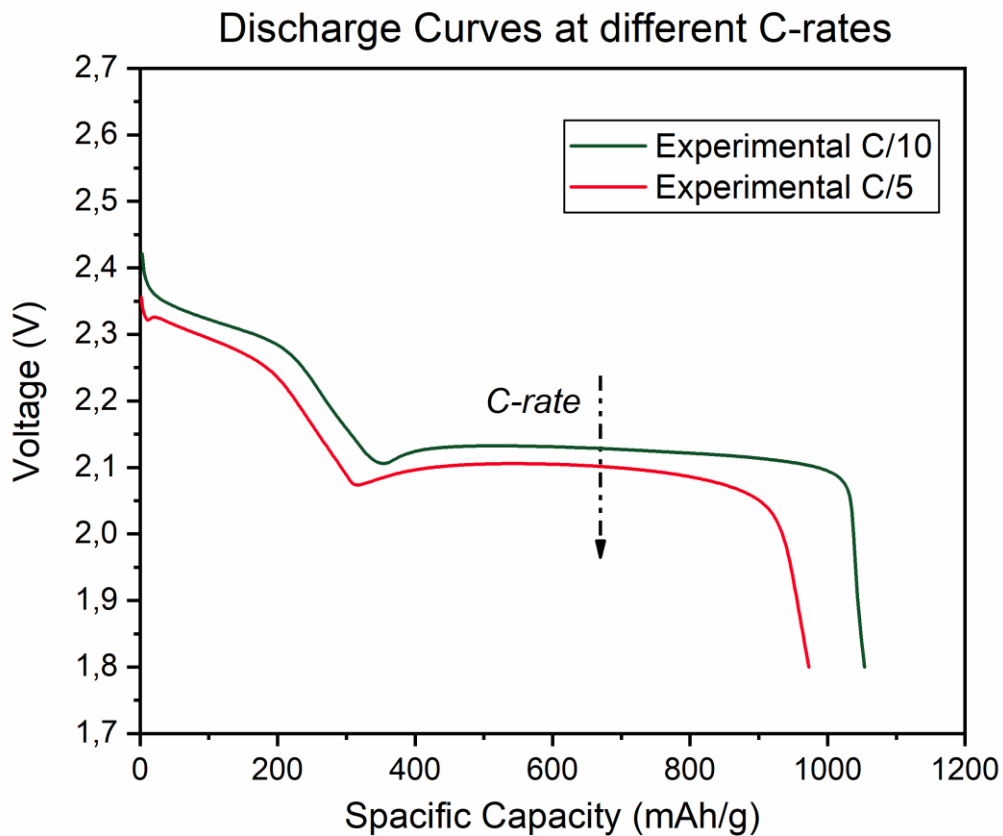


Figure 3. 13 – C/10 and C/5 discharge curves employed for model validation

### 3.1.2.2 Electrochemical Impedance Spectroscopy

EIS allows to investigate bulk and surface properties of an electrochemical device by an in-situ non-destructive analysis. The study is black box based, an alternating current/voltage at different frequency is imposed to the system and its corresponding impedance is calculated by mean of power electronics.

In a potentiostatic study, a voltage signal is applied and current is measured, while in a galvanostatic study a current signal is applied and voltage is measured.

The potentiostatic approach is the most common, an electrochemical interface applies a constant voltage while a frequency response analyzer (FRA) superimposes an AC voltage (around 10 mV) with a frequency from mHz to MHz.

The result is a waveform with a not null mean value. The amplitude is small enough to detect a pseudo-linear response but not excessively to avoid noise disturbance that can compromise the reading of the output signal.

The system must be at rest before the test (OCV conditions) to ensure a slight variation of the cell voltage over the process.

As the measuring circuit closes, a change in electrode potential occurs and an electric double layer develops, chemical species reduce/oxidize and diffusion occurs.

Applying AC excitation at different frequency allows to study separately these events as they are characterized by different time constants.

An equivalent circuit is adopted to represent the different components of the cell impedance, comprising resistances, capacitances and constant phase elements (CPE) that represent the non-idealities in the circuit.

The battery performances could be tested to detect their degradation upon cycling.

The main goal is to measure these parameters and relate them to specific physical phenomena occurring.

The impedance is represented on a Nyquist plot, with real part ( $Re(\mathbf{Z})$  or  $Z'$ ) on x-axis and the negative imaginary part ( $-Im(\mathbf{Z})$  or  $Z''$ ) on the y-axis. It is also possible to represent the data on a Bode plot, with frequency on x-axis and magnitude or phase angle on the y-axis.

In the equivalent circuit, resistors model electrolyte resistance and faradaic currents, capacitors model charge separation, double layer and grain boundaries effects.

The constant phase element is composed by a variable resistance and a variable capacitor, it describes non uniform properties in a system according to the following formula:

$$Z = \frac{1}{(j\omega)^n Y_0} \quad (3.1)$$

Where  $Y_0$  is a constant,  $n = 0 \div 1$  is responsible for the semi-circle depression. With  $n = 0.5$  the CPE is referred to a Warburg impedance, that is adopted to model diffusion, characterized by equal negative imaginary part and real parts on the Nyquist plot.

Phenomena that occur in the same spatial location are modelled by circuit elements in parallel, while physically sequential phenomena are modelled by series parameters.

For a simple resistive model (e.g. representing electrolytic resistance), Ohm’s law is valid and the impedance would be represented on the Nyquist plot by a point on the real axis, while on Bode plot by a constant value of magnitude and phase angle.

A more realistic model would include a capacitor that considers the effect of the EDL and a resistor that models faradaic current. These two elements are connected in parallel, considering the equivalent impedance:

$$Z = \frac{R_F}{1 + j\omega C_{DL}R_F} \tag{3.2}$$

At high frequency, the impedance will tend to zero, while at low frequency it will tend to  $R_F$ , thus its Nyquist plot representation would be a semi-circle.

With a more complex model, more elements are included, so Nyquist plot could be like in Figure 3.14.

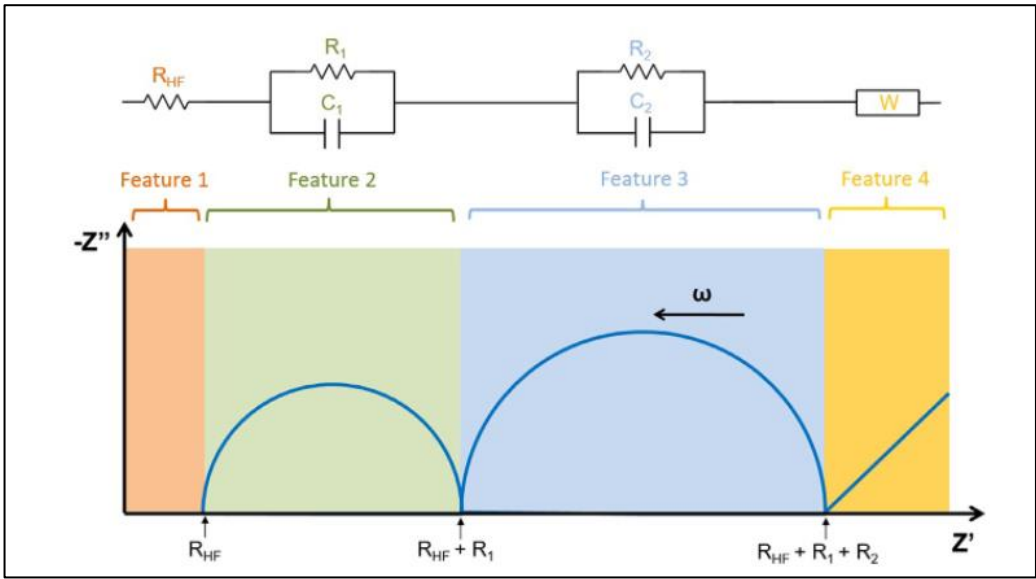


Figure 3. 14 - Nyquist plot from EIS performed on a generic battery [37]

In the proposed case (Figure 3.14) a metal-ion battery is considered, by decreasing in frequency of the applied waveform: the first feature is represented by  $R_{HF}$ , the second and third ones by  $R_1C_1$  and  $R_2C_2$  parallel, while the fourth one by a Warburg element [37].

The specific relationships between the operational behaviour and characteristic parameters are described for the peculiar case of LSBs [26].

- 1)  $R_{el}$  is the contribution of the electrolyte resistance, influenced by PS dissolution and also including the effect of electrical connection;
- 2)  $R_S$  and  $CPE_S$  are related to the surface resistance of both electrodes and to the electrical double layer capacitive effect;
- 3)  $R_{ct}$  and  $CPE_{ct}$  are related to the charge transfer resistance and pore double layer capacity;
- 4)  $W$  is the Warburg Impedance related to PS diffusion effect within the cathode;

### 3.1.2.2.1 EIS experimental results

Three cells have been assembled and immediately tested by PEIS to evaluate their behaviour and compare it to available data from literature (Figure 3.15).

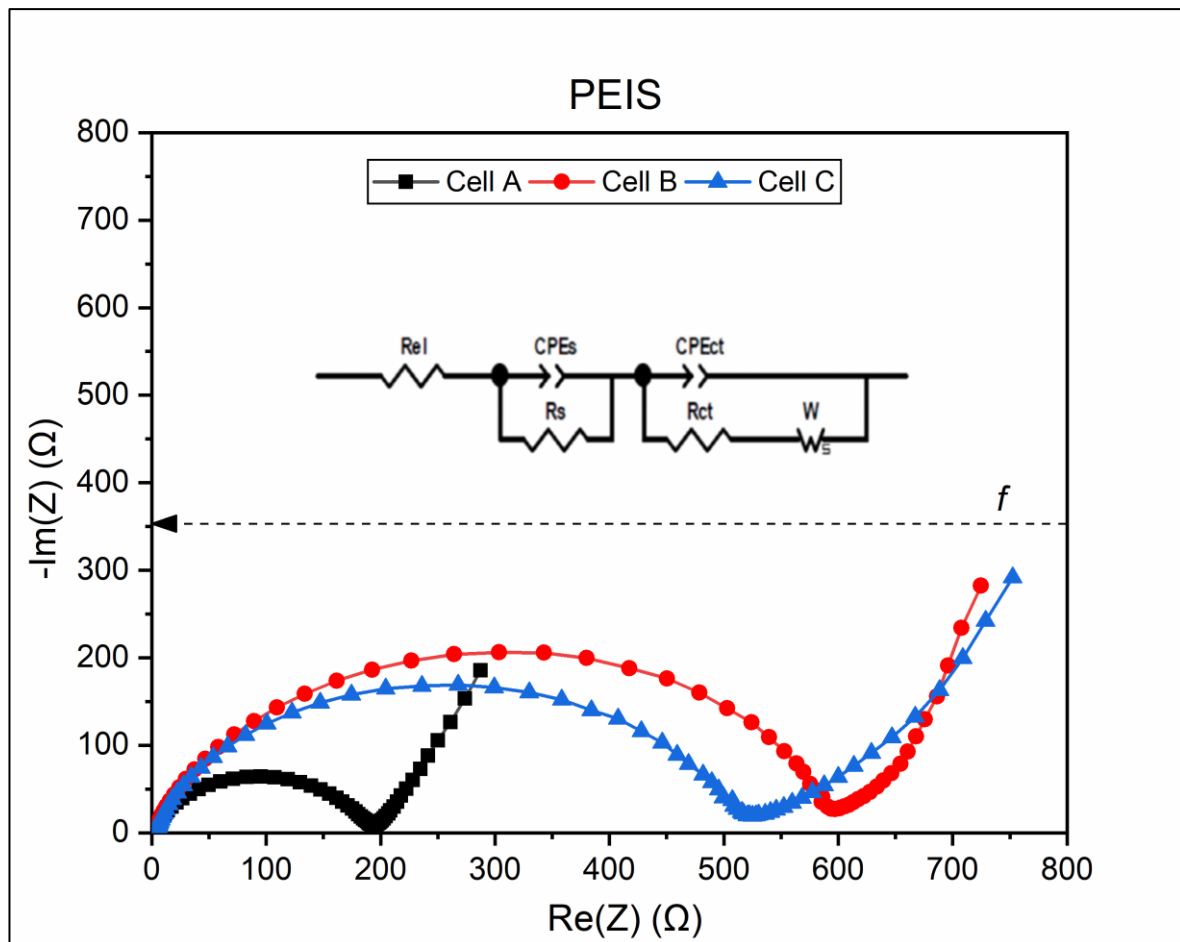


Figure 3. 15 – Nyquist plot of 3 lithium-sulfur coin cells

The spectra are all constituted by a depressed semicircle and by a bended pseudolinear response. The semicircle is the result of a superposition of many semicircles, each one related to a parallel contribution, and it is positioned in medium/high frequency range of each curve,. The first value of  $Re(\mathbf{Z})$  for each spectrum corresponds to  $R_{el}$ , while the  $Re(\mathbf{Z})$  values related to the depressed semi-circles closure corresponds to  $R_{ct}$ .

*Table 3. 1 - PEIS paramaters and results*

	<b>Cell A</b>	<b>Cell B</b>	<b>Cell C</b>
$R_{el} (\Omega)$	2.64	3.47	3.97
$f_{R_{el}}(Hz)$	5E5		
$R_{ct} (\Omega)$	193	597	525
$f_{R_{ct}}(Hz)$	8.53	4.23	4.23

In Table 3.1 the electrolyte resistance of Cell A is in accordance with literature results [26], while slightly higher for the two other cells.

The charge transfer resistance appears extremely high for the three cases, because it is two orders of magnitude higher than expected ones [26].

The main reason beyond the discrepancies could be due to an EIS not performed at OCV, neither with priorly formation cycles occurrence, differently from the test performed on the cells from literature [26].

### 3.1.2.3 Voltammetry

Voltammetry is a technique adopted to extract information about electrochemical processes.

The oxidation and reduction processes are studied by analysing the voltammogram plots, relating the current produced and the potential of the working electrode in the form  $I=f(E)$ .

Employing different scan rates will result in a different system response, thus the shape of the curves is affected.

### 3.1.2.3.1 Cyclic Voltammetry for reversible processes

Potential is swept up and down at constant scan rate  $\nu$ , at time  $\lambda$  potential reversal is set.

As the cathodic scan begins, only capacitive currents flow up to the voltage approaching the reduction potential, thus reduction takes place consuming oxidized species and the current increases up to the cathodic peak current  $i_{p,c}$  corresponding to the cathodic peak potential  $E_{p,c}$ .

The concentration gradient progressively increases as the potential decreases and current rises. After the peak, the electrode surface is saturated thus the process becomes diffusion limited (depletion effect). As the voltage is reversed, the anodic scan is performed and the oxidation rate is maximized at the anodic peak current  $i_{p,a}$  that corresponds to the anodic peak potential  $E_{p,a}$  (Figure 3.16).

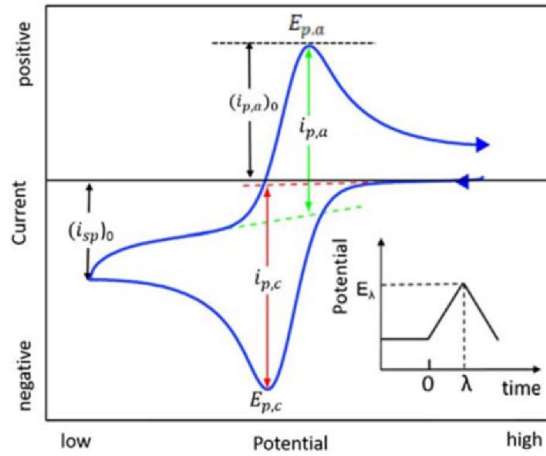


Figure 3. 16 – Cyclic Voltammetry for a reversible process [39]

Considering an electrochemical reversible process, the Randles-Sevick equation states that:

$$i_p = 0.4463nFAC \left( \frac{nF\nu D}{RT} \right)^{\frac{1}{2}} \quad (3.4)$$

where  $n$  is the number of electrons involved in the reaction,  $A$  the surface area of the electrode,  $C$  the oxidized species bulk concentration and  $D$  the diffusion coefficient of the oxidized species.

For an irreversible process:

$$i_p = 2.99 * 10e^5 n(\alpha n_a)^{\frac{3}{2}} AD^{\frac{1}{2}} C \nu^{1/2} \quad (3.5)$$

Two fundamental parameters are peak potential separation ( $\Delta E_p = E_{p,a} - E_{p,c}$ ) and peak current derivation  $i_{p,a}/i_{p,c}$ .

### 3.1.2.3.2 Cyclic Voltammetry for asymmetric processes

The voltammogram could show significantly different relationships between the potential applied and current with the absence of the cathodic peak and/or with multiple oxidation peaks.

In the first case, the cause could be that the oxidation process is irreversible, the products are uncharged or the reduction kinetics is too slow (low  $i_{0,red}$ ) compared to the sweep rate to be identified.

In the second case, the cause is due to multiple species being oxidized at different potentials, that is exactly what occurs in CV testing of lithium-sulfur batteries.

### 3.1.2.3.3 Cyclic Voltammetry experimental results

Cyclic voltammetry is performed at different scan rate, with a rest time of 1 hour between each test, resulting in the graph represented in Figure 3.17.

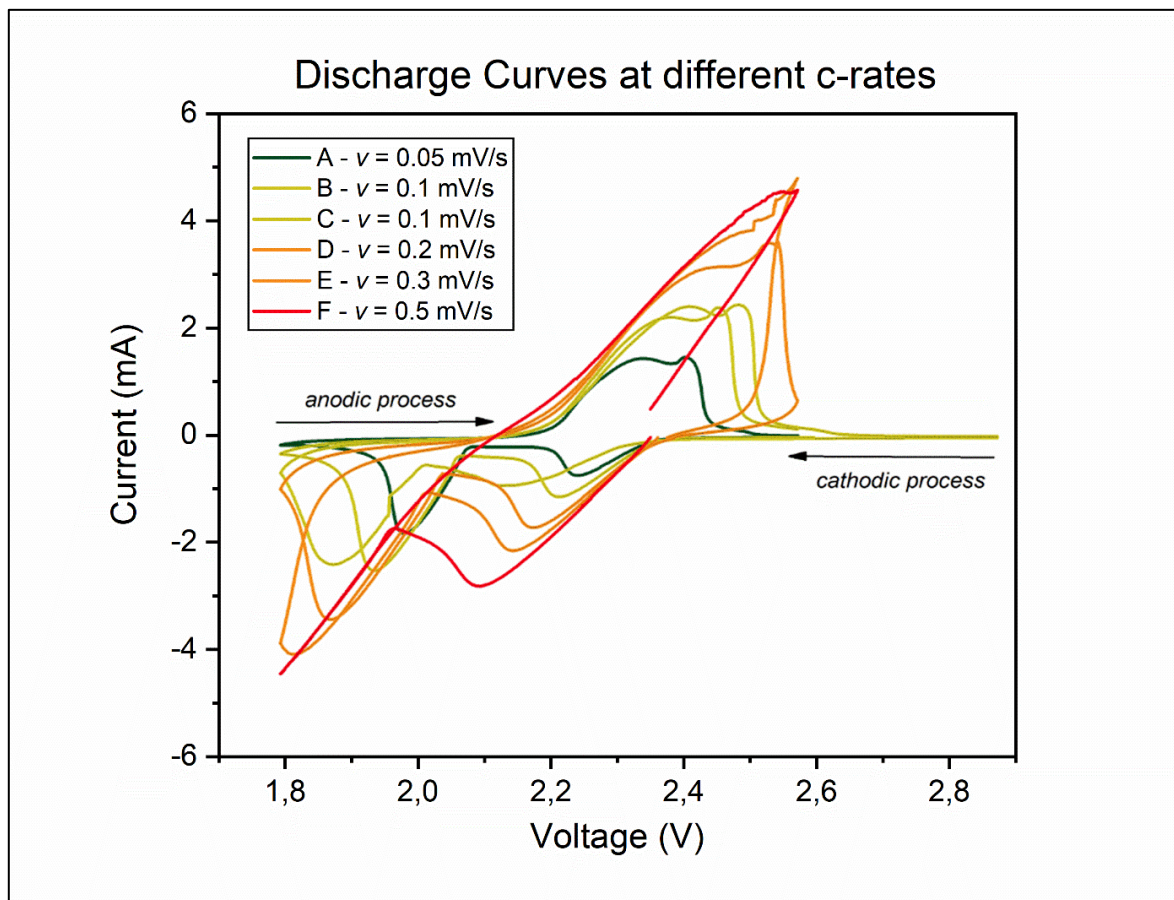


Figure 3. 17 – CV at different scan rates

The anodic process corresponds to the oxidation while the cathodic process to the reduction; the main current peaks could be related to the plateaux of the galvanostatic cycling and to their characteristic reactions.

By increasing the scan rate, the polarization effect is more pronounced as the cathodic peaks are situated at lower voltage, while the anodic peaks are situated at higher voltage.

At high scan rate the current peaks increase in magnitude and get closer in both anodic and cathodic scan. Over  $v = 0.2$  mV/s the anodic peaks overlap, thus it's not possible to distinguish the current contributions of the sets of reactions related to the two plateaux.

In this thesis the purpose of CV applied to LSBs is the detection of  $Li^+$  effective diffusion coefficients adopting the equation 3.4 [39].

Table 3. 2 - Determination of  $D_{Li^+}^{eff}$  from CV data fitting

	$v$ (mV/s)	$i_p$ (mA)	$D_{Li^+}$ ( $m^2/s$ )		$v$ (mV/s)	$i_p$ (mA)	$D_{Li^+}$ ( $m^2/s$ )
A	0.1	2.3	9.27468E-13	D	0.2	3.5	2.41E-12
	0.1	2.4	1.008E-12		0.2	3	7.89E-13
	0.1	2.5	1.09906E-12		0.2	2	3.51E-13
	0.1	1	1.7417E-13		0.2	3.2	8.98E-13
B	0.05	1.5	7.89675E-13	E	0.3	4	2.10E-12
	0.05	1.4	6.8789E-13		0.3	4	2.10E-12
	0.05	0.75	1.97418E-13		0.3	2	2.34E-13
	0.05	2.75	2.65418E-12		0.3	4	2.10E-12
C	0.1	2.3	9.27606E-13	F	0.5	4.5	1.59426E-12
	0.1	2.2	8.49E-13		0.5	4.5	1.59426E-12
	0.1	1.3	2.96E-13				
	0.1	2.5	1.10E-12				

The sets of data from Table 3.2, obtained from Randles-Sevick equation fitting at different scan rates for both anodic and cathodic peak currents, provides an approximate result of  $D_{Li^+}^{eff} \approx 10^{-13} \div 10^{-12} m^2/s$ , where the effect of porosity would lead to a higher values for the bulk diffusion coefficient.

### 3.1.2.4 Galvanostatic Intermittent Titration Technique

The Galvanostatic Intermittent Titration Technique (GITT) is a methodology based on the application of current pulses to an electrochemical device, punctuated by relaxation periods, up to the battery full charge or discharge.

By studying the response of the system, it is possible to characterize both its kinetics and thermodynamics features.

The purpose of the GITT applied to LSB is to estimate the diffusion coefficient of sulfur species dissolved in the electrolyte at different stages of the discharge, with the purpose to determine an average  $D$  for long, intermediate and short chain PS.

The theory behind GITT operation is summarized. The application of a current pulse ( $I_0$ ) to the system of cross-sectional area ( $A$ ) at rest generates a concentration ( $c$ ) imbalance on the oxidized ( $O$ ) and reduced ( $R$ ) species:

$$\frac{I_0}{A} = -nFD_O \left( \frac{\partial c_O}{\partial x} \right)_{x=0} = nFD_R \left( \frac{\partial c_R}{\partial x} \right)_{x=0} \quad (3.6)$$

Where  $D_x$  are the diffusion coefficients.

The surface concentrations of both oxidized and reduced species, being  $L$  the electrolyte thickness, change in time from the *initial* conditions as:

$$\Delta c_{PULSE} = c_{O/R}^{x=0} - c_{O/R}^{initial} = \mp \frac{2I_0\sqrt{t}}{AnF\sqrt{D_{O/R}\pi}} \left( t \ll \frac{L^2}{D} \right) \quad (3.7)$$

Where the validity of the formula holds if the duration of the current pulse is limited by the expression in parenthesis.

According to the Nernst equation, the cell potential will vary accordingly. When the change in surface concentration is small, the potential response ( $\Delta E_{PULSE}$ ) could be approximated as linearly dependent:

$$\Delta E_{PULSE} = k\Delta c_{PULSE} \quad (3.8)$$

Where the constant  $k$  could be derived by the ratio between the change in potential ( $\Delta E_{REL}$ ) and change in concentration ( $\Delta c_{REL}$ ) during the following relaxation step:

$$\Delta E_{REL} = k\Delta C_{REL} \quad (3.9)$$

$$\Delta C_{REL} = \frac{\tau I_0}{nFV_{el}} \quad (3.10)$$

Where  $\tau$  is the duration of the pulse and  $V_{el}$  is the volume of the electrolyte.

By combining the previous equations, the expressions to calculate the diffusion coefficients are:

$$D = \left(\frac{4}{\tau\pi}\right) \left(\frac{V_{el}}{A}\right)^2 \left(\frac{\Delta E_{REL}}{\Delta E_{PULSE}^{t=\tau}}\right)^2 \quad (3.11)$$

Eq. 3.11 allows the evaluation of the diffusion coefficient from the slope of the plot  $\Delta E_{PULSE} \propto \sqrt{t}$  at any given time if linearity holds [40]. In Figure 3.18, the results from GITT at C/20 on a coin cell is shown.

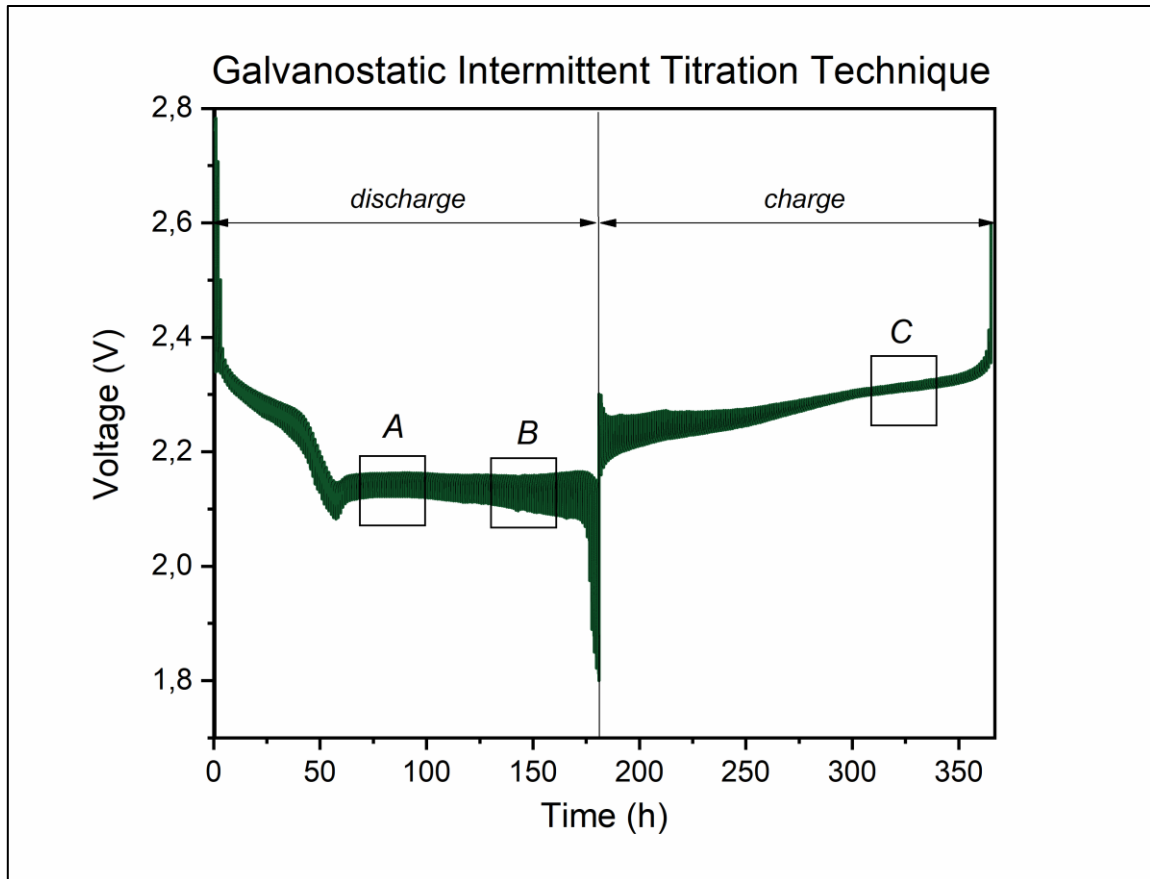


Figure 3. 18 – GITT performed on a lithium sulfur coin cell, charge and discharge set at C/20

The calculations on region A are employed to determine intermediate chain PS diffusion coefficients, while regions B and C are adopted for short and intermediate chain PS respectively.

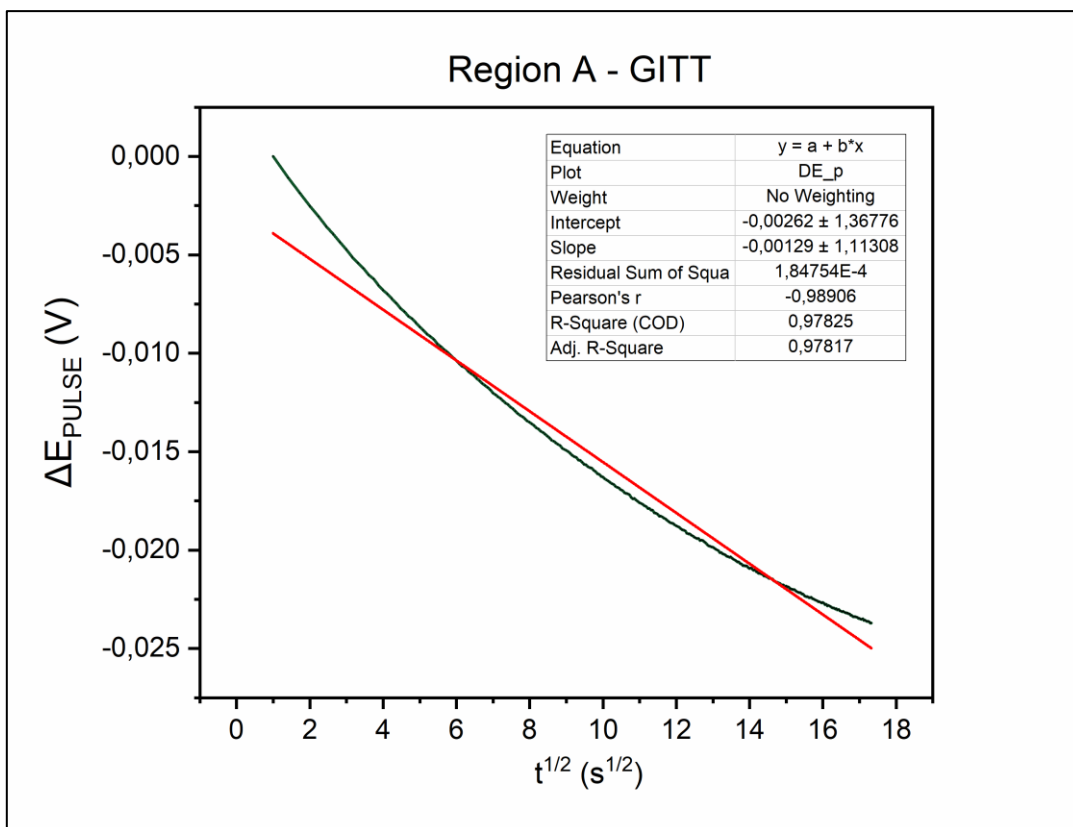


Figure 3. 20 - Evaluation of  $\Delta E_{PULSE}$  vs  $\sqrt{t}$  linearity in region A

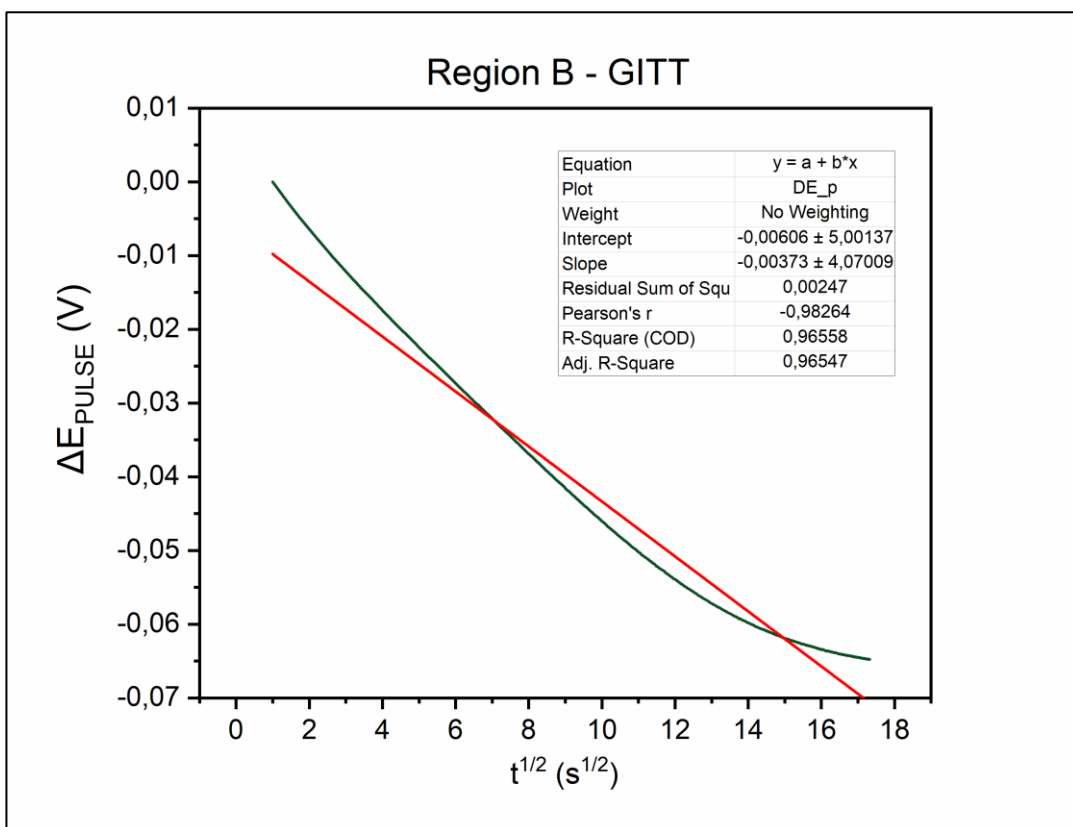


Figure 3. 19 - Evaluation of  $\Delta E_{PULSE}$  vs  $\sqrt{t}$  linearity in region B

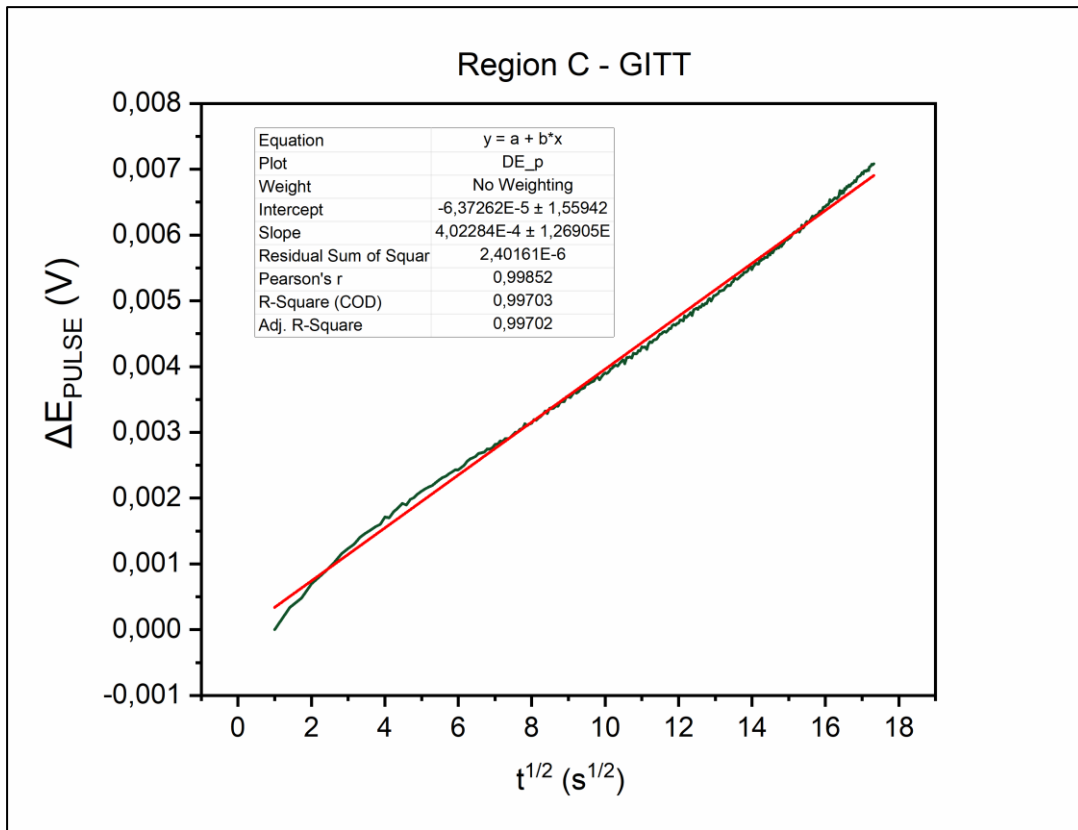


Figure 3. 21 - Evaluation of  $\Delta E_{PULSE}$  vs  $\sqrt{t}$  linearity in region C

Three regions of the GITT curve have been selected to carry out the evaluation of effective diffusion coefficients, applying Equation 3.11:

- 1) Region A is chosen as representative for intermediate chain PS;
- 2) Region B is chosen as representative for short chain PS;
- 3) Region C is chosen as representative for long chain PS.

The previously mentioned condition of linearity is checked (from Figure 3.19 to Figure 3.21), providing satisfactory results especially in Region C.

The resulting effective diffusion coefficients are evaluated (Table 3.3).

Table 3. 3 - Diffusion coefficients from GITT

Region A		Region B		Region C	
$D_{int}^{eff}$	$5.8E-11 \text{ m}^2/\text{s}$	$D_{short}^{eff}$	$6.8E-13 \text{ m}^2/\text{s}$	$D_{long}^{eff}$	$4.8E-14 \text{ m}^2/\text{s}$

The corresponding bulk diffusion coefficients are expected to show orders of magnitude higher values due to the impact of porosity, as expressed by the Bruggeman equation.

## 3.2 Precalibration and validation of the model

### 3.2.1 Precalibration of the model and sensitivity analysis

In the precalibration stage, experimentally measured characteristics of the cell and applied currents are imposed in the parameter list without modifications in physicochemical variables, to understand whether the accuracy of the model is already satisfactory or not (Table 3.4).

The thickness of the cathode is obtained subtracting the thickness of the aluminium current collector from the total thickness of the cathode ( $L_{tot\_pos}$ ), using a micrometer.,

A similar procedure is carried out to evaluate the mass of active material ( $S8\_mass$ ) knowing the total mass of the cathode ( $Pos\_mass$ ) and subtracting the masses of current collector ( $Al\_mass$ ), KJB and binder.

The theoretical  $I_{1C}$  could be calculated from the mass of available octasulfur.

The reference concentration of  $Li^+$  and  $A^-$  is modified to account for the presence of the total 1.25 mol of salt dissolved in the electrolyte (last two rows of Table 3.4).

Table 3. 4 – Modification to model parameters in the precalibration stage

	Zhang preset	Experimental
$L_{sep}$	25 $\mu m$	25 $\mu m$
$L_{tot\_pos}$	-	70 $\mu m$
$L_{Al}$	-	17 $\mu m$
$L_{pos}$	20 $\mu m$	53 $\mu m$
$r_{cell}$	-	7.5 mm
$A_{cell}$	0.28 m <sup>2</sup>	1.767E-4 m <sup>2</sup>
$Pos\_mass$	-	10.5 mg
$Al\_mass$	-	7.76 mg
$S8\_mass$	-	1.65 mg
$Cap_{th}$	3.4 Ah	2.75 mAh
$I_{1C}$	12.143 A	2.75 mA
$c_{Li\_1p\_ref}$	1001 mol/m <sup>3</sup>	1251 mol/m <sup>3</sup>
$C_{A\_1m\_ref}$	1000 mol/m <sup>3</sup>	1250 mol/m <sup>3</sup>

### 3.2.1.1 Comparison between experimental and simulated discharge curves

A comparison between the experimental and simulated curve after precalibration is performed and its results are shown in Figure 3.22.

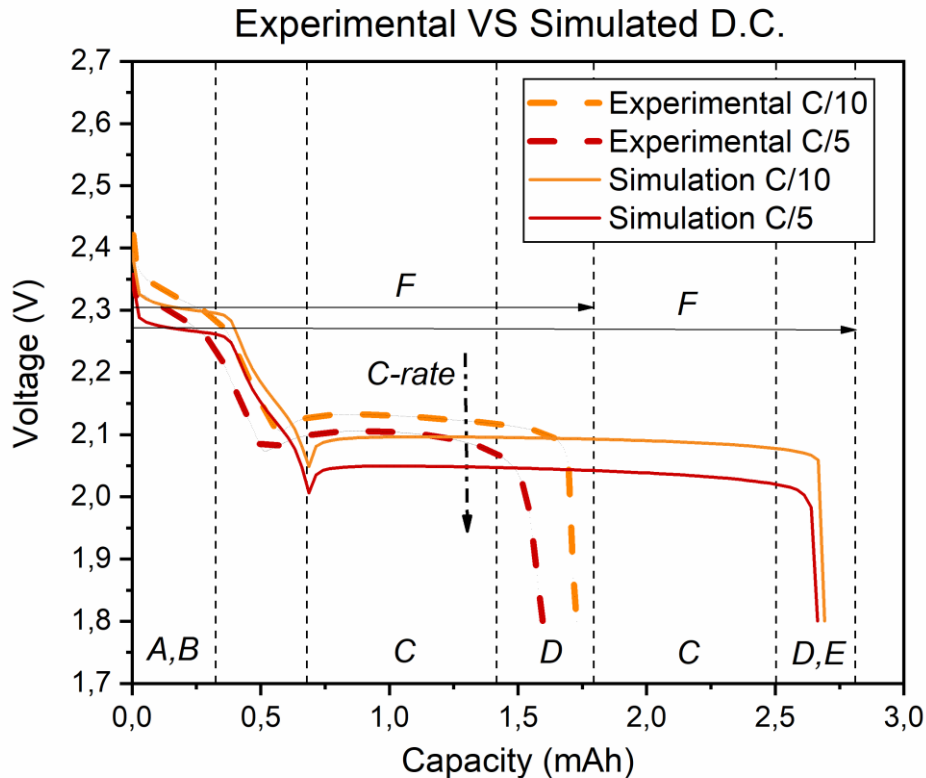


Figure 3. 22 - Comparison between experimental and simulated discharge curves (precalibration)

Noticeable discrepancies appear by observing experimental and simulated discharge curves: a rational analysis would require the identification of peculiar characteristics of their shape and their comparison.

The main differences displayed in the simulated curves are discussed:

- A) In the initial stage of discharge, a much steeper decay is present;
- B) The first plateau occurs at a lower voltage and with a higher capacity Q1;
- C) The second plateau occurs at a lower voltage and with a much higher capacity Q2;
- D) In the last stage of the discharge, the ending part of the curves is much steeper;
- E) Capacity loss at higher C-rate is almost not detectable in the considered range;
- F) From (B) and (C), the overall discharge capacity is significantly higher;

### 3.2.1.2 Sensitivity analysis on diffusion coefficients

Zhang choice on diffusion coefficients appears to be ineffective at the selected C-rates, a parametric analysis is performed, adopting a multiplying coefficient  $MD$  defined such that:

$$D'_i = MD * D_i \quad (3.13)$$

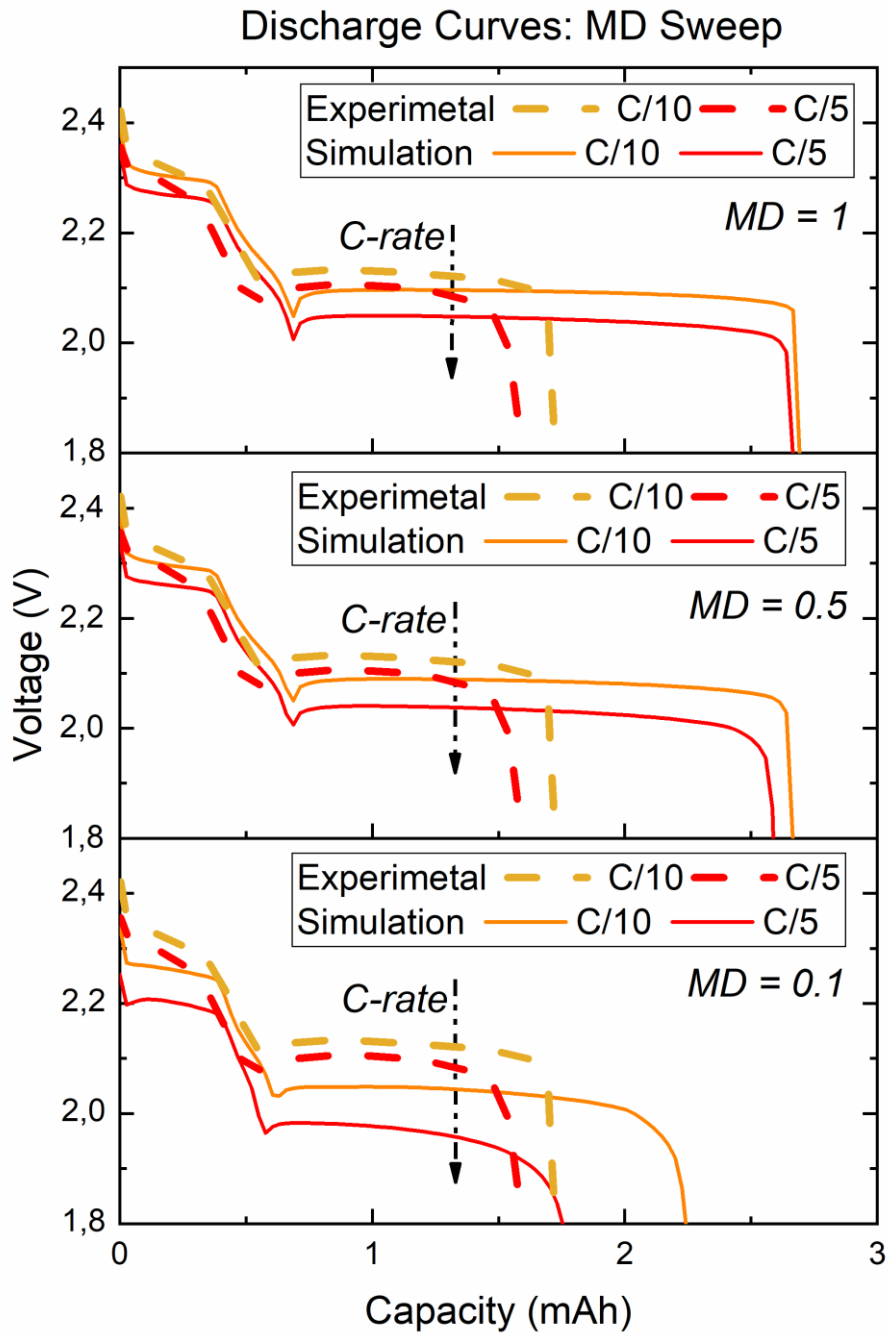


Figure 3. 23 – Parametric sweep on  $MD$

From Figure 3.23, noticeable discharge capacity sensitivity of the model occurs at MD = 0.5, where the discrepancy between C/10 and C/5 is comparable with experimental data. Instead, the effect is excessive at MD = 0.1, corresponding to diffusion coefficients that are one order of magnitude lower than Zhang values.

In MD = 1 and MD = 0.5 cases the values of simulated Q2 stick to almost double the empirical ones, both plateaux occur at the same voltage in both cases, the first slightly lower and the second much lower than experimental values.

Considering the case MD = 0.1, the polarization effect is extreme, causing both plateaux to occur at excessively lower voltage, strongly deviating from experimental data.

The proposed parametric analysis hasn't led to an immediate improvement in the accuracy of the model to predict experimental results.

### 3.2.1.3 Sensitivity analysis on reference exchange current densities

The exchange current densities are key parameters in determining the performance of the LSBs due to their primary impact on electrochemical kinetics., So a parametric sweep is performed by adopting two multiplying coefficients MI1 and MI2, such that:

$$i'_{0,j,1st} = MI1 * i_{0,j,1st} \quad (3.14)$$

$$i'_{0,j,2nd} = MI2 * i_{0,j,2nd} \quad (3.15)$$

Where the first one impacts on the reduction reactions mostly affecting the characteristics of the discharge curve first plateau and the second one would analogously impact most the shape of the second plateau. Both parameters are increased and decreased by 2 orders of magnitude, the results are shown in Figure 3.24.

The sweep clearly doesn't affect neither Q1 nor Q2, the boost of both MI1 and MI2 is not impacting neither on the plateaus voltages, while their reduction results in a stronger activation polarization. By setting MI1=1E-2, the resulting shape of the first plateau strongly deviates from experimental data, while by MI2=1E-2 the tails of the curves resemble more the empirical observations.

### Discharge Curves: MI1/MI2 Sweep

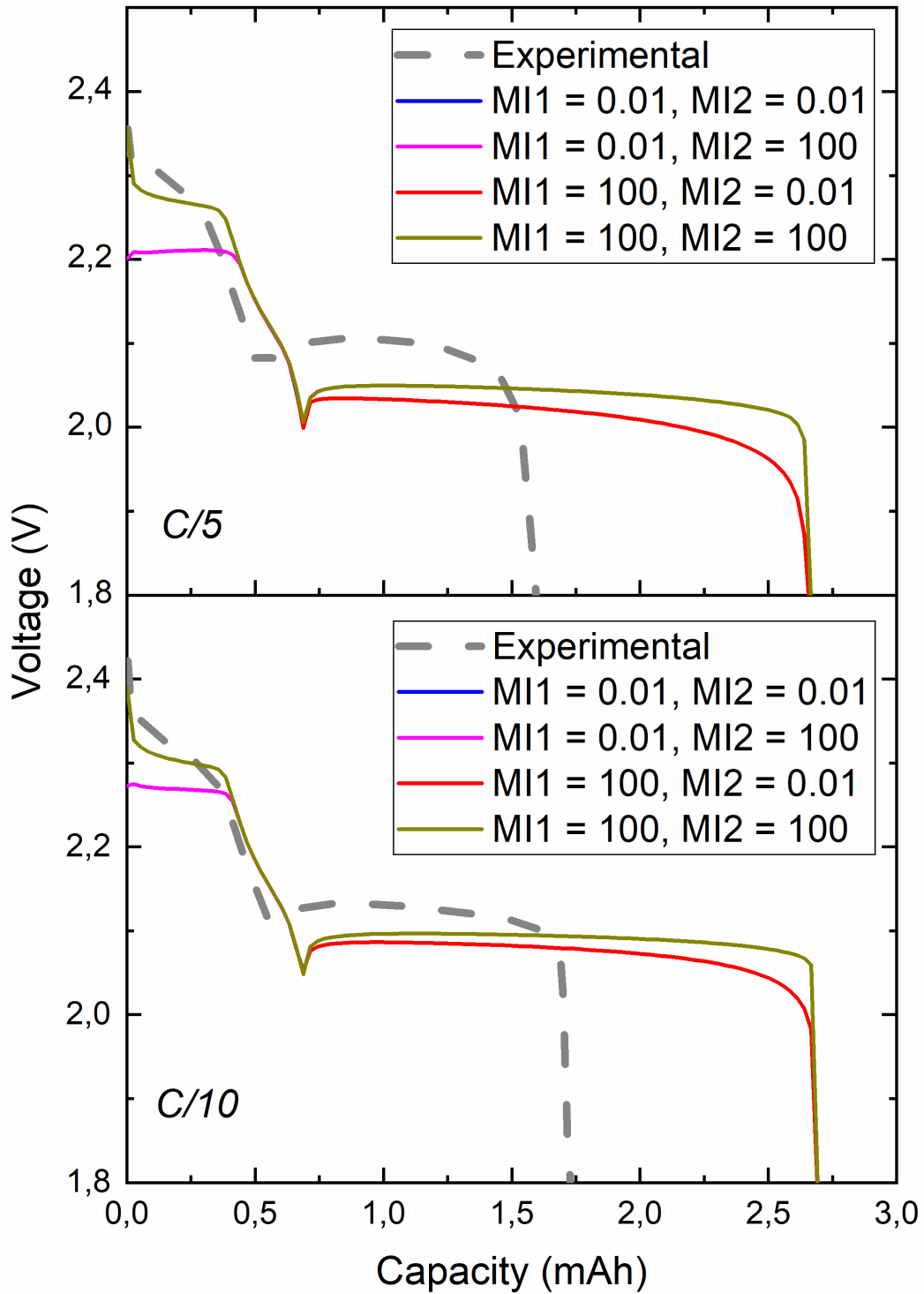


Figure 3. 24 – Parametric sweep on MI1 and MI2

### 3.2.2 Model calibration by experimental and literature data

The strong discrepancy between experimental data and simulated curves proposed in the previous chapter suggests the requirement for an update of the physico-chemical parameters adopted in the model.

#### 3.2.2.1 Diffusion coefficients

An important aspect to be considered in the calibration and validation phase is the nature of the species constituting the simulation domains.

The Zhang solvent is sulfone based, differing from the DME:DIOX 1:1 v/v adopted in the experimental part.

Data found in literature regarding Molecular Dynamics simulation on the interaction between solvent and dissolved species [41] could be employed, neglecting minor deviations in terms of LiTFSI and LiNO<sub>3</sub> concentration:

$$D_{Li^+} \approx D_{TFSI^-} \approx D_{NO_3^-} (= D_{A^-}) \approx 5 * 10^{-10} \frac{m^2}{s} \quad (3.16)$$

Where  $A^-$  represents both  $TFSI^-$  and  $NO_3^-$  in the proposed case.

The value of the diffusion coefficient of dissolved sulfur is evaluated in [42] as:

$$D_{S_8} = 2.6 * 10^{-6} \frac{cm^2}{s} = 2.6 * 10^{-10} \frac{m^2}{s} \quad (3.17)$$

Considering the diffusion coefficients of polysulphides, an approximated increase of two orders of magnitudes compared to the Zhang parameters is adopted, resulting in values similar to the Kumaresan ones.

The list of update bulk diffusion coefficients is provided in Table 3.5.

Parameter	Zhang	Proposed Values
D_Li_1p	8,80E-13 m <sup>2</sup> /s	5E-10 m <sup>2</sup> /s
D_S8	8,80E-12 m <sup>2</sup> /s	2.5E-10 m <sup>2</sup> /s
D_S8_2m	3,50E-12 m <sup>2</sup> /s	3.5E-10 m <sup>2</sup> /s
D_S6_2m	3,50E-12 m <sup>2</sup> /s	3.5E-10 m <sup>2</sup> /s
D_S4_2m	1,75E-12 m <sup>2</sup> /s	1.75E-10 m <sup>2</sup> /s
D_S2_2m	8,80E-13 m <sup>2</sup> /s	8.8E-11 m <sup>2</sup> /s
D_S_2m	8,80E-13 m <sup>2</sup> /s	8.8E-10 m <sup>2</sup> /s
D_A_1m	3,50E-12 m <sup>2</sup> /s	5E-10 m <sup>2</sup> /s

*Table 3. 5 - Calibration on bulk diffusion coefficients*

The proposed diffusion coefficients are also in accordance with experimental data obtained from CV and GITT study, after proper manipulation to convert them from effective to bulk values, considering the effect of porosity.

### 3.2.2.2 Solubility product of octasulfur

The importance of the dissolution of octasulfur in the solvent has been addressed in the first chapter of the thesis: so, an update of the solubility product is required to represent more accurately the operation of the system.

Literature [21] suggests a lower value than the one proposed by Zhang, considering the cell being at equilibrium at the beginning of the discharge phase. The solubility product is adopted also as the reference concentration of dissolved S<sub>8</sub>, whose values are reported in Table 3.6.

*Table 3. 6 – Calibration on octasulfur dissolution properties*

Parameter	Zhang	Proposed Values
Ksp_S8_s	19 mol/m <sup>3</sup>	5 mol/m <sup>3</sup>
c_S8_ref	19 mol/m <sup>3</sup>	5 mol/m <sup>3</sup>

The calibrated discharge curves are proposed, together with pre-calibrated ones and experimental results, in Figure 3.25.

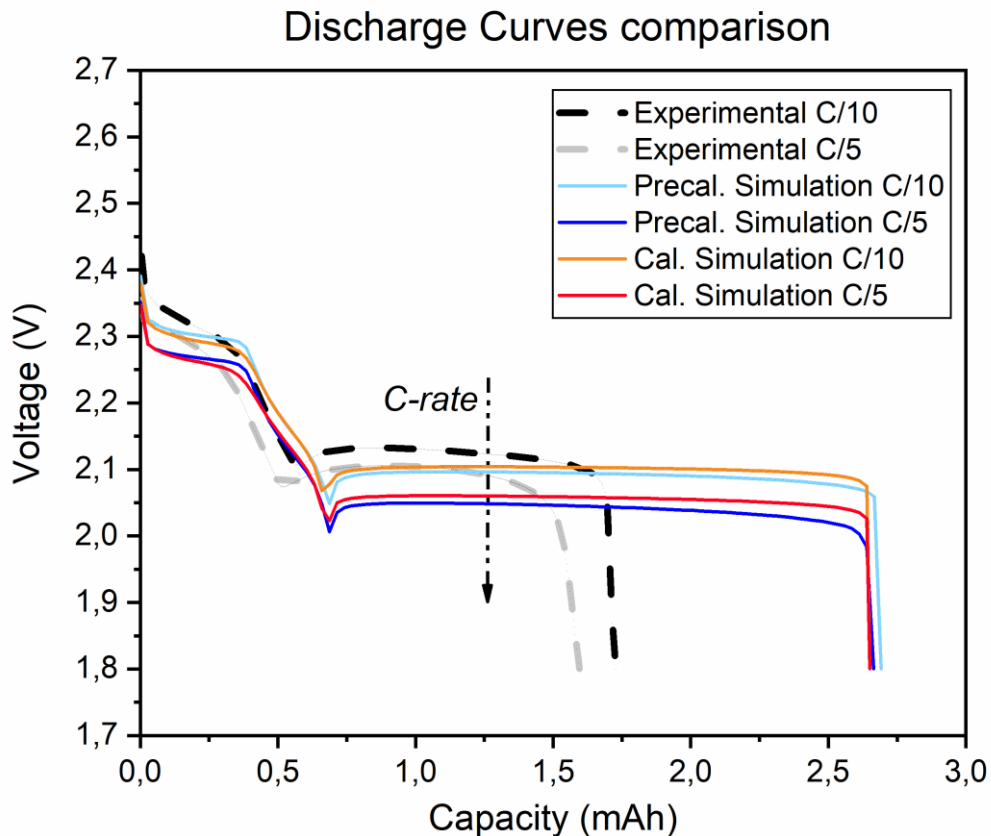


Figure 3. 25 – Comparison between calibrated, precalibrated curves and experimental data

The results of this calibration stage are not satisfactory. The calibrated curves in both cases almost overlap with the precalibrated ones, showing a slightly lower first plateau voltage and slightly higher second plateau voltage, losing the capacity sensitivity to C-rate.

It is required to perform an in-depth analysis on model parameters which could not be straightforwardly evaluated but could strongly impact the behaviour of LSBs.

### 3.2.3 Proposal of model calibration by structural modifications

As the modification in model parameters appears to be ineffective for the calibration purpose, a structural modification of the equations is proposed.

### 3.2.3.1 Approaching calibration by introducing $Li_2S_2$ species

The introduction of the species  $Li_2S_2$  could allow to increase the accuracy of the model and provide a further degree of freedom which might be helpful in the calibration and validation.

According to Zhang, the above-mentioned species is not detected as a final product in the discharge phase, but there is no unanimous consent on this issue as several more updated papers in literature report evidence of its presence.

The deposition reaction of  $Li_2S_2$  is also considered in Kumaresan model, thus reaction parameters required for the computation are adopted from his studies.

The main reason leading to this implementation is the effect in reducing Q2 (Figure 3.26).

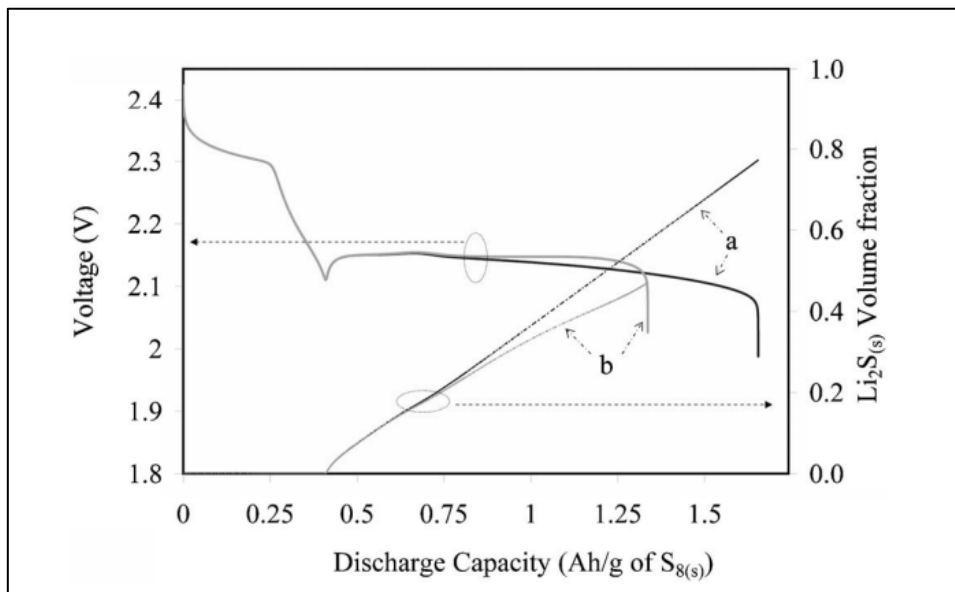


Figure 3. 26 - Effect of  $Li_2S_2$  precipitation kinetics on Q2 [2]

As implicitly suggested, controlling the kinetic of deposition would allow, within some extents, to tune Q2.

At first, the adoption of the same values employed by Kumaresan is considered, being:

$$k_{Li_2S_2(s)_1} = 9.98e - 4 \text{ s}^{-1}; \quad (3.18)$$

$$k_{Li_2S_2(s)_2} = 0.05 \text{ s}^{-1} \quad (3.19)$$

Where the second value differs from the first one by 2 orders of magnitude, implying a much faster kinetic, thus an overall higher volumetric fraction of  $Li_2S_2$  at the end of the discharge.

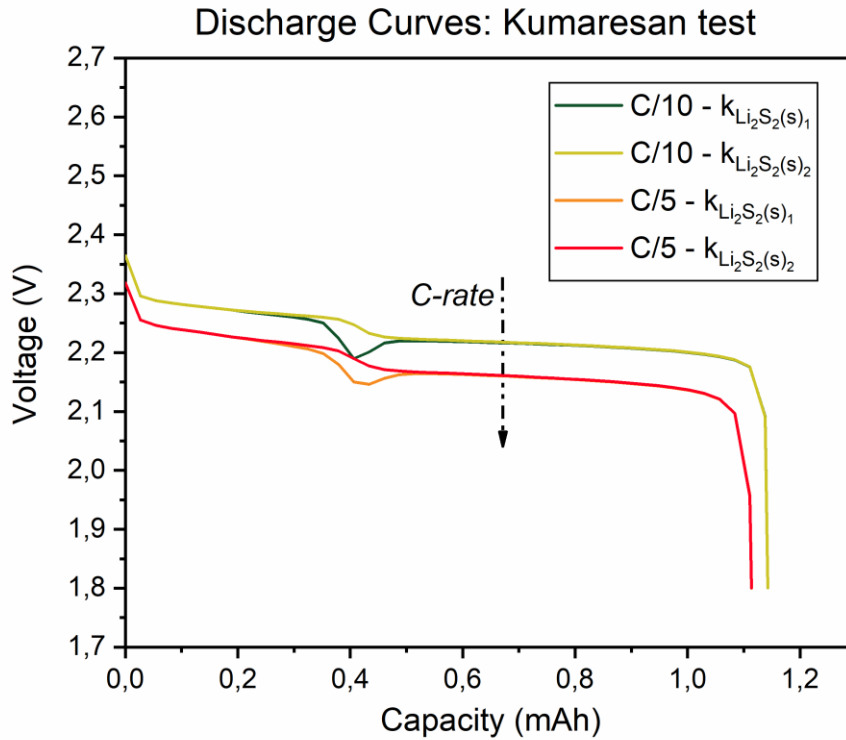


Figure 3. 27 – Evaluation of Kumaresan proposed parameters for  $Li_2S_2$  precipitation kinetics

As the simulation results (Figure 3.27) strongly differ from the expected curves, a parametric sweep of both the  $Li_2S$  and  $Li_2S_2$  precipitation rate constants is performed. As base values the ones proposed by Zhang and Kumaresan models are adopted, employing multiplying coefficients MK1 and MK2.

$$k'_{Li_2S(s)} = MK1 * k_{Li_2S(s)} \quad (3.20)$$

$$k'_{Li_2S_2(s)} = MK2 * k_{Li_2S_2(s)} \quad (3.21)$$

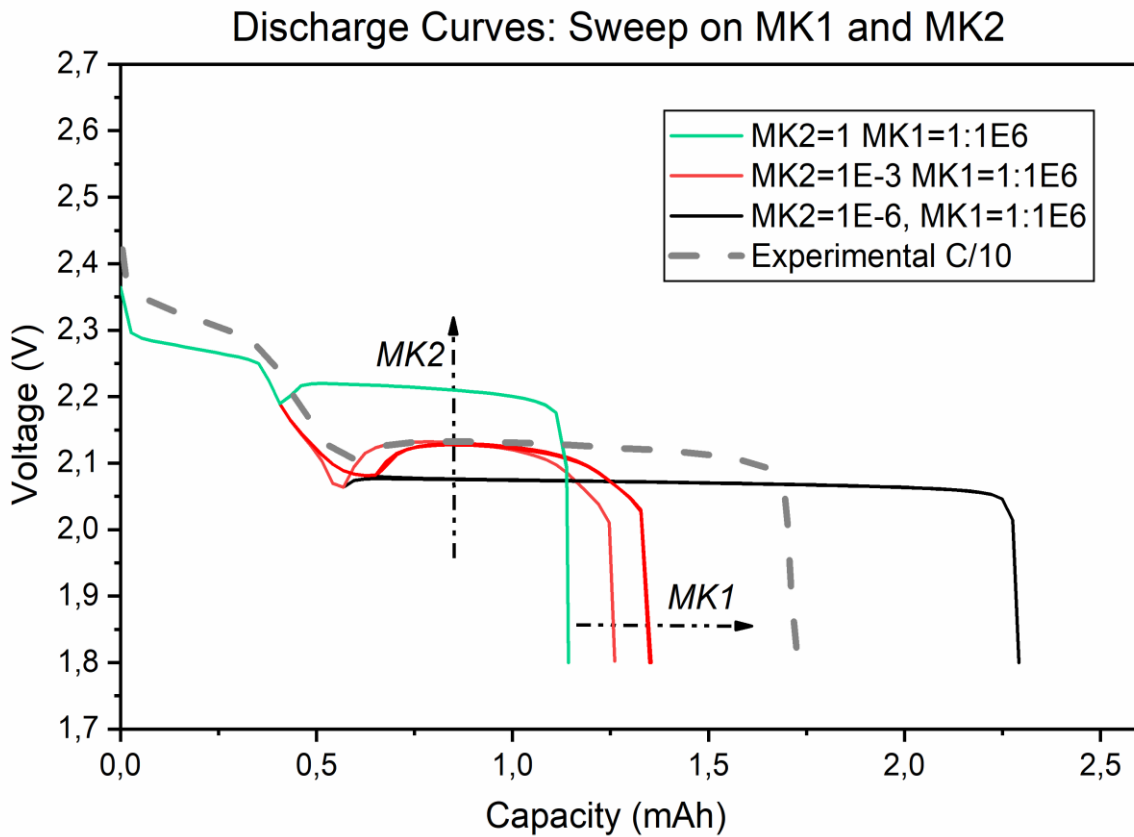


Figure 3. 28 – Sweep on kinetic multipliers MK1 and MK2

By analysing the results (Figure 3.28), it's clear that tuning both parameters strongly influence the shape of discharge curves.

The sensitivity of the model to MK1 is extremely low, thus for further analysis a parametric sweep on MK2 only is considered.

The 6 orders of magnitude increment from the base value leads to an evident reduction of inter-plateaus peak steepness, which could be ascribed to a milder increase in viscosity of the electrolyte as  $Li^+$  and  $S^{2-}$  react more rapidly to form  $Li_2S$ .

Regarding the MK2 sweep, the high rate of precipitation of  $Li_2S_2$  of the base case would lead to a fast consumption of  $S_2^{2-}$  that compete with the last reduction semi-reaction of the model producing  $S^{2-}$  ions. This will bring to  $Li_2S$  precipitation, resulting in high second plateau voltage and lower Q2., For this reason, a reaction slowdown has been considered.

By decreasing MK2 by 6 orders of magnitude, the discharge curve regains the usual experimental-like shape, but it is still characterized by much lower Q2 than experimental evidence.

A more focused sweep has been performed on MK2 over 1E-4 order of magnitude, as it is found to be a transition zone to tune Q2 (Figure 3.29).

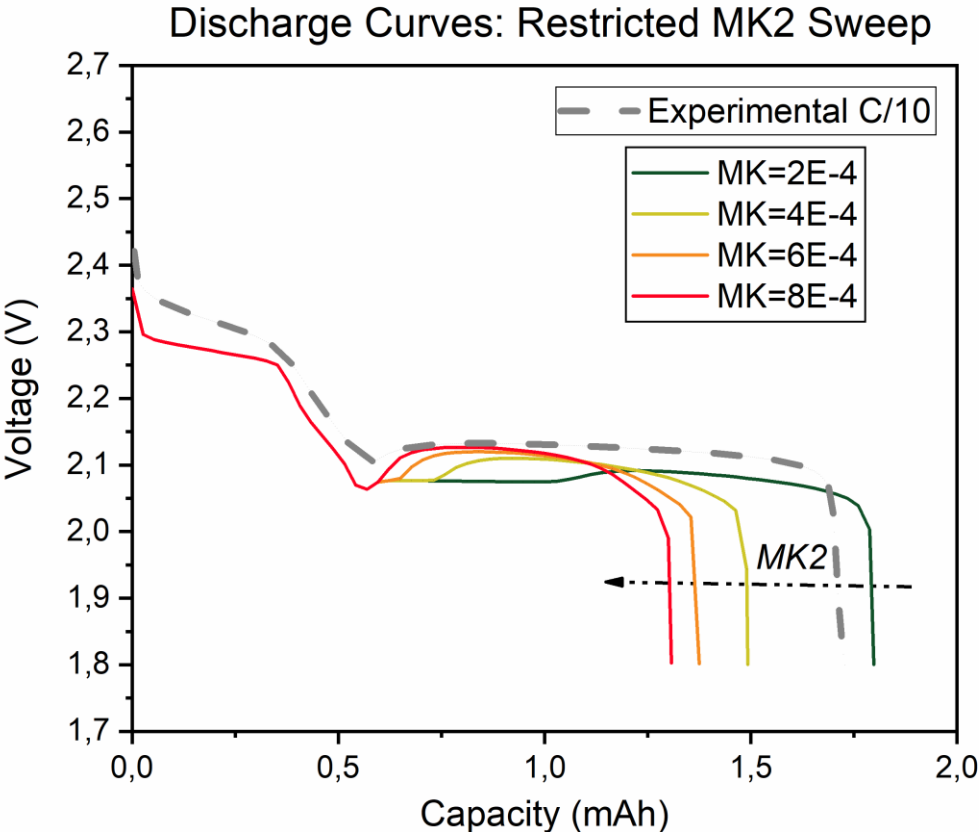


Figure 3. 29 - Restricted parametric analysis on MK2

It can be stated that a calibration based on the introduction of  $Li_2S_2$  allows an easy tuning of Q2 from a model-fitting perspective. Unfortunately, the simulated shape of the second plateau shows a strong discrepancy with the experimental data indicating a kinetic insurgence of  $Li_2S_2$  by a sudden voltage increase. So new considerations should be taken into account with the purpose to improve the calibration of the model curves with the experimental ones.

### 3.2.3.2 Focus on $Li_2S$ precipitation and porosity

The impact of  $Li_2S$  precipitation in determining capacity loss at variable C-rate is evaluated.

In the discharge process solid octasulfur dissolves, leading to a higher volumetric fraction of electrolytes, which reduces as  $Li_2S$  precipitates along the process. This results in a volume expansion up to 80%, compared to SOC = 100% in sulfur abundant cathodes, and changes not only in porosity, but also in pores volumes [43].

#### 3.2.3.2.1 *Sulfur volumetric fraction/porosity sweep*

In order to evaluate profoundly the role of  $Li_2S$  precipitation, a parametric analysis with a focus on the calibration purpose is performed.

The model sensitivity to the parameter  $\epsilon_{pos,0}$  could be verified to account for its impact in the species initial volume fraction in the solid material  $\epsilon_{S_8,spos,0}$ . The following relationship is imposed:

$$\epsilon_{S_8,spos,0} = f_{v,mix,S_8,s}(1 - \epsilon_{pos,0}); \quad (3.22)$$

$$f_{v,mix,S_8,s} = 0.13 \quad (3.23)$$

Where  $f_{v,mix,S_8,s}$  is calculated based on the estimated volumetric fraction of  $S_8$ .

The applied C-rate is kept constant for different porosity values, since it is related to the mass loading. The simulation results are depicted in Figure 3.31.

The model response to the porosity sweep is evident, showing a good fitting with the experimental C/10 curve for  $\epsilon_{pos,0}$ .

The adoption of diffusion coefficients close to Kumaresan set values hinders the discharge capacity sensitivity at different C-rates, while the polarization discrepancy between simulated curves is excessive compared to the experimental curves.

The adoption of  $\epsilon_{pos,0} = 0.4$  leads to a good fit of the decreasing potential between the two plateaux at C/10 and C/5, while  $\epsilon_{pos,0} = 0.6$  accurately represents the C/10 discharge capacity.

### Discharge Curves: sweep on cathode porosity

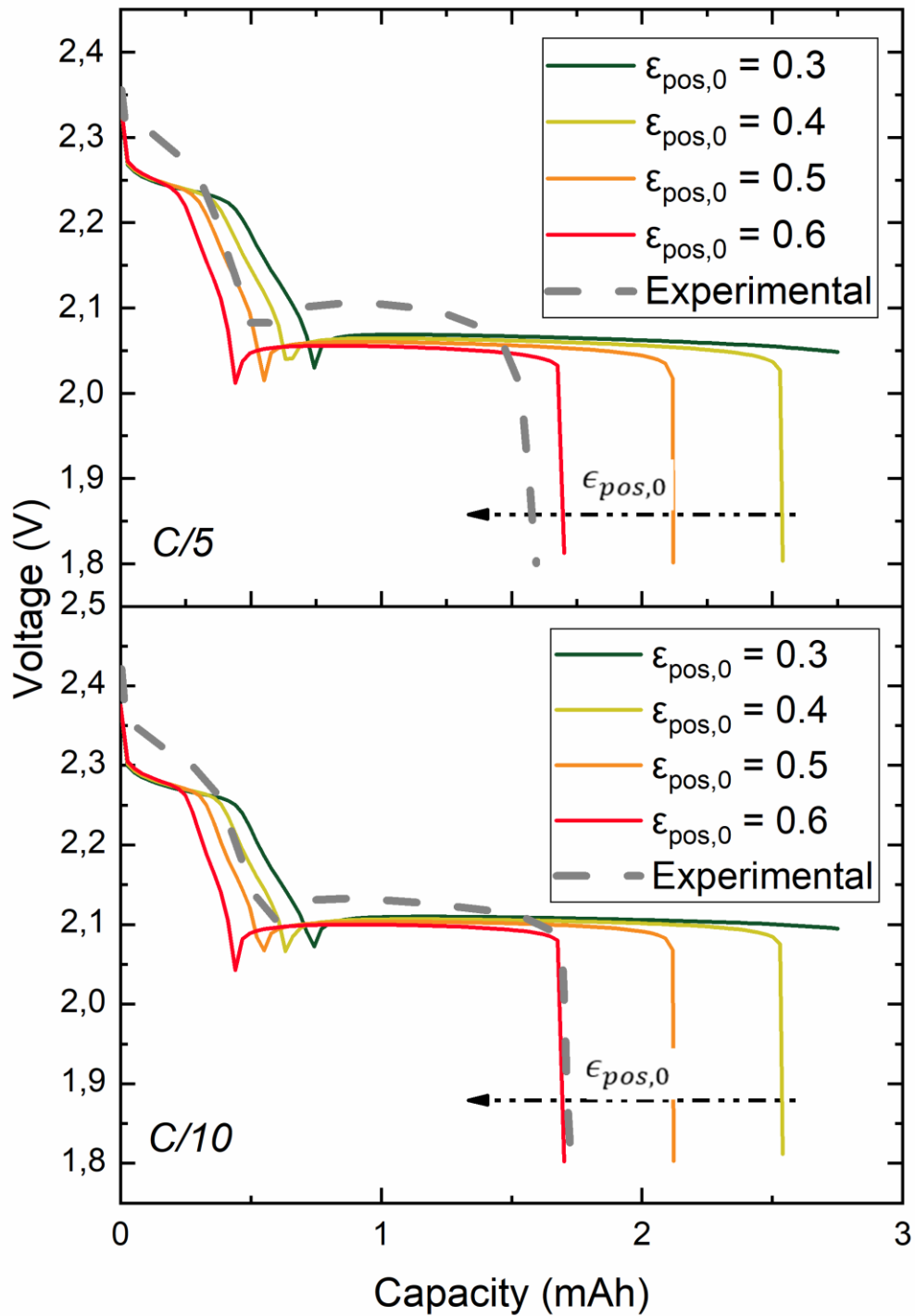


Figure 3. 29 – Evaluation of the impact of cathode porosity on simulated discharge curves

### 3.2.3.2.2 Further analysis on model parameters

There is no experimental evidence of  $Li_2S$  presence in fresh cells as a product of incomplete charge, differently from already cycled units. Anyway, it's mandatory to consider that a null value of  $\epsilon_{Li_2S,pos,0}$  would lead to a null precipitation rate over the discharge process.

The initial value, which is guessed to be extremely low, is exploited for fitting purposes only and not included in the above-mentioned volume fraction balance (Equation 3.21).

The kinetic multiplier MK1 is employed to investigate the impact of changing the precipitation rate constant by different orders of magnitude.

The electronic conductivity of the cathode is expected to have an impact on ohmic polarization.

Including a variation of this parameter over the discharge, as the bulk positive electrode changes its composition in the process, would be an interesting investigation strategy. Therefore, a parametric analysis, shown in Figure 3.31, was performed to evaluate the suitability of this approach.

The most impacting parameter on the discharge curve, among the ones considered, is MK1, that defines three voltage levels as second plateau positions, where the most noticeable effect occurs for  $MK1=1E-3$  as a strong polarization effect.

By reducing MK1, a wide supersaturation peak occurs due to a slower  $S^{2-}$  and  $Li^+$  depletion by  $Li_2S$  precipitation, causing a delayed stabilization of the second plateau voltage.

At  $MK1 = 1E3$  the opposite effect occurs, while the second plateau position scarcely differs from  $MK1 = 1$ .

The sensitivity analysis on  $\sigma$  provides unsatisfying results; its variation by 4 orders of magnitude, that simulates a change in composition, apparently provides no effect.

### MK1 Discharge Curves Sweep

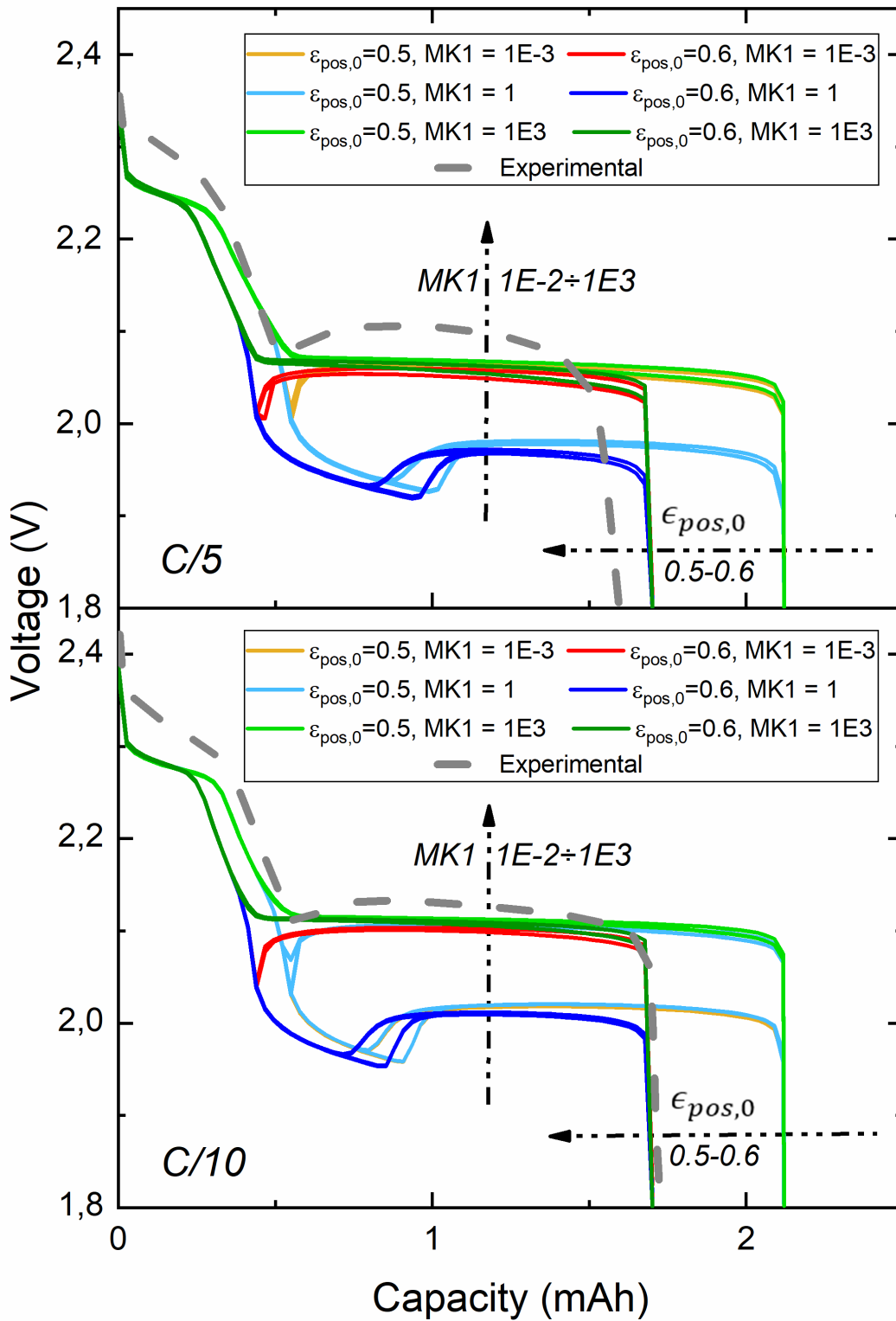


Figure 3. 30 – Evaluation of the impact of MK1,  $\sigma$  and  $\epsilon_{Li_2S, pos, 0}$  on discharge curves

Considering the influence of the cathodic volumetric fraction of  $Li_2S$ , no significant repercussion is noticed at  $MK1=1E3$  while a slight effect occurs in the other cases, softening the supersaturation peak at  $MK1=1$  and anticipating the voltage recovery at  $MK1=1E-3$ .

### 3.2.3.2.3 Combined analysis on the roles of specific surface area and porosity

The specific surface area has a determining role in the model operation, since it is related to the kinetic of electrochemical reactions and to the structure porosity by a morphological power law.

Experimental evidence suggests a strong correlation between specific surface area, porosity and electrochemical performances.

In fact, Zheng et al. [44] underline the impact on different cathode compositions on the discharge curves profile and on capacity degradation (Figure 3.32).

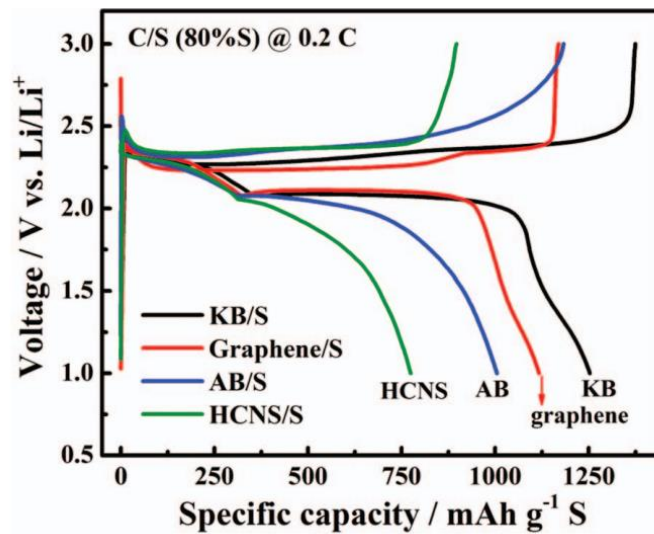


Figure 3. 31 - Specific capacity vs electronically conductive medium employed [44]

For example, Carbon Black and graphene provide more reaction sites, increasing the sulfur utilization, and allow to lower the real current density, thus increasing the discharge capacity and reducing the activation polarization.

The total capacity improvement by increasing the specific surface area available strongly favours the second plateau capacity Q2 while slightly enhances the first plateau capacity Q1.

The findings by Kang et al. [45] are more relevant for comparison to the specific case under analysis, as the relationship between porosity and cell discharge curve performance is investigated adopting the same conductive matrix.

The average sulfur loading among the assembled cell is calculated as:

$$\overline{SL} = \frac{\overline{m_{AM}}}{A_{cell}} = 0.93 \frac{mg}{cm^2} \quad (3.24)$$

The adopted cell assembly approach is similar to the one employed in the experimental part of the thesis, adding an extra 40  $\mu$ l electrolyte for cells with sulfur loading  $SL_a = 2.5 \text{ mg/cm}^2$  and an extra 80  $\mu$ l where sulfur loading is  $SL_b = 5 \text{ mg/cm}^2$ .

It is important to note that the salt concentration also differs; in the mentioned paper which it is set as 0.6 M LiTFSI and 0.4 M LiNO<sub>3</sub> and different porosity values are obtained by a calendaring procedure. In addition, the sulfur loading of the cells studied in the paper is much higher than the average one evaluated in laboratory practice. Considering the  $SL_b$  specimens, it is evident an oscillatory behaviour of capacity at high value of porosity, where at the lowest value a strong decay occurs, mostly ascribed to second plateau suppression due to the lower availability of active area.

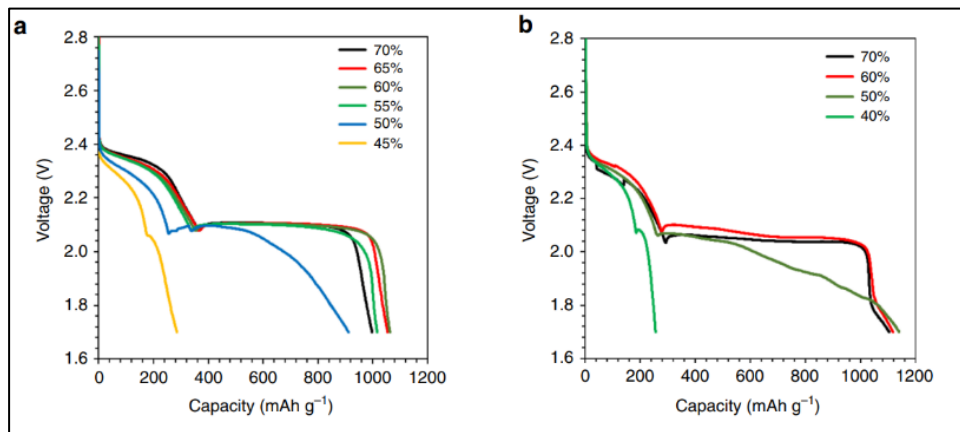


Figure 3. 32 – Effect of porosity on exp. discharge curves in case of low (a) and high mass loading (b) [45]

The impact of porosity in determining the shape of the curves (Figure 3.33) differs from the results by Zheng [44] and Kang [45] while it should be similar to the last one, as the same electronically conductive material is adopted (KJB).

The main discrepancy to Zheng results is related to a scarce impact in the first plateau capacity and shape considering different materials. In the previously presented porosity sweep the curves

keep the same proportion but appear to be resized on the capacity axis, slightly differing from Kang results.

Considering the impact of porosity on model variables, as the correction on diffusion coefficients by Bruggeman relationship, a numerical example is provided, considering the two extreme values adopted in the porosity sweep:

$$\frac{D_{i,\epsilon_{pos,0,A}}^{eff}}{D_{i,\epsilon_{pos,0,B}}^{eff}} = \left( \frac{\epsilon_{pos,0,A}}{\epsilon_{pos,0,B}} \right)^b = \left( \frac{0.3}{0.6} \right)^{1.5} = 0.3535 \quad (3.25)$$

The variation might seem significant but, as previously discussed, in the specific orders of magnitudes under investigation, the overall effect is negligible on the discharge capacity C-rate sensitivity, recalling the Zhang approach to the model.

As tuning the second plateau voltage is a matter of interest, the main hypothesis underlying the parametric analysis is that the model would be highly sensitive to the variation in initial specific surface area in terms of activation polarization resistance, as  $a_{v,0}$  impacts on the charged species source term in the material balance equation.

The availability of extra specific surface area compared to the common value adopted by Zhang and Kumaresan is considered. In fact, in their work a generic “carbon” is stated to constitute the cell conductive matrix, employing a value of  $a_{v,0}$  which is 3 orders of magnitude lower than the one characterizing KJB EC300J.

Since different carbon blacks could show significantly different characteristics [46], the methodology to calculate an average value of  $a_{v,0}$  is not clear., Thus the parameter MAV0 could help in the fitting procedure, also considering the scarce impact that other related multipliers (MI1 and MI2) show in altering the second plateau voltage.

The parameter MAV0 is adopted as a multiplier as reported in the following formula.

$$a_v = MAV0 * a_{v,0} \left( \frac{\epsilon}{\epsilon_0} \right)^\xi \quad (3.26)$$

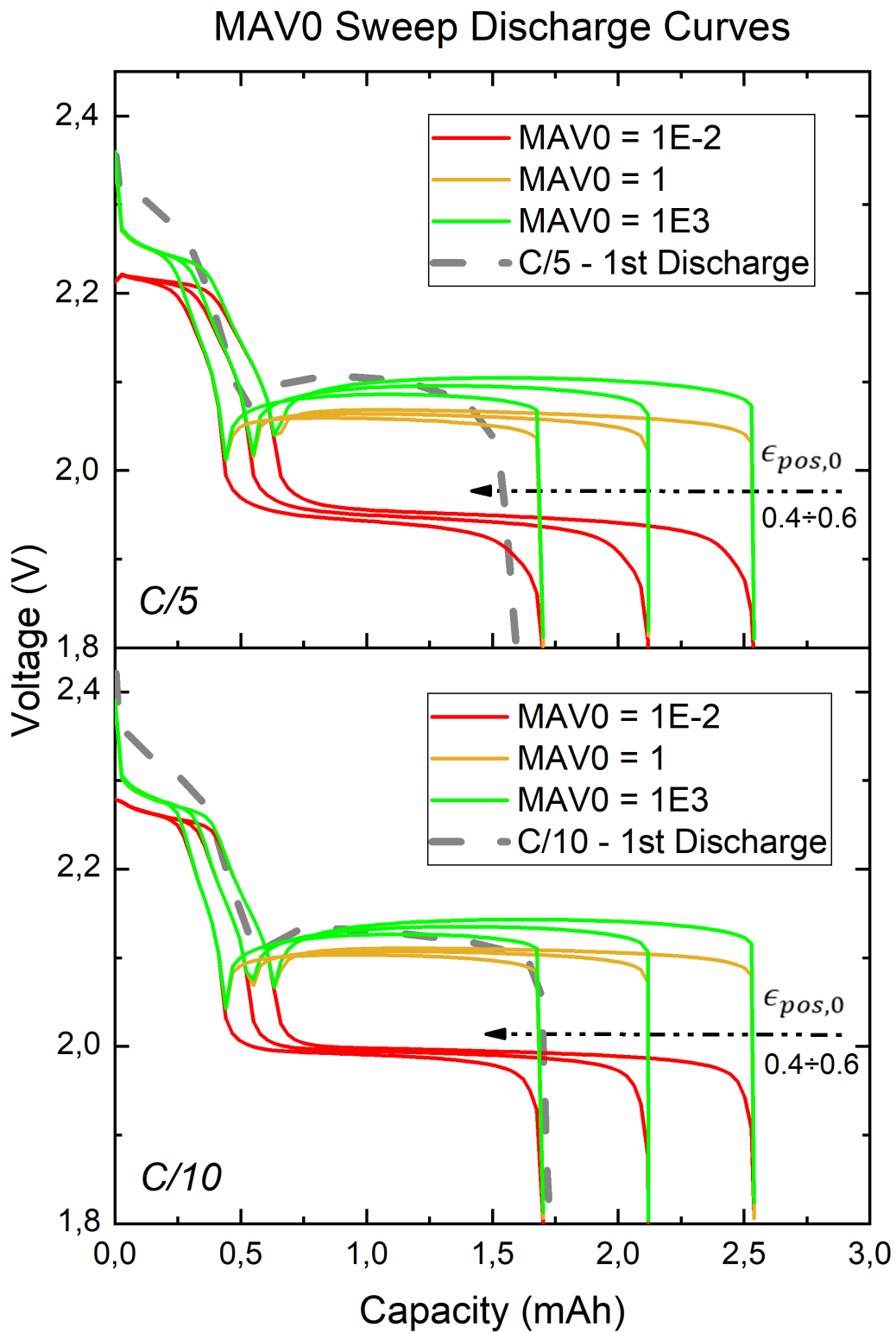


Figure 3. 33 – Evaluation of the impact of the multiplier MAV0 on discharge curves

The impact of MAV0 in determining the shape of discharge curve is clear from Figure 3.34.

Its reduction below the base case leads to a strong activation polarization in both the first and second plateaus. This effect is clearly more marked at higher C-rates, while the shape of the descending branch between the two plateaux is unchanged.

Considering MAV0 = 1E3, a sharp increase in the second plateau voltage occurs, resulting in a slightly more curved shape, in better accordance with experimental data.

Comparing the two extreme cases, it's clear that as the initial porosity increases the second plateaus suffers a higher polarization, while this phenomenon is less noticeable in the base case.

The depth of the supersaturation peak is more pronounced at higher porosity at C/10 C-rate, while the relationship is not clear in the C/5 case.

### 3.2.4 Model Validation

The impact of specific surface area is further investigated, beyond its mere initial value modification, focusing in depth on its morphological relationship with porosity. So two extra parameters are introduced in the formulas of specific surface area and effective diffusion coefficient.

$$a_v = MAV0 * a_{v,0} \left( \frac{\epsilon}{\epsilon_0} \right)^{MEXAV * \xi} \quad (3.27)$$

$$D_i^{eff} = D_i(\epsilon)^{MEXB * b} \quad (3.28)$$

The parameter MEXAV is the multiplier adopted in the power law relating the evolution of porosity and specific surface area.

Its employment is justified by the fact that in both Kumaresan and Zhang papers the methodology adopted to evaluate  $\xi$  is not clarified and recent discoveries on the morphology of precipitate might lead to an adjustment of this parameter.

Over the discharge, a considerable share of the KJB surface is covered by  $Li_2S$ . For this reason, its polarization impact due to the insulating nature of the precipitate is revised compared to the previous research results.

$Li_2S$  precipitates forming 2D patches, but, then a 3D growth occurs due to the interaction with disproportionation reactions of PS. Subsequently both mechanisms occur simultaneously leading to a very complex morphology [47], hindering the availability of specific surface area over the discharge process.

The multiplier MEXB is employed to modify the Bruggeman relationship since experimental evidence shows a strong polarization effect directly driven by diffusion [47]. Thus, considering also that a complex morphology of the precipitate, which is an insulating phase not only for electron transfer but also for mass transfer, would strongly impact on tortuosity over the discharge, its adoption might be useful to describe at best the phenomenon.

A parametric analysis on the described parameters is performed and the best fitting curves are presented in Figure 3.35., while the fitting parameters are shown in Table 3.7.

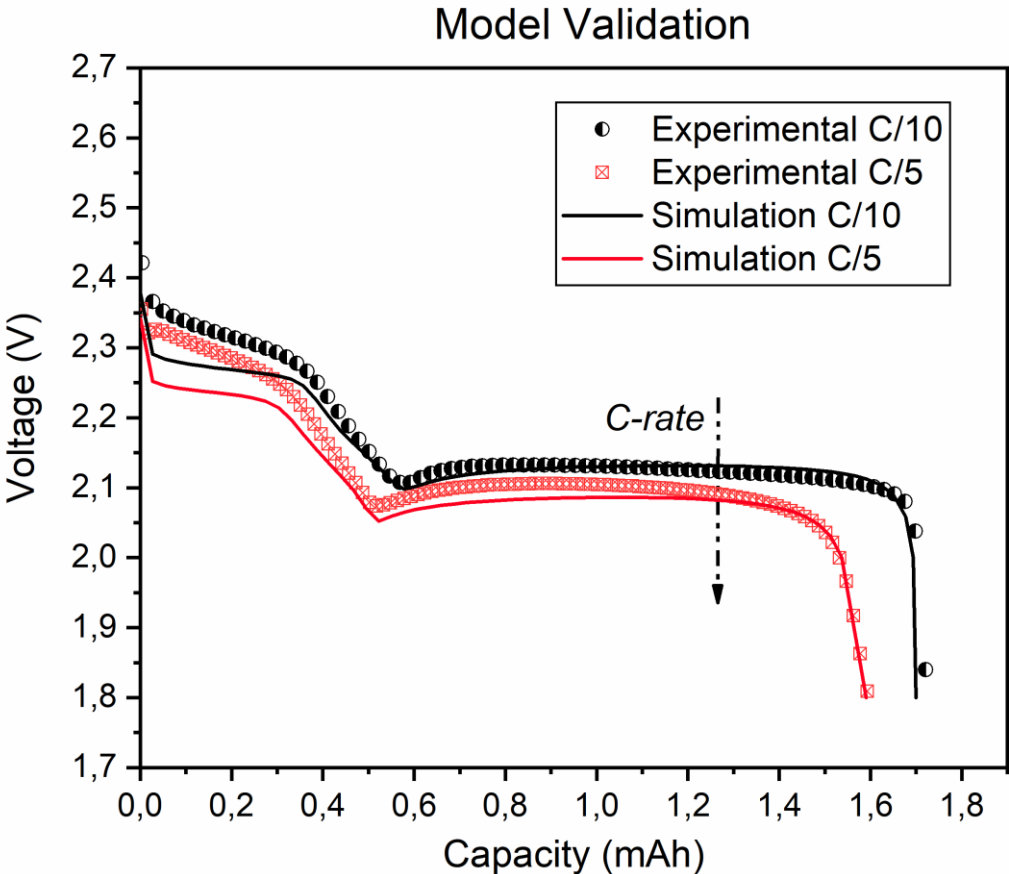


Figure 3. 34 - Validation of the model

Table 3. 7 - Validation parameters

C-rate	MAV0	MEXAV	MEXB
C/5	100	4.5	6.95
C/10	100	3.3	6.55

Regarding the C/10 curve, it is evident that, while accurately describing the experimental behaviour from the descending branch to the end of the discharge, a clear discrepancy occurs on the first plateau voltage. A similar phenomenon can be seen on C/5 curve.

In both cases a further analysis (Figure 3.36) demonstrates that the limiting factor is related to the solubility product of octasulfur, nonetheless, adopting this parameter for fitting purposes would lead to discrepancy with the experimental data present in literature [21].

In Kumaresan and Zhang works, this parameter is declared to be assumed, thus it was probably adopted to fit at best the curves.

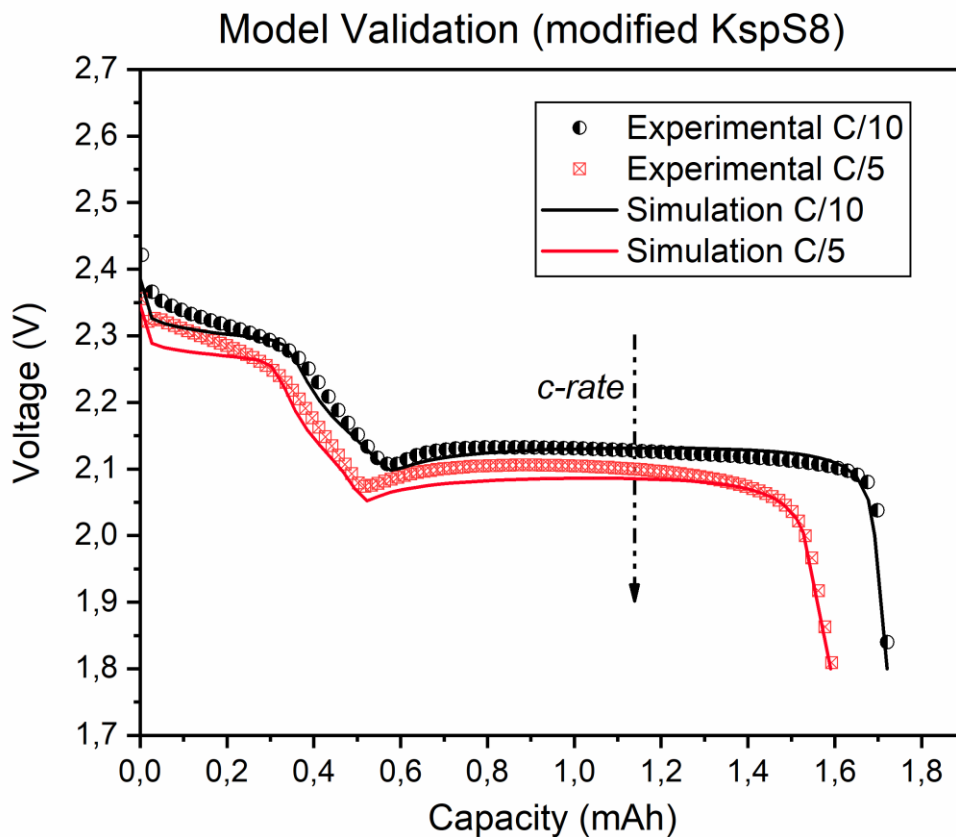


Figure 3. 35 - Validation of the model (modified  $K_{sp,S_8(s)}$ )

The capacity Q1 though is accurately described by the simulated curves.

At low C-rates the deposition of  $\text{Li}_2\text{S}$  doesn't expand the pores of the carbon matrix as it mostly precipitates in the mesopores (2-50nm) and limits the ionic transport properties by replacing the electrolyte [48].

Following the precipitation, the formation of different  $\text{Li}_x\text{S}_y$  structures at different C-rates leads to a different morphology which could justify the different sulfur utilization. Combining this effect with the increasing diffusion resistance at low C-rates, these factors could justify the adoption of different parameters for the simple morphological equations adopted [47][48].

The employment of more complex relationship between porosity, specific surface area and effective diffusion coefficients could lead to adopt fitting parameters, which are not C-rates dependent, allowing an easier calibration of the model.

## 4. Conclusions

Lithium-sulfur batteries are a promising technology, capable to foster the sustainable development in economy, society and environment.

LSBs present high energy density and specific energy due to the adoption of sulfur at cathode, an abundant and cheap material featuring an exceptional specific capacity of 1675 mAh/g.

The main limitations hindering the spreading of these systems are related to the complex reaction mechanism of  $S_8$  reduction, producing intermediate species, lithium polysulfides, responsible of the shuttle phenomenon, reducing the utilization of active material, causing anode corrosion and modest cycle-life.

To aid in system design and experimental activities, the development of a robust computational model would allow to correctly predict the behaviour of LSBs in different operating conditions.

A comparison between the models proposed by Kumaresan and Zhang is performed, focusing on both their bright sides and their limitations. In particular, Zhang model is capable to reproduce a discharge curve which qualitatively shows all the characteristic of an experimental one, while the proposed diffusion limiting approach has a limited accuracy at low C-rates.

In order to improve the model, an analysis of the electrochemical parameters has been performed with the purpose to calibrate and validate the model with the experimental discharge profiles. In this aim, coin cells have been assembled at DISAT electrochemistry laboratory and tested by mean of Galvanostatic Cycling (GC), Potentiostatic Electrochemical Impedance Spectroscopy (PEIS), Cyclic Voltammetry (CV) and Galvanostatic Intermittent Titration Technique (GITT), providing useful data to perform the model calibration.

After a focus on  $Li_2S$  precipitation mechanism, the most effective approach, combining both the calibration and validation phases, resulted to be the adoption of specific multipliers acting on the relationship between specific surface area, porosity and effective diffusion coefficients.

For further studies purpose, the adoption of more complex morphological relationships is suggested, as it could allow to adopt a single set of fitting parameters for a wide range of operating conditions and eventually permit to model the behaviour of cells featuring composite cathodic structures.

# Bibliography

- [1] “*Our Common Future (Brundtland Report)*”, Oxford University Press, 1987
- [2] “Net Zero by 2050, A Roadmap for the Global Energy Sector”, International Energy Agency, 2020
- [3] “*Lithium–Sulfur Batteries*”, M. Wild, Gregory J. Offer, John Wiley & Sons Ltd, 2019
- [4] “*Electrochemistry*”, P. H. Rieger, Springer Netherlands, 1993
- [5] “*Electrochemical Power Sources: Batteries, Fuel Cells, and Supercapacitors*”, V. S. Bagotsky et al., John Wiley & Sons Inc, 2015
- [6] Notes of the course “Polygeneration and advanced energy systems” held by Professor Massimo Santarelli at Polytechnic of Turin, A.Y. 2021/2022
- [7] “*Key Performance Indicators for the monitoring of large-scale battery storage systems*”, Björn Laumert, KTH, 2019
- [8] “*Thermal stability studies of Li-Ion Cells and Components*”, H. Maleki et al., Journal of The Electrochemical Society, 1999
- [9] “*Global Lithium Sources - Industrial Use and Future in the Electric Vehicle Industry: A Review*”, Laurence Kavanagh, J. Keohane et al., Resources, MDPI, 2018
- [10] “*Literature Review and Thermodynamic Modelling of Roasting Processes for Lithium Extraction from Spodumene*”, A. Fosu et al., Metals, MDPI, 2020
- [11] United States Geological Survey (USGS) - National Minerals Information Center - Mineral Commodity Summaries 2022 – Lithium
- [12] “*Extractivism and its socio-environmental impact in South America. Overview of the “lithium triangle”*”, E. Giglio, América Crítica, UniCA Open Journals, 2021
- [13] “*Thermal Stability Studies of Li-Ion Cells and Components*”, H. Maleki et al., Journal of The Electrochemical Society, ECS, 1999
- [14] “*Recent developments in cathode materials for lithium ion batteries*”, J. W. Fergus, Journal of Power Sources, Elsevier, 2010

- [15] “*High Performance of Salt-Modified–LTO Anode in LiFePO<sub>4</sub> Battery*”, P. Agus et al., Applied Sciences, Basel, 2020
- [16] “*Nano/Microstructured Silicon–Graphite Composite Anode for High-Energy-Density LiIon Battery*”, ACS Nano, American Chemical Society, 2019
- [17] “*Lithium Germanate (Li<sub>2</sub>GeO<sub>3</sub>): A High-Performance Anode Material for Lithium-Ion Batteries*”, Md. Rahman et al., Angewandte Chemie, Blackwell Publishing Ltd, 2016[13]
- “*Recent developments in cathode materials for lithium ion batteries*”, J. W. Fergus, Journal of Power Sources, Elsevier, 2010
- [18] “*Advances in lithium-sulfur batteries*”, X. Zhang et al., Material Science and Engineering R, Elsevier, 2017
- [19] “*A Comprehensive Understanding of Lithium–Sulfur Battery Technology*”, T. Li et al., Advanced Functional Materials, Wiley-VCH GmbH, Weinheim, 2019
- [20] “*Lithium sulfur batteries, a mechanistic review*”, M. Wild et al., Energy & Environmental Science, Royal Society of Chemistry, 2015
- [21] “*The Significance of Elemental Sulfur Dissolution in Liquid Electrolyte Lithium Sulfur Batteries*”, P. P. R. M. L. Harks et al., Advanced Energy Materials, Wiley-VCH GmbH, 2017
- [22] “*A Mathematical Model for a Lithium–Sulfur Cell, K. Kumaresan et al.*”, Journal of The Electrochemical Society, 2008
- [23] “*Revisiting the Role of Polysulfides in Lithium–Sulfur Batteries*”, G. Li et al., Advanced Materials, Wiley-VCH GmbH, Weinheim, 2018.
- [24] “*Polysulfide Shuttle Study in the Li/S Battery System*”, Y. Mikhaylik et al., Journal of The Electrochemical Society, ECS, 2004
- [25] “*Molybdenum disulfide/polyaniline interlayer for lithium polysulphide trapping in lithium-sulphur batteries*”, D. Versaci et al., Journal of Power Sources, Elsevier, 2022
- [26] “*Influence of synthesis parameters on g-C<sub>3</sub>N<sub>4</sub> polysulfides trapping: A systematic study*”, D. Versaci et al., Applied Materials Today, Elsevier, 2021
- [27] “*Efficient electrolytes for lithum-sulfur batteries*”, N.Angulakshmi et al., Frontiers in Energy Research, 2015

- [28] “*Electrolyte Issues in Lithium–Sulfur Batteries: Development, Prospect, and Challenges*”, G. Liu et al., Energy Fuels, 2021
- [29] “*Calcolo Scientifico*”, Alfio Quarteroni et al., Springer, 2017
- [30] The Electrochemistry Module User’s Guide, COMSOL, 2017
- [31] “*POROUS-ELECTRODE THEORY WITH BATTERY APPLICATIONS*”, Newman, J., & Tiedemann, W., Lawrence Berkeley National Laboratory. LBNL Report #: LBL-3117., 1974
- [32] “*Modelling transport-limited discharge capacity of lithium-sulfur cells*”, T. Zhang et al., Electrochimica Acta, Elsevier, 2016
- [33] “*On the origin and application of the Bruggeman correlation for analysing transport phenomena in electrochemical systems*”, B. Tjaden et al., Current Opinion in Chemical Engineering, Elsevier, 2016
- [34] “*Investigation of the Effect of Temperature on Lithium-Sulfur Cell Cycle Life Performance Using System Identification and X-Ray Tomography*”, N. Shateri et al., Batteries & Supercaps, 2022
- [35]  
[https://www.disat.polito.it/it/il\\_dipartimento/strutture\\_interne/laboratori\\_interni/laboratori\\_area\\_chimica\\_per\\_1\\_ingegneria/laboratorio\\_elettrochimica\\_2\\_sistemi\\_li\\_ione\\_tecnologie\\_post\\_li\\_ione](https://www.disat.polito.it/it/il_dipartimento/strutture_interne/laboratori_interni/laboratori_area_chimica_per_1_ingegneria/laboratorio_elettrochimica_2_sistemi_li_ione_tecnologie_post_li_ione)
- [36] “*Lithium sulfur batteries, a mechanistic review*”, M. Wild et al., Energy & Environmental Science, Royal Society of Chemistry, 2015
- [37] “*Characterization of batteries by electrochemical impedance spectroscopy*”, L.A. Middlemiss et al., Energy Reports 6, Elsevier, 2020
- [38] Linear Voltammetry - Andrew McKinley lectures on physical chemistry
- [39] “*Cyclic Voltammetry in Lithium–Sulfur Batteries—Challenges and Opportunities*”, X. Huang et al., Energy Technology, WILEY-VCH Verlag GmbH, 2019
- [40] “*Quantitative Galvanostatic Intermittent Titration Technique for the Analysis of a Model System with Applications in Lithium-Sulfur Batteries*”, J.W. Diben, ChemElectroChem, Wiley-VCH Verlag GmbH & Co. KGaA, Weinheim, 2018

- [41] “*Molecular simulations of electrolyte structure and dynamics in lithium-sulfur battery solvents*”, C. Park et al., Journal of Power Sources, Elsevier, 2017
- [42] “*Probing the Lithium-Sulfur Redox Reactions: A Rotating-Ring Disk Electrode Study*”, Y. Lu et al., The Journal of Physical Chemistry C, ACS Publications, 2014
- [43] “*Poromechanical effect in the lithium-sulfur battery cathode*”, P.Barai et al., Extreme Mechanics Letters, Elsevier, 2016.
- [44] “*Revisit Carbon/Sulfur Composite for Li-S batteries*”, J.Zheng et al., Journal of The Electrochemical Society, ECS, 2013
- [45] “*Cathode porosity is a missing key parameter to optimize lithium-sulfur battery energy density*”, N.Kang et al., Nature Communications, 2019.
- [46] “*Fair performance comparison of different carbon blacks in lithium-sulfur batteries with practical mass loadings - Simple design competes with complex cathode architecture*”, A. Jozwiuk et al., Journal of Power Sources, Elsevier, 2015
- [47] “*Which Process Limits the Operation of a Li-S System?*”, S. D. Talian et al., Chemistry of Materials, Elsevier, 2019
- [48] “*Correlations between precipitation reactions and electrochemical performance of lithium-sulfur batteries probed by operando scattering techniques*”, Y.C. Chien et al., Chem, Cell Press, 2022